# Transport Properties of Driven Topological Systems


**Thomas Adam Simons,**
Department of Physics
Lancaster University

This thesis is submitted for the degree of
*Doctor of Philosophy*

September, 2022

*To my grandfather Richard,*

*who crossed the bar and is greatly missed.*

# Declaration

I declare that the work presented in this thesis is, to the best of my knowledge and belief, original and my own work. The material has not been submitted, either in whole or in part, for a degree at this, or any other university. This thesis does not exceed the maximum permitted word length of 80,000 words including appendices and footnotes, but excluding the bibliography.

Thomas Adam Simons

# Abstract

The work in this thesis is centred around exploring the transport properties induced by periodically driving topologically non-trivial systems. In particular, it focuses upon the signatures associated with Majorana modes in 1D topological superconductors and their adiabatic manipulations, in anticipation of the next generation of experiments pursuing the realization and control of such excitations, which have been stipulated as the potential building blocks of robust quantum computation.

We examine two distinct ways by which external driving can influence a system's topology. Firstly, we focus upon systems for which the modulation results in the emergence of additional topological phases, not present in their static counterparts, the classification of which is not well defined by the usual topological invariants associated with the energy spectrum of the bulk system. For such systems, transport properties are vital in identifying non-trivial topological regimes and, with this motivation, we examine the relationship between driven scattering matrix topological invariants and conductance signatures.

Secondly, we determine the transport statistics associated with the adiabatic manipulation of topological excitations appearing in static systems, with a specific focus upon a Majorana braiding protocol. In this way, we demonstrate that the topological protection of the operation is reflected in geometric contributions to the heat transport induced by the driving. In addition to providing potential experiential signatures of such manipulations, this analysis also sheds light on the influence of periodic driving upon exchange fluctuation theorems, that govern the thermodynamics of non-equilibrium quantum systems, and also the performance of such protected operations as nanoscale thermal machines.

# Publications

- **T. Simons**, D. Meidan, and A. Romito

  *Pumped heat and charge statistics from Majorana braiding*

  Phys. Rev. B **102**, 245420 (2020)

- **T. Simons**, A. Romito, and D. Meidan

  *Relation between scattering matrix topological invariants and conductance in Floquet Majorana systems*

  Phys. Rev. B **104**, 155422 (2021)

# Acknowledgements

The completion of this thesis would not have been possible without the endless guidance, support and patience of my supervisor Alessandro Romito. I'm indebted to the countless hours of stimulating discussion and mentorship that instilled me with the passion, determination and confidence to complete this work. Much of this was provided during the challenging times of the COVID-19 pandemic and I greatly appreciate the sacrifices made to maintain an unwavering level of support, in spite of the sometimes testing circumstances.

I would also like to extend my thanks to my collaborator Dganit Meidan for providing the opportunity to work on several exciting topics together and always having time for insightful discussions and guidance.

Furthermore, I would like to acknowledge the Lancaster University Physics department for the provision of a studentship and to show my appreciation to all members of the Condensed Matter Theory group for always providing a welcoming atmosphere and contributing to the development of my knowledge through the provision of many meetings and seminars. Special thanks goes to my fellow PhD students Dominic Shea and Chun Leung whose arrival in the group allowed me to truly feel at home and provided me with many hours of laughter and entertainment.

Similarly, I must also acknowledge my friends further afield, Luke and Mark, for always helping to preserve my confidence during moments of doubt and whose own achievements are a constant source of inspiration. Most importantly, our online gaming sessions provided much needed relief during stressful times.

Finally, I must express my gratitude to my family. I'm deeply grateful to Green for her endless love and patience and for always sticking by my side through the ups and

downs of this journey. Thank you also to my extended family and friends in Taiwan. Our chats are always one of the highlights of my week. Lastly, a heartfelt thanks to my sister Katie and to my parents. I owe everything to their continued support and motivation and without them none of this would have been possible.

# Contents

# List of Figures

# List of Tables

# Chapter 1

# Introduction

A key aspect of condensed matter physics is the classification of systems into distinct phases based on their underlying properties and the external conditions to which they are subjected. Conventional phase transitions are well described by Landau's theory, which states that phase transitions occur upon the breaking of some internal symmetry of the system [1–3]. Despite its success in the classification of a myriad of crystalline structures and emergent properties such as magnetism and superconductivity, the discovery of the quantum Hall effect posed a stumbling block to this theory by exhibiting distinct phases characterized by the emergence of quantized conductance along the edges of a sample, the bulk of which remains in an insulating state [4–7]. Crucially, the emergence of this conductance occurs without the breaking of any local symmetry and hence such phases require an alternative notion of classification.

This discovery initiated the concept of the topological classification of condensed matter systems, a notion more commonly encountered in Mathematics, where it is used to differentiate continuous manifolds which cannot be smoothly deformed into one another. Within the realm of condensed matter physics, this idea can be used to group

wavefunctions that are adiabatically connected and distinct topological phases can be defined by the value of a topological invariant that is immune to such deformations [8–13]. Importantly, this manner of classification is based upon the global properties of the object in question, as opposed to the local structure, and hence the topological properties of each phase are robust against adiabatic perturbations to the system.

One particularly striking consequence of topologically non-trivial states of matter is the existence of gapless excitations at the boundaries with systems of a different topological class [11]. It is such protected excitations that result in the quantized conductance across quantum Hall systems [14] and such excitations take on increasingly remarkable properties when the concept of topological classification is extended to superconductors [15, 16]. Superconducting systems allow for emergence of quasi-particles consisting of linear combinations of particles and holes and, at zero energy, this results in the appearance of Majorana zero modes (MZMs); excitations for which the creation and annihilation operators are identical [17–22]. The possible existence of such excitations was first eluded to by Kitaev's toy model of a 1D spinless $p$-wave superconductor [18], followed by the suggestion of their presence within vortices in 2D $p_x + ip_y$ superconductors [23].

Much of the excitement surrounding MZMs, and thereby the motivation for them forming the focus of this thesis, stems from their potential applications in the field of topological quantum computation [21, 24–28]. It has been stipulated that two spatially separated MZMs, defining a non-local state, could in principle encode information as a qubit system. The topological protection of the constituent MZMs partnered with the fact that the information is encoded non-locally, would instill such a theoretical qubit with a high resistance to decoherence via local perturbations. Furthermore,

the MZMs exhibit non-Abelian statistics under exchange [23, 24, 29], allowing for the protected control of the qubit state and the execution of some computational gates. Such potential applications have motivated a multitude of attempts to realize such excitations experimentally [30–34], many of which are centered around detecting signatures via electronic tunnelling spectroscopy. It is known that the scattering of electrons via MZMs, when in contact with an external metal lead, should yield a quantised zero-bias peak in the conductance spectrum [35, 36]. However, such a feature is not a unique consequence of the existence of Majoranas [37, 38] and hence alternative detection methods are desirable. Furthermore, in anticipation of the next generation of experiments beyond detection, it is of interest to explore the transport signatures associated with dynamical manipulation of MZMs, such as braiding operations, for which several theoretical implementation proposals already exist [39, 40].

As a consequence of the correspondence between topological classification and the presence of gapless boundary modes, scattering matrices can provide an alternative tool in the identification of topological phases [41–43]. Indeed, scattering matrices provide alternative topological indexes for all symmetry classes present in the so called 10-fold way [44], providing a complete classification of the zoo of possible symmetry protected topologically non-trivial states of matter. This approach is particularly applicable to the identification of the additional topologically distinct phases that arise in systems subjected to a source of periodic driving. Such Floquet topological systems attract interest due to the ability to manipulate their properties and induce phase transitions by simple changing the driving frequency [45–51]. However, unlike their stationary counterparts, the original topological invariants associated with the eigenstates of the bulk system can fail to capture the behaviour at the boundary [47, 52, 53]. Despite

this, stroboscopic scattering matrices, defined by only turning on the coupling to external leads after regular intervals, remain sensitive to the existence of gapless modes and are hence an indispensable tool in the classification of such driven systems [53]. However, the exact relationship between this fictitious stroboscopic scattering setup and the electronic conductance that would be accessible in potential experiments, with constantly coupled leads, remains unclear and hence is one of the topics addressed in this work.

In addition to the emergence of additional topological features in periodically driven systems, it is also of interest to consider the transport properties associated with the time dependent manipulation of the topological excitations existing in static systems. When connected to external baths of particles, the slow driving of a quantum system is known to stimulate the transition of, or *pump*, both particles and energy between the baths, even in the absence of potential or temperature biases [54, 55]. These *geometric* contributions to the transport are intricately connected to the Berry phase accumulated during the periodic manipulation of a quantum state [56]. This contribution takes on a renewed significance in systems for which the dynamical operations in question are topologically protected, such as the exchange of Majorana zero modes [57] which is the chosen example addressed in this work.

Geometric contributions to heat transport are also known to have a profound impact upon the thermodynamic properties of driven mesoscopic systems. Specifically, they have been shown to result in corrections to steady state fluctuation theorems, that quantify the likelihood of anomalous heat transfer against a thermal gradient and are of fundamental importance to understanding the second law of thermodynamics on a mesoscopic scale [58–62]. The potential for topologically protected transport

contributions, and consequently the possibility of driving a highly controlled heat flux against a thermal gradient, means that it is also of interest to consider the performance of adiabatically driven quantum systems as thermal machines [63–66] and consequently this forms the final focus of this thesis. The ability to utilise the flow of heat to perform useful work or, conversely, use the external driving in order to refrigerate at the nanoscale is of fundamental importance to the development of a host of quantum technologies [67–71]. The highly robust nature of topologically protected operations adds an additional desirable facet to the operation of such a thermal machine.

## Structure of Thesis

The work in this thesis addresses themes concerned with the connection between transport properties and periodically driven topological systems, using scattering matrices as the central tool. It is divided into two main parts. Part I introduces the background theoretical framework required to explore the properties of the topological superconducting systems analysed in Part II, in which the culmination of my original studies of such systems are presented. Specifically, Chap. 2 will introduce the general notion of topology in condensed matter physics, before focusing upon the emergence of Majorana zero modes in topological superconducting systems. Chap. 3 then provides an outline of how we can study the transport properties of such systems by introducing Landauer-Büttiker theory and the scattering matrix formalism. This formalism is then extended for application to both superconducting and periodically driven Floquet systems. We will also explore how the underlying symmetries of the scattering matrix can be exploited for the classification of topological phases. The fluctuations theorems describing the work done by an isolated system as well as the heat exchange between

reservoirs are introduced in Chap. 4.

Chap. 5 is concerned with studying the transport properties of the additional topological phases that arise due to external driving and focuses on the example of a one-dimensional superconducting nanowire, periodically driven to host both Majorana zero and $\pi$ modes. We compare the electronic conductance accessible in transport experiments with constantly coupled leads, with the conductance defined using the stroboscopic scattering matrix, formulated by considering pulse-like coupling at periodic intervals. In this way, we shed light upon the connection between the scattering matrix topological invariants used to classify Floquet systems and the raw DC conductance.

Chap. 6 centres around the transport processes induced by performing a Majorana braiding operation, when coupled to external fermionic reservoirs. Using a scattering matrix approach, we analyse the full counting statistics of both the heat and charge transport driven by the process and hence identify geometric contributions that share the topological protection of the braiding operation. The calculation of the full probability distribution describing the flow of heat, allows for the analysis of the relevant fluctuation theorem for this driven system. Finally, in Chap. 7, the discussion of the Majorana braiding protocol is extended to assess its performance as a quantum thermal machine.

# Part I

# Theoretical Framework

# Chapter 2

# Topology in Condensed Matter Physics

## 2.1 Topological band theory

The topological classification of two geometrical objects concerns whether they can be smoothly transformed into one other, that is, without the alteration of some global property such as the number of holes [8, 9, 13]. Within the realm of mathematics this notion can be illustrated by considering the simple structures of a sphere and torus. The hole in a torus cannot be created by continuous deformations of the sphere and hence these two objects are topologically distinct [72]. However, the torus belongs to the same topological class as a coffee cup, since they share the same number of holes. The number of holes thereby defines what is known as a topological invariant; an integer value, determined by a global property of the system, that cannot be changed under smooth deformations [73].

The concept of topological classification can also be extended into a condensed

matter setting and, in particular, can be applied to crystalline systems that exhibit translational invariance. This translational symmetry allows the system to be described in terms of a Bloch Hamiltonian $H(\boldsymbol{k})$ acting within a single unit cell of the crystalline structure, where $\boldsymbol{k}$ is the periodic crystal momentum defined within the Brillouin zone. The eigenstates, or Bloch states $|u_m(\boldsymbol{k})\rangle$, of this Bloch Hamiltonian then define the possible electronic states of the system, with the corresponding eigenvalues $\epsilon_m(\boldsymbol{k})$ describing energy bands that together form the band structure [74], each labelled by a band index $m = 1, 2, 3, \ldots$. Therefore, within the context of condensed matter physics, two quantum systems which exhibit a finite energy gap between the highest occupied band and lowest empty excited state band are said to be topologically equivalent if their Bloch Hamiltonians can be adiabatically deformed into one another without closing this gap [8,9,13]. Each topologically distinct phase is characterised by some integer invariant quantity $n \in \mathbb{Z}$ that depends upon the topological structure of the Bloch wavefunctions in momentum space.

One important quantity, crucial in the determination of such topological invariants, is the Berry phase $\gamma_m$ [75]. This is the phase factor that, in addition to the dynamical phase $\gamma_m^{\text{dyn}} = -\int \epsilon_m(\boldsymbol{k}(t))dt$, is accumulated as an eigenstate is adiabatically taken around some closed path $\mathcal{C}$ in parameter space. The Berry phase is a purely geometric quantity and can be expressed as a closed contour integral of the so-called Berry connection $\mathcal{A}_m(\boldsymbol{k}) = i \langle u_m(\boldsymbol{k})| \boldsymbol{\nabla}_{\boldsymbol{k}} |u_m(\boldsymbol{k})\rangle$ [76]:

$$\gamma_m = \oint_C d\boldsymbol{k} \cdot \mathcal{A}_m(\boldsymbol{k}). \tag{2.1}$$

The Berry connection can also be used to construct a gauge invariant quantity known as the Berry curvature $\Omega_m = \nabla_{\boldsymbol{k}} \times \mathcal{A}_m$. The flux of this quantity passing through the

entire Brillouin zone gives us our topological classification of the eigenstate $|u_m(\boldsymbol{k})\rangle$, known as the Chern invariant

$$Ch_m = \frac{1}{2\pi}\int_{BZ} d\boldsymbol{k}\ \Omega_m(\boldsymbol{k}). \tag{2.2}$$

In the case that the eigenstate in question is topologically trivial, and hence the Berry connection $\mathcal{A}_m(\boldsymbol{k})$ exhibits no singularities over the entire Brillouin zone, the Chern number can be evaluated via Stokes' theorem, with the periodicity of the Brillouin zone resulting in a vanishing integral and $Ch_m = 0$. In the case that there exists a singularity in Berry connection at some point in a region $R$ of the Brillouin zone, then we can perform a gauge transformation $|u_m(\boldsymbol{k})\rangle \to e^{i\phi_m(\boldsymbol{k})}\,|u_m(\boldsymbol{k})\rangle$ such that this singularity is removed. This results in a subsequent transformation of the Berry connection:

$$\mathcal{A}'_m(\boldsymbol{k}) = \mathcal{A}_m(\boldsymbol{k}) - \boldsymbol{\partial}_{\boldsymbol{k}}\phi_m(\boldsymbol{k}), \tag{2.3}$$

and Stokes' theorem gives us a Chern number of

$$Ch_m = \frac{1}{2\pi}\int_{\partial R} d\boldsymbol{k}\cdot\boldsymbol{\partial}_{\boldsymbol{k}}\phi_m(\boldsymbol{k}), \tag{2.4}$$

where $\partial R$ is the boundary of $R$. Since our choice of gauge $e^{i\phi_m(\boldsymbol{k})}$ is a unique function on $\partial R$, the value of this integral must be $2\pi N$ with integer $N$ and consequently we have that $Ch_m \in \mathbb{Z}$ [8, 73, 76]. The fact that the Chern number is restricted to take integer values means that under continuous deformations of the Hamiltonian, which maintain the energy gap between bands and result in continuous changes to the Berry curvature, it cannot change. Only when the energy gap separating $\epsilon_m$ from a neighbouring band

closes, at which point the Berry connection is not well defined, can the Chern number be altered. We hence see that $Ch_m$ behaves like a topological invariant.

The connection between topological spaces and the band structure of some Bloch Hamiltonian $H(\boldsymbol{k})$ can be visualised in the case of a generic gapped two level system. The general form of the Hamiltonian describing such a system can be expanded in the basis of Pauli matrices as

$$H(\boldsymbol{d}) = d_x\sigma_x + d_y\sigma_y + d_z\sigma_z = \boldsymbol{d}\cdot\boldsymbol{\sigma}, \tag{2.5}$$

where $\boldsymbol{d} \in \mathbb{R}^3$ and $|\boldsymbol{d}| \neq 0$ in order to avoid the degeneracy in the energy spectrum occurring at the origin, so that the system remains gapped. For now, we do not specify the spatial dimension of the system in question and hence do not include the wave vector dependence of $\boldsymbol{d}$. Labelling the two eigenstates of this system as $|\pm\rangle$, one can show that, in the parameter space defined by the vector $\boldsymbol{d}$, the corresponding Berry curvatures can be calculated as [76, 77]

$$\Omega_\pm(\boldsymbol{d}) = \pm\frac{\boldsymbol{d}}{|\boldsymbol{d}|}\frac{1}{2\boldsymbol{d}^2}. \tag{2.6}$$

This corresponds to the field of a point-like monopole source of Berry curvature, emanating from the origin of our parameter space.

As an example of such a two band system, we can consider the case of an electron with two possible internal states, hopping on a translation invariant 2D lattice. The internal states may correspond to electron spin or some sublattice index in the case that the electron is spin polarized. The function $\boldsymbol{d}(\boldsymbol{k})$ now maps each 2D wave vector $\boldsymbol{k} = (k_x, k_y)$ to a 3D vector in the parameter space defined by $\boldsymbol{d}$. Due to the periodicity

of the crystal momentum, as we sweep $\boldsymbol{k}$ through the Brillouin zone the endpoints of the vector $\boldsymbol{d}(\boldsymbol{k})$ map out a deformed torus in $\mathbb{R}^3 \setminus 0$. The value of the Berry curvature flux passing through the torus, defined by the mapping $\boldsymbol{d}(\boldsymbol{k})$ over the Brillouin zone, is then 0 in the case that the monopole source at the origin lies outside of the torus and $2\pi N$, with $N \in \mathbb{Z}$, if the origin is contained within the torus. This results in quantized integer values of the Chern number. Furthermore, we can see that deforming a torus into one with a different Chern number necessarily requires that the surface intersects the origin, corresponding to the point at which the band gap closes. Hence, we can visualize the protection of the Chern number under deformations that preserve the energy band gap which separates distinct topological phases.

### 2.1.1 Quantum Hall effect

The first example of a topologically non-trivial insulating state was discovered in 1980, in the form of the integer quantum Hall effect (IQHE) [4]. Such an effect is exhibited in a two-dimensional electron gas subjected to a strong magnetic field, acting perpendicularly to the plane. The action of the magnetic field, $B$, is to force electrons in the bulk of the material to perform quantized circular orbits with a cyclotron frequency $\omega_c = eB/m_e$, where $e$ and $m_e$ denote the electron charge and mass respectively. The band structure of the bulk then takes the form of flat Landau levels with energies given by $\epsilon_m = \hbar\omega_c(m + 1/2)$. In the case that $N$ of these Landau levels are filled and the remaining levels are empty, the Fermi energy lies in a gap in the band structure and we have an insulating Hamiltonian for which we can calculate the Chern numbers associated with each band. In a finite quantum Hall system, states close enough to the edges have energy bands which are deformed by the effects of the confining potential and

hence cross the Fermi energy. Classically, we can imagine that electrons at a distance from the edge that is smaller than their cyclotron orbit radius are reflected by the surface and forced to skip along the boundary in a single direction. These conducting states, bound to the edges of the bulk insulating system and forced to propagate in a single direction, are known as chiral edge modes. As a consequence, one can show that the Hall conductance, dictating the current that flows perpendicularly to an applied voltage, takes quantized values [5]:

$$\sigma_{xy} = N\frac{e^2}{h}, \tag{2.7}$$

where $N$ is the number of occupied Landau levels. It can also be shown that $N$ corresponds exactly to the sum of the Chern numbers for each of the occupied bands of the system [6]. Consequently, each allowed quantized value of the Hall conductance corresponds to the system being in a distinct topological phase.

### 2.1.2 Bulk-boundary correspondence

The existence of conducting states at the edges of bulk insulating systems, such as those appearing in the 2D quantum Hall state, constitutes a universal property of non-trivial topological phases. This correspondence between the topological classification of the energy bands of a bulk insulating system and the existence of edge modes is known as bulk-boundary correspondence [11]. The emergence of such gapless edge states can be understood by considering the interface of crystal structures of differing topologies. Since we have seen that topological invariants can only change upon the closure of the bulk band gap, gapless energy modes must exist somewhere within the interface over which the topological invariant changes. Due to the insulating nature of the bulk on

either side of such an intersection, these conducting states are localized at the interface and decay exponentially into the bulk. A more detailed derivation of the existence of such modes is included in Sec. 2.2, where we study a specific example of a topologically non-trivial phase in more detail.

### 2.1.3 The role of symmetries

Although the concept of bulk-boundary correspondence is a feature universal to phases of matter exhibiting a non-trivial topology, the nature of the topological invariants used to classify these phases are dependent upon the system in question. In particular, it is the presence or absence of the three fundamental Hermitian symmetries in the system's Hamiltonian, along with the dimensionality of the system in question, that determine the possible topologies of the occupied bands [15,44]. These three symmetries consist of two anti-unitary operators, time-reversal ($\mathcal{T}$) and particle-hole exchange ($\mathcal{C}$), which can either square to 1 or -1, along with the unitary operator representing chiral symmetry ($\chi$) which always squares to 1. It can be shown that [8, 9], in the absence of these symmetry constraints, the only possible topologically non-trivial state, in up to three dimensions, is that of the quantum Hall state in 2 dimensions with an integer topological invariant given by the Chern number defined previously. In other words, in 1D and 3D systems for which all three fundamental symmetries can be broken, all gapped Hamiltonians can be deformed into one another without closing the bulk gap.

The importance of symmetry on topological classification can be illustrated by considering what happens to a 2D insulating system in the presence of time-reversal symmetry [78, 79]. The time-reversal symmetry operator commutes with the Bloch

Hamiltonian so that

$$\mathcal{T}H(\boldsymbol{k})\mathcal{T}^{-1} = H(-\boldsymbol{k}). \tag{2.8}$$

In the case of a system containing spin-$\frac{1}{2}$ electrons, the relevant time-reversal operator is given by $\mathcal{T} = i\sigma_y\mathcal{K}$, where $\sigma_y$ represents the second Pauli matrix acting on the spin degree of freedom, $\mathcal{K}$ is the complex conjugation operator and we see that $\mathcal{T}^2 = -1$. The symmetry of such a system means that for every eigenstate $|u_n(\boldsymbol{k})\rangle$ of the Bloch Hamiltonian, its orthogonal, time-reversed partner $\mathcal{T}|u_n(\boldsymbol{k})\rangle$ is also an eigenstate with the same energy. This implies that every energy eigenstate of such a system is two-fold degenerate, known as Kramers degeneracy. Each Kramers pair can be denoted as $\left|u_n^I(\boldsymbol{k})\right\rangle$, $\left|u_n^{II}(\boldsymbol{k})\right\rangle$ and can be used to define corresponding Chern numbers $Ch_I$ and $Ch_{II}$. One can easily show that under time-reversal the Berry curvature transforms as $\Omega_m(\boldsymbol{k}) \to -\Omega_m(-\boldsymbol{k})$ and hence time reversal symmetry ensures that $Ch_I + Ch_{II} = 0$, so that the total Chern number of the occupied bands always vanishes. Despite this, the Chern numbers associated with the Kramers pairs can be used to define a new $\mathbb{Z}_2$ topological invariant that changes sign upon the closing of the energy gap and hence can be used to indicate the topology of each phase. For a time-reversal invariant system this index can be defined as

$$\nu = (-1)^{Ch_I} = (-1)^{Ch_{II}}. \tag{2.9}$$

A topological invariant of this type is restricted to take values of $\pm 1$ and consequently, such a system can only exhibit two topologically distinct phases.

Such time-reversal symmetric systems, when in the topologically non-trivial phase, will exhibit two gapless modes at each edge of the system. These so called helical edge

| Symmetry | | | | Dimension | | | |
|---|---|---|---|---|---|---|---|
| Class | $\chi$ | $\mathcal{C}$ | $\mathcal{T}$ | 0 | 1 | 2 | 3 |
| A | 0 | 0 | 0 | $\mathbb{Z}$ | 0 | $\mathbb{Z}$ | 0 |
| AIII | 1 | 0 | 0 | 0 | $\mathbb{Z}$ | 0 | $\mathbb{Z}$ |
| AI | 0 | 0 | 1 | $\mathbb{Z}$ | 0 | 0 | 0 |
| BDI | 1 | 1 | 1 | $\mathbb{Z}_2$ | $\mathbb{Z}$ | 0 | 0 |
| D | 0 | 1 | 0 | $\mathbb{Z}_2$ | $\mathbb{Z}_2$ | $\mathbb{Z}$ | 0 |
| DIII | 1 | 1 | -1 | 0 | $\mathbb{Z}_2$ | $\mathbb{Z}_2$ | $\mathbb{Z}$ |
| AII | 0 | 0 | -1 | $2\mathbb{Z}$ | 0 | $\mathbb{Z}_2$ | $\mathbb{Z}_2$ |
| CII | 1 | -1 | -1 | 0 | $2\mathbb{Z}$ | 0 | $\mathbb{Z}_2$ |
| C | 0 | -1 | 0 | 0 | 0 | $2\mathbb{Z}$ | 0 |
| CI | 1 | -1 | 1 | 0 | 0 | 0 | $2\mathbb{Z}$ |

Table 2.1: Classification of topological phases depending upon the symmetry class and number of spatial dimensions. For each of the possible classes the absence of the chiral ($\chi$), particle-hole ($\mathcal{C}$) and time-reversal ($\mathcal{T}$) symmetries are denoted by 0, whereas their their presence is indicated by a '$\pm 1$' depending on whether the operator in question squares to $\pm 1$. For each combination of symmetries and dimensionality, the possibility of the existence of a topologically non-trivial phase is indicated by the corresponding type of topological invariant. A '0' denotes the case for which only the trivial phase is present.

modes are counter-propagating and have opposite spins, meaning that although the Hall conductivity of the sample vanishes, there is instead a net spin Hall conductivity, leading such systems to be known as quantum spin Hall insulators [79].

This example provides a clear demonstration of how adding certain symmetries to a system can alter the nature of the topological phases that it can exhibit. We will study the effects of the particle-hole symmetry present in superconducting systems in the following section. One can show that it is possible to invoke 10 possible combinations of the three fundamental symmetries mentioned previously and for each it is possible to determine the nature of the topological invariant present depending on the spatial dimension. The result is a periodic table of invariants known as the 'Ten-fold way' [15, 44, 80] which is displayed in Table 2.1.

## 2.2 Kitaev chain

The work in this thesis is focussed upon the nature of topological phases within superconducting systems and as such we here outline one of the simplest toy models that can be used to illustrate their emergence: the Kitaev chain [18, 81]. The model describes a system consisting of a 1D chain of $N$ fermionic sites, each of which can be occupied by an electron of only one fixed direction of spin. The system is governed by the following Hamiltonian:

$$H = \sum_j \Big( -\mu(a_j^\dagger a_j - \frac{1}{2}) - \frac{w}{2}(a_j^\dagger a_{j+1} + a_{j+1}^\dagger a_j) + \frac{\Delta}{2} a_j a_{j+1} + \frac{\Delta^*}{2} a_{j+1}^\dagger a_j^\dagger \Big), \qquad (2.10)$$

where $\mu$ gives the on-site potential strength, $w \geq 0$ the nearest neighbor hopping amplitude and $\Delta = |\Delta| e^{i\theta}$ the superconducting gap. The operators $a_j^\dagger$ and $a_j$ denote the fermionic creation and annihilation operators acting on the site $j = 1, \ldots, N$.

### 2.2.1 Energy spectrum of the bulk

Since topological phase transitions occur when the energy gap of the bulk system closes, it is useful to analyse the bulk energy spectrum in order to determine in which regimes of the Hamiltonian parameters we should expect non-trivial topological features to be present. To this end we eliminate the boundaries of the Kitaev chain and assume periodic boundary conditions. In this situation, the system has a translational symmetry $|j\rangle \rightarrow |j+1\rangle$ and the momentum $k$ is a conserved quantum number with allowed values $2\pi n/N$, where $n = 1, ...N$. The creation and annihilation operators in

momentum space are given by

$$a_k = \frac{1}{\sqrt{N}} \sum_{j=1}^{N} e^{-ikj} a_j. \tag{2.11}$$

In momentum space, the Kitaev Hamiltonian can then be expressed in Bogoliubov-de Gennes (BdG) form:

$$H = \frac{1}{2} \sum_k A_k^\dagger H_{\mathrm{BdG}}(k) A_k, \qquad H_{\mathrm{BdG}}(k) = \begin{pmatrix} \epsilon_k & \tilde{\Delta}_k^* \\ \tilde{\Delta}_k & -\epsilon_k, \end{pmatrix} \tag{2.12}$$

where $\epsilon_k = -w \cos k - \mu$, $\tilde{\Delta}_k = -i\Delta \sin k$ and we have introduced the two-component operator $A_k^\dagger = (a_k^\dagger, a_{-k})$. The BdG Hamiltonian $H_{\mathrm{BdG}}$, is symmetric under the exchange of the particle and hole degrees of freedom. This particle-hole symmetry is captured by the anticommutation of the BdG Hamiltonian with the antiunitary operator $\mathcal{C} = \sigma_x \mathcal{K}$, where $\mathcal{K}$ is the complex conjugation operator:

$$\mathcal{C} H_{BdG}(k) \mathcal{C}^{-1} = -H_{BdG}(-k). \tag{2.13}$$

This symmetry results in a symmetric energy spectrum around $E = 0$, with a dispersion relation given by [20]

$$E_\pm(k) = \pm \sqrt{(w \cos k + \mu)^2 + \Delta^2 \sin^2 k}, \tag{2.14}$$

and with corresponding eigenstates taking the form

$$\psi_+ = \begin{pmatrix} u_k \\ v_{-k}^* \end{pmatrix}, \quad \psi_- = \mathcal{C} \begin{pmatrix} u_{-k} \\ v_k^* \end{pmatrix} = \begin{pmatrix} v_k \\ u_{-k}^* \end{pmatrix}. \tag{2.15}$$

Hence, particle-hole symmetry in this system means that any excitation at energy $E$ is necessarily accompanied by a corresponding excitation at energy $-E$. Diagonalizing the Hamiltonian,

$$H = \frac{1}{2} \sum_k E_+(k) \alpha_k^\dagger \alpha_k + E_-(k) \tilde{\alpha}_k^\dagger \tilde{\alpha}_k = \sum_k E_+(k) \alpha_k^\dagger \alpha_k, \tag{2.16}$$

we see that these excitations take the form of *Bogoliubov quasiparticles*, $\alpha_k$, $\tilde{\alpha}_k$, which consist of a linear combination of particle and hole operators:

$$\alpha_k = u_k^* a_k + v_{-k} a_{-k}^\dagger \quad \text{and} \quad \tilde{\alpha}_k = v_k^* a_k + u_{-k} a_{-k}^\dagger. \tag{2.17}$$

From these expressions it is evident that the positive and negative energy excitations, $\alpha_k$ and $\tilde{\alpha}_k$ respectively, are related as $\alpha_k = \tilde{\alpha}_{-k}^\dagger$ and hence a special case arises when $E_\pm = 0$, $k = 0$ and the operators define a particle that is its own anti-particle, otherwise known as a Majorana zero mode.

Such special points occur when the bulk energy gap closes which, from Eq. 2.14, we see occurs when the on-site potential is set to $\mu = \pm w$. Since the regimes for which $\mu < -w$ and $\mu > w$ are related by the particle-hole symmetry operator $\mathcal{C}$, it seems that the system exhibits two distinct gapped phases for parameter values $|\mu| < |w|$ and $|\mu| > |w|$ respectively. However, in order to see that these two regimes do indeed have distinct topologies, we require information beyond the bulk spectrum. In order to see

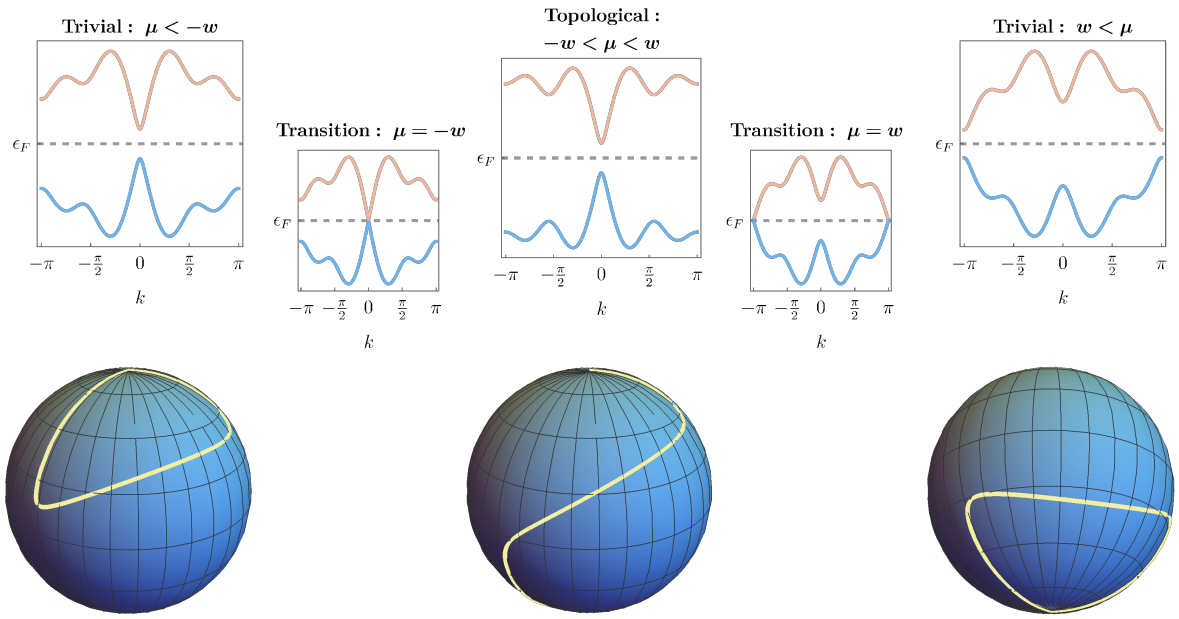


Figure 2.1: Band structure of the 1D Kitaev chain for several values of the parameters $(\mu, w, \Delta)$, including at the values for which a topological phase transition occurs: $\mu = \pm w$. For the points away from the phase transition, the path traced out by the vector $\boldsymbol{h}(k)$ (Eq. 2.18) on the unit sphere $\mathcal{S}^2$ as $k$ is swept through the Brillouin zone is also plotted and illustrates the two possible, topologically distinct, trajectories.

this, it is useful to write the BdG Hamiltonian $H_{\text{BdG}}$ in the form

$$H_{\text{BdG}}(k) = \boldsymbol{h}(k) \cdot \boldsymbol{\sigma}, \tag{2.18}$$

where $\boldsymbol{\sigma} = (\sigma_x, \sigma_y, \sigma_z)$ is the vector of Pauli matrices and $\boldsymbol{h}(k) = (h_x(k), h_y(k), h_z(k))$ with components given by

$$h_x(k) = \frac{\text{Re}\,\tilde{\Delta}_k}{E_+(k)}, \quad h_y(k) = \frac{\text{Im}\,\tilde{\Delta}_k}{E_+(k)}, \quad h_z(k) = \frac{\epsilon_k}{E_+(k)}. \tag{2.19}$$

Since $|\boldsymbol{h}(k)|^2 = 1$ when the spectrum is gapped, this vector maps a given wavenumber $k$ to a point on the surface of a 2D unit sphere $\mathcal{S}^2$. Sweeping the value of $k$ through

the Brillouin zone $-\pi < k \leq \pi$ then corresponds to tracing out a path on the surface of this sphere. The particle-hole symmetry of our Hamiltonian results in the following constraints on the components of the vector $\boldsymbol{h}(k)$:

$$h_{x,y}(k) = -h_{x,y}(-k), \quad h_z(k) = h_z(-k). \tag{2.20}$$

As a consequence, the mapped path of the Brillouin zone is constrained to pass through one of the poles of the sphere at both $k = 0$ and $k = \pi$. This results in paths with two distinct topologies: those passing through the same pole at both $k = 0$ and $k = \pi$, corresponding to paths that can be continuously deformed to a single point, and those passing through opposite poles that cannot. These two scenarios are illustrated in Fig 2.1 and can be distinguished by the $\mathbb{Z}_2$ topological index [20]

$$\nu = \mathrm{sgn}[\epsilon_0 \epsilon_\pi] = -\mathrm{sgn}[(w + \mu)(w - \mu)]. \tag{2.21}$$

Since $w \geq 0$ by definition, we find that $\nu = -1$, and hence the system exhibits a non-trivial topology, when $-w \leq \mu \leq w$.

The BdG Hamiltonian describing the bulk system can further be used to study the nature of the transition points between distinct topological phases and hence shed light upon the bulk-boundary correspondence introduced in Sec. 2.1.2 [82, 83]. Considering the case of $\mu = -w$, at which the bulk energy gap closes for $k = 0$, the Hamiltonian can be linearly expanded as

$$H_{\mathrm{BdG}}(k) \approx m\sigma_z + \Delta k \sigma_y, \tag{2.22}$$

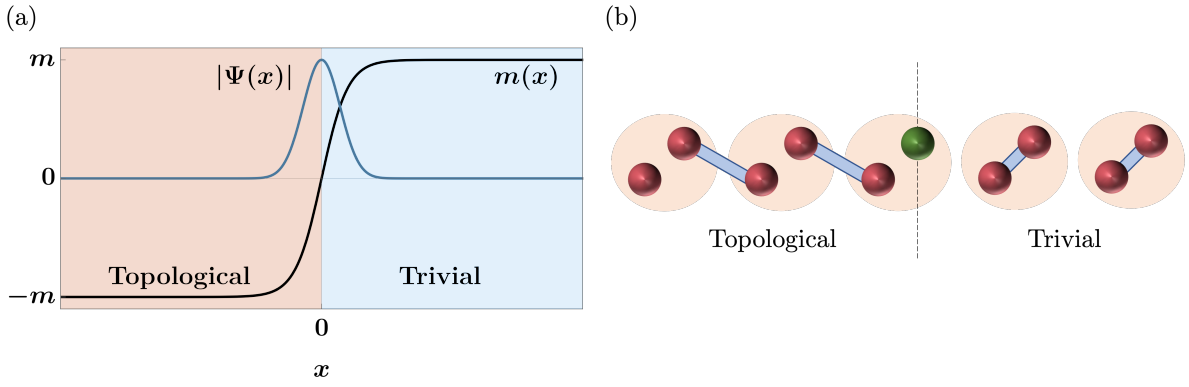


Figure 2.2: (a) Spatial dependence of the mass parameter $m(x)$ appearing in the linear expansion of the Kitaev chain Hamiltonian (Eq. 2.23), alongside the spatial dependence of the zero energy Majorana mode $\Psi(x)$. (b) Sketch of the interface between trivial and topological Kitaev chains. The orange circles represent the fermionic sites, each containing two red Majorana modes. The coupling between the Majoranas are illustrated by the blue lines, leaving the uncoupled green zero mode localized at the interface.

where $m = -w - \mu$. We see that, close to the gap closure, the system is described by a 'Dirac Hamiltonian' which is linear in $k$ and includes a 'mass' parameter $m$, the magnitude of which corresponds to the size of the band gap. We notice that $m$ changes sign across the topological phase transition, so that $m > 0$ corresponds to the trivial phase and $m < 0$ when the system is topological. Consequently, the interface between two different phases can be described by a mass parameter that varies continuously in space and changes sign at some point, as sketched in Fig. 2.2. In real-space, the Dirac Hamiltonian takes the form

$$H(x) = m(x)\sigma_z - 2\Delta\sigma_y i\partial_x, \tag{2.23}$$

where $m(x) \to \pm m$ for $x \to \pm\infty$ and $m = 0$ at the domain wall corresponding to $x = 0$. Since we know that gapless zero energy Majorana modes exist for $m = 0$, we can study

the spatial dependence of such states by solving $H(x)\Psi(x) = 0$. The solutions of this expression take the form

$$\Psi(x) = \exp\left( \pm \int_0^x \frac{m(x')}{2\Delta} dx' \right) \begin{pmatrix} 1 \\ \pm 1 \end{pmatrix}. \tag{2.24}$$

The fact that $m(x)$ changes sign at the interface results in only one of these two solutions being normalizable and hence physical. This solution takes the form of a wavefunction centered at the interface, which decays exponentially on both sides. Furthermore, in the case that $m(x)$ does not change sign, no zero-energy normalizable solution exists. This demonstrates the emergence of localized zero energy excitations at the boundary between two phases of differing topologies. This analysis can be extended to any topological system in order to demonstrate the universality of the principle of bulk-boundary correspondence.

### 2.2.2 Majorana zero modes

In order to highlight the physical consequences of the existence of a non-trivial topological phase in the Kitaev wire, it is instructive to assign to each fermionic site in the Kitaev chain a pair of Majorana operators defined as [18]

$$\gamma_{2j-1} = e^{i\frac{\theta}{2}} a_j + e^{-i\frac{\theta}{2}} a_j^\dagger, \qquad \gamma_{2j} = i\Big( e^{i\frac{\theta}{2}} a_j^\dagger - e^{-i\frac{\theta}{2}} a_j \Big), \tag{2.25}$$

satisfying the relations

$$\gamma_j^\dagger = \gamma_j \text{ and } \gamma_i\gamma_j + \gamma_j\gamma_i = 2\delta_{ij}. \tag{2.26}$$

Written in terms of these newly defined operators the Kitaev chain Hamiltonian takes the form

$$H = \frac{i}{2}\sum_{j=1}^{N-1}\Big( -\mu\gamma_{2j-1}\gamma_{2j} + \frac{1}{2}\big(w+|\Delta|\big)\gamma_{2j}\gamma_{2j+1} + \frac{1}{2}\big(-w+|\Delta|\big)\gamma_{2j-1}\gamma_{2j+1}\Big). \quad (2.27)$$

In this form, two limiting cases that highlight the distinct topological phases evident in this system become manifest. The first is the trivial phase for which $|\Delta| = w = 0$, $\mu < 0$ and the Hamiltonian becomes

$$H = -\mu\sum_{j=1}^{N-1}\Big(\gamma_{2j-1}\gamma_{2j}\Big) = -\mu\sum_{j=1}^{N}\Big(a_j^\dagger a_j - \frac{1}{2}\Big). \quad (2.28)$$

Here, we see that in this case only Majoranas belonging to the same fermionic site are coupled. This situation is illustrated in Fig. 2.3(a) and has a ground state corresponding to the situation where every fermionic site is empty. If instead we consider the case where $|\Delta| = w > 0$ and $\mu = 0$, then

$$H = iw\sum_{j=1}^{N}\gamma_{2j}\gamma_{2j+1} = 2w\sum_{j=1}^{N-1}\Big(\tilde{a}_j^\dagger\tilde{a}_j - \frac{1}{2}\Big). \quad (2.29)$$

In this case, only Majoranas from neighbouring sites are coupled and the Hamiltonian is diagonalized by alternative creation and annihilation operators defined as $\tilde{a}_j = \frac{1}{2}(\gamma_{2j} + i\gamma_{2j+1})$ and $\tilde{a}_j^\dagger = \frac{1}{2}(\gamma_{2j} - i\gamma_{2j+1})$. This is the situation shown in Fig. 2.3(b). Consequently, the Majorana operators localized at each end of the wire, $\gamma_1$ and $\gamma_{2N}$ remain uncoupled to the bulk of the chain and do not appear in the Hamiltonian. The system is now in the topological phase, characterised by the existence of these zero energy excitations at the system boundaries. These two unpaired Majorana operators

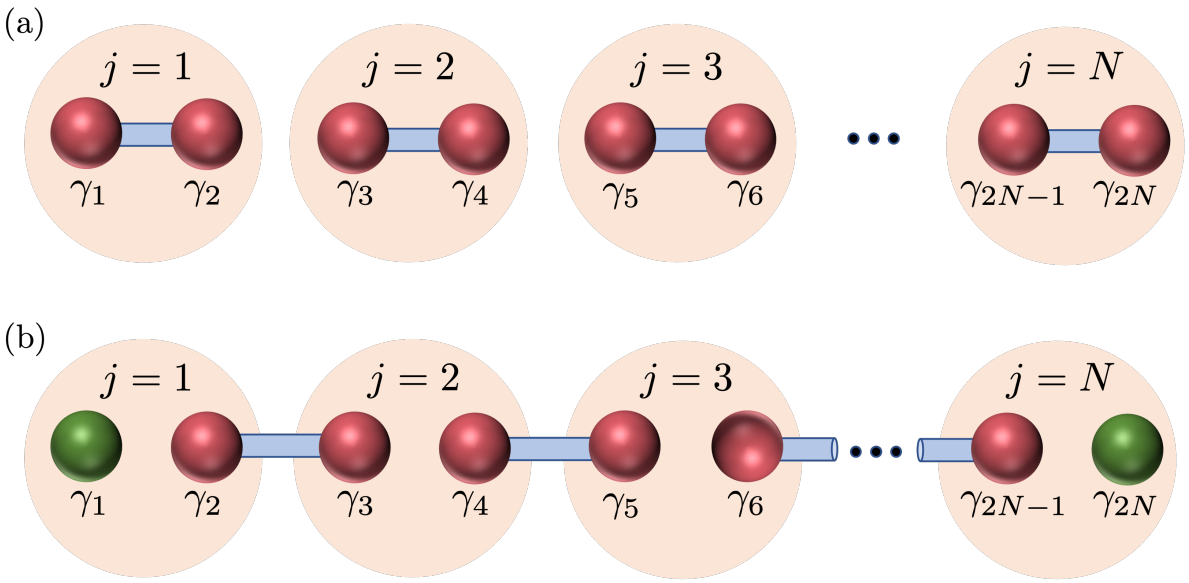


Figure 2.3: Schematic illustration of the two limiting cases of the Kitaev Hamiltonian for (a) $|\Delta| = w = 0$, $\mu < 0$ and (b) $|\Delta| = w > 0$, $\mu = 0$. In the former limit, Majoranas from the same fermionic site are coupled and the system exhibits a unique trivial ground state. In the latter, coupling between neighbouring sites leaves an unpaired Majorana at each end of the chain, resulting in a topologically non-trivial ground state with two-fold degeneracy.

define a non-local fermionic state, the occupation of which costs zero energy:

$$f = \frac{1}{2}(\gamma_{2N} - i\gamma_1). \tag{2.30}$$

The ground state of the system is hence two-fold degenerate and spanned by the states $|\psi_0\rangle$ and $|\psi_1\rangle = f^\dagger |\psi_0\rangle$ with opposite fermionic parity. The non-local nature of this fermionic state, along with the non-Abelian statistical properties of the Majoranas, make such systems appealing candidates for use as a topological qubit. These properties will be discussed in more detail in the next section, but before this we would like to study the behaviour of the Kitaev chain away from the two fully dimerized limits outlined above.

For arbitrary values of the Hamiltonian parameters $\mu$, $w$ and $\Delta$, the Kitaev Hamiltonian can be expressed in terms of the Majorana operators in a generic quadratic form [18]:

$$H = \frac{i}{4}\sum_{l,m} A_{lm}\gamma_l\gamma_m \text{ with } A^*_{lm} = A_{lm}. \tag{2.31}$$

Such a Hamiltonian can be diagonalised by fermionic operators $\tilde{a}^\dagger$ that are constructed as linear combinations of the operators associated with each site in the chain $a_j^\dagger$. From these one can construct associated Majorana operators $\tilde{\gamma}_j^{'}$, $\tilde{\gamma}_j^{''}$, defined via the relations $\tilde{a}_j = \frac{1}{2}(\tilde{\gamma}_j^{'} + i\tilde{\gamma}_j^{''})$ and $\tilde{a}_j^\dagger = \frac{1}{2}(\tilde{\gamma}_j^{'} - i\tilde{\gamma}_j^{''})$. In terms of these operators, the Hamiltonian takes the form

$$H = \frac{i}{2}\sum_{j=1}^{N} \epsilon_j \tilde{\gamma}_j^{'}\tilde{\gamma}_j^{''} = \sum_{j=1}^{N} \epsilon_j \Big(\tilde{a}_j^\dagger \tilde{a}_j - \frac{1}{2}\Big). \tag{2.32}$$

For values of the Hamiltonian parameters for which the bulk energy spectrum is gapped, any zero energy mode of the finite system must be localized at the ends of the chain. The particle-hole symmetry of the system also ensures that we chose zero energy states to have a support on only even or odd Majorana states $\gamma_j$. As such, any potential edge modes can be expressed in the general form

$$\begin{gathered}\gamma' = \sum_j (\alpha'_+ x_+^j + \alpha'_- x_-^j)\gamma_{2j-1}, \quad \gamma'' = \sum_j (\alpha''_+ x_+^{-j} + \alpha''_- x_-^{-j})\gamma_{2j}, \\ \text{with } x_\pm = \frac{-\mu \pm \sqrt{\mu^2 - w^2 + |\Delta|^2}}{w + |\Delta|}.\end{gathered} \tag{2.33}$$

These states are further subjected to boundary conditions enforced by the fact that it is necessary for them to vanish beyond the boundaries of the Kitaev chain: $\alpha'_+ + \alpha'_- = \alpha''_+ x_+^{-(N+1)} + \alpha''_- x_-^{-(N+1)} = 0$. Considering the two topologically distinct phases separated by the closing of the bulk energy gap:

- In the trivial phase, for $|w| < |\mu|$, we see that either $|x_+| > 1$ and $|x_-| < 1$ or $|x_+| < 1$ and $|x_-| > 1$. Consequently, in order to be localized at one end of the chain, one of the coefficients $\alpha'_+$ or $\alpha'_-$ must be equal to zero and hence cannot satisfy the boundary conditions. As a result, zero energy edge states do not exist in this phase.

- In the topological phase, for $w > |\mu|$, we have that $|x_+|$, $|x_-| < 1$ so that $\gamma'$ is localized close to $j = 1$ and $\gamma''$ close to $j = N$. In this case the boundary conditions can be satisfied and hence Majorana zero modes exist in the whole of this regime.

The persistence of the Majorana zero modes throughout the entire topological phase can also be understood by considering the symmetry protection of these states. Due to the particle-hole symmetry of the system and the resulting symmetric energy spectrum around $E = 0$, any perturbation to the Hamiltonian that would move a state away from zero energy individually is forbidden. Since the bulk spectrum is gapped throughout the phase, the only possibility of removing zero energy states is to couple the two unpaired Majorana states together. However, due to their localization at opposite ends of the system, the strength of this interaction decays exponentially with the length of the chain like $e^{-N/\xi}$, where $\xi$ is the Majorana coherence length, and hence can be assumed negligible in the limit $N \gg \xi$.

## 2.3 Majoranas in 2D superconducting systems

It can be shown that unpaired Majorana zero modes also arise in spinless 2D $p_x + ip_y$ superconducting system described by a Hamiltonian of the form [17, 20]

$$H = \int d^2\boldsymbol{r} \left\{ \psi^\dagger \left( -\frac{\nabla^2}{2m} - \mu \right) \psi + \frac{|\Delta|}{2} \left[ e^{i\phi} \psi (\partial_x + i\partial_y) \psi + H.c \right] \right\}, \tag{2.34}$$

where $\psi^\dagger$ is the creation operator for a spinless fermion with effective mass $m$, $|\Delta|$ determines the $p$-wave pairing amplitude and $\phi$ is the corresponding superconducting phase. As in the case of the 1D analogue, when in the topological phase this system is found to exhibit Majorana zero modes. In the 2D case, these Majorana states are bound to the edges of topologically trivial regions within the superconductor that are penetrated by an external magnetic flux and correspond to vortices in the superconducting pairing parameter $\Delta = |\Delta| e^{i\phi}$ [20, 84]. Several proposals of systems that have the potential to exhibit such an exotic superconducting state have been put forward. These include intrinsic realizations, such as the fractional quantum Hall state at filling factor $\nu = 5/2$ [17, 24] and the superconductors $Sr_2RuO_4$ [85, 86] and $Cu_xBi_2Se_3$ [87, 88], in addition to hybrid metal or semiconductor systems which are engineered to display the desired characteristics [89, 90], the basic principles of which will be outlined in Sec. 2.6. Although such 2D systems are not the focus of this thesis, they are useful for explaining the behaviour of Majorana zero modes under exchange and braiding, processes which require more than one spatial dimension to occur.

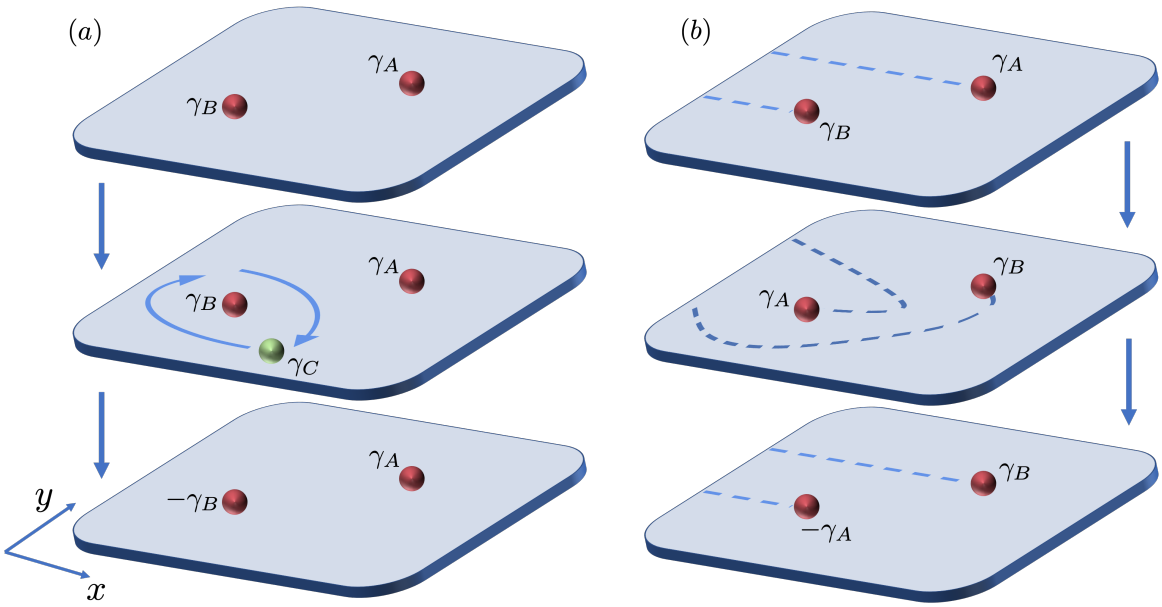


Figure 2.4: Schematic illustrations of vortex-bound Majorana braiding processes in a 2D topological superconductor. (a) demonstrates the phase factor acquired when one vortex is taken in a circular path around another, whereas in (b) we see the effect of directly exchanging the positions of two vortices, with the dotted lines representing the branch cuts in real space needed to unambiguously define the phase of the superconducting order parameter.

## 2.4 Exchange statistics of Majorana zero modes

### 2.4.1 Braiding MZMs in 2D

One of the most interesting properties of Majorana zero modes is the fact that they exhibit non-Abelian statistics under the exchange of their positions [23,24,29]. In order to demonstrate this, consider the setup illustrated in Fig. 2.4(a), consisting of a pair of vortices in a 2D superconducting system. Each vortex hosts a MZM denoted $\gamma_A$ and $\gamma_B$ which define fermionic creation and annihilation operators as

$$c_{AB}^{\dagger} = \frac{\gamma_A + i\gamma_B}{2}, \quad c_{AB} = \frac{\gamma_A - i\gamma_B}{2}. \tag{2.35}$$

We know that when particles obeying fermionic or bosonic statistics are exchanged twice, the wavefunction of the resultant state is the same as that with which we started. However, the non-locality of the creation and annihilation operators defined via the separated vortices in a 2D $p$-wave superconducting system, together with the fact that the system is confined to just two dimensions, means that this is not the case for the exchange of Majorana zero modes. To see this we consider the following sequence of processes [22]. We start initially with our vortices A and B as illustrated in Fig 2.4(a). We then consider the arrival of a third vortex C which proceeds to move in a path around vortex B before again moving far away, leaving us with our initial two vortices. Such a process is equivalent to the double exchange of vortices B and C and hence, under the assumptions of regular fermionic and bosonic statistics, we would expect the initial and final states of the sytem to match. To see that this is not the case, we first note that, due the Aharonov-Bohm effect, an electron or hole moving in one complete circuit around a vortex in a superconductor containing a flux quantum $\Phi_0 = hc/2e$, acquires a phase factor given by

$$e^{\pm\frac{ie\Phi_0}{\hbar c}} = -1. \tag{2.36}$$

Given that Majorana operators consist of a superposition of electron and hole states, a vortex bound Majorana moving around another such state transforms as $\gamma_0 \rightarrow -\gamma_0$. Consequently, the process illustrated in Fig 2.4(a) results in the following transformation of the fermionic operators defined by the vortices $A$ and $B$:

$$\begin{aligned} c_{AB}^\dagger = \frac{\gamma_A + i\gamma_B}{2} &\rightarrow \frac{\gamma_A - i\gamma_B}{2} = c_{AB}, \\ c_{AB} = \frac{\gamma_A - i\gamma_B}{2} &\rightarrow \frac{\gamma_A + i\gamma_B}{2} = c_{AB}^\dagger. \end{aligned} \tag{2.37}$$

We now consider the case that our system is initially in the state $|i\rangle$, corresponding to the fermionic state defined by the Majorana operators $\gamma_A$ and $\gamma_B$ being empty, so that

$$|i\rangle = |0\rangle\,, \quad c_{AB}\,|0\rangle = 0. \tag{2.38}$$

Considering the transformation of the fermionic operators, the final state of the system must satisfy

$$c_{AB}^{\dagger}\,|f\rangle = 0 \quad \Longrightarrow \; |f\rangle = |1\rangle \equiv c_{AB}^{\dagger}\,|0\rangle\,. \tag{2.39}$$

Hence we see that the final state of the system is orthogonal to the initial state and the Majorana zero modes behave as non-Abelian anyons. One should note here that this operation does not alter the parity of the total system since occupation of the fermionic state defined by $\gamma_C$ and its necessary partner will simultaneously change as a consequence of the exchange.

In order to determine the exact form of the unitary operator representing the single exchange of two MZM hosting vortices, we consider the situation illustrated in Fig. 2.4(b) [23]. In order to unambiguously define the phase of the superconducting order parameter $\phi$, we introduce branch cuts connecting each of the vortices with the left boundary of our system. We then take the superconducting phase to be single valued away from these cuts and jumping by $2\pi$ as you move across the cuts. From Eq. 2.34 we see that a shift in the superconducting phase by $\delta\phi$ is equivalent to a wavefunction transformation of the form $\psi \to e^{i\delta\phi/2}\psi$. As a consequence, a phase shift of $2\pi$ due to crossing a branch cut results in a sign change for any unpaired fermionic operators in the system. Since they are linear superpositions of these fermionic operators, the same applies to operators corresponding to MZMs. Considering the evolution of the branch

cuts as we perform a single exchange of two vortices as illustrated in Fig. 2.4(b) it becomes clear that this process will result in just one of the MZMs crossing a branch cut and hence being subjected to change of sign. Which of the two vortices experiences the sign change will depend upon whether the braiding is performed in a clockwise or anticlockwise direction in the 2D plane. The transformation corresponding to the braiding of MZMs $\gamma_A$ and $\gamma_B$ therefore takes the form:

$$T_{AB} : \begin{cases} \gamma_A \rightarrow \gamma_B \\ \\ \gamma_B \rightarrow -\gamma_A \end{cases} . \tag{2.40}$$

From this transformation we can construct the corresponding unitary operator associated with the braiding $U_{AB}$, such that $U_{AB}\gamma_i U_{AB}^{\dagger} = T_{AB}(\gamma_i)$. This operator takes the form

$$U_{AB} = \frac{1}{\sqrt{2}}(1 + \gamma_B\gamma_A) = \exp\left(\frac{\pi}{4}\gamma_B\gamma_A\right). \tag{2.41}$$

In the case of a system consisting of four vortices the MZMs can be combined to define two fermionic states as $c_{AB}^{\dagger} = (\gamma_A + i\gamma_B)/2$ and $c_{CD}^{\dagger} = (\gamma_C + i\gamma_D)/2$. The three operators corresponding to the braidings of neighbouring vortices can then be expressed

as matrices in the basis ($|00\rangle, c_{AB}^{\dagger}|00\rangle = |10\rangle, c_{CD}^{\dagger}|00\rangle = |01\rangle, c_{AB}^{\dagger}c_{CD}^{\dagger}|00\rangle = |11\rangle$):

$$\begin{aligned} U_{AB} &= \exp\Big(\frac{\pi}{4}\gamma_B\gamma_A\Big) = \exp\Big(-i\frac{\pi}{4}\mathcal{I}\otimes\sigma_z\Big), \\ U_{CD} &= \exp\Big(\frac{\pi}{4}\gamma_D\gamma_C\Big) = \exp\Big(-i\frac{\pi}{4}\sigma_z\otimes\mathcal{I}\Big), \\ U_{BC} &= \exp\Big(\frac{\pi}{4}\gamma_C\gamma_B\Big) = \frac{1}{\sqrt{2}}\begin{pmatrix} 1 & 0 & 0 & -i \\ 0 & 1 & -i & 0 \\ 0 & -i & 1 & 0 \\ -i & 0 & 0 & 1 \end{pmatrix}. \end{aligned} \tag{2.42}$$

In matrix form the non-trivial nature of the braiding operators becomes evident and in particular we see that the unitary operators $U_{AB}$ and $U_{BC}$ do not commute, so that $U_{AB}U_{BC} \neq U_{BC}U_{AB}$. This further illustrates the fact that such single exchange processes are indeed non-Abelian.

### 2.4.2 Braiding MZMs in 1D

Although the braiding of two MZMs requires a minimum of two spatial dimensions in order to perform without collisions, the process can also be achieved using a network of one-dimensional superconducting nanowires [91]. The simplest such network required to perform a braiding operation takes the form of a T-junction, as illustrated in Fig. 2.5(c). It is the exchange of MZMs hosted in such 1D structures that will form the focus of the majority of the work in this thesis. The T-junction consists of the three distinct wires meeting at a single junction. Each wire is described by a Kitaev Hamiltonian (Eq. 2.10) and can either reside in the topological or trivial phase depending on the on-site potential strength $\mu$. Since MZMs remain localized at the boundaries between phases of differing topologies, tuning $\mu$ locally along the wire provides a mechanism for

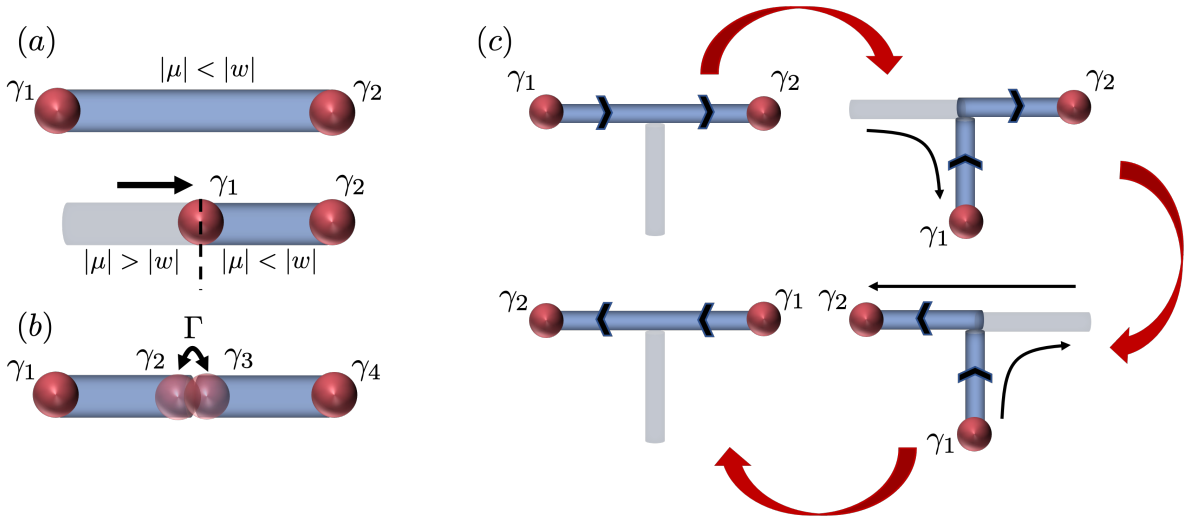


Figure 2.5: (a) Illustration of how tuning the on-site potential strength $\mu$ locally along the wire can be used to control the size of the topological region and hence the location of the Majoranas. (b) The coupling between the Majoranas at the junction between two superconducting nanowires in the topological regime results in the formation of a finite energy fermionic state at the interface. (c) Demonstration of how a T-junction configuration of 1D nanowires can be used to perform an exchange of the Majoranas $\gamma_1$ and $\gamma_2$. The black arrows on each topologically non-trivial wire are used to define the phase of the superconducting order parameter $\Delta$.

transporting Majoranas. This process is sketched in Fig. 2.5(a). Of course, moving an unpaired MZM towards the other end of the wire in this way will eventually result in a finite coupling between the MZMs at opposite end of the wire, thereby combining them into an ordinary finite-energy fermion. However, this scenario can be avoided in the case where we have two topological superconducting nanowires meeting at a junction, as shown in Fig. 2.5(b). This situation results in a finite coupling between the MZMs meeting at the junction. If the phase of the superconducting parameter is given by $\phi_{L/R}$ for the left/right chains, then this coupling can be shown to take the form [92, 93]

$$H_{\text{coup}} \sim -\frac{i}{2}\cos\left(\frac{\phi_L - \phi_R}{2}\right)\gamma^L_{B,N}\gamma^R_{A,1}. \tag{2.43}$$

Consequently, in general these MZMs combine to form a finite energy fermionic state that will not interact with the MZM we would like to move towards the junction. We note however that an exception occurs in the case that $\phi_L - \phi_R = \pi$, in which case the MZMs at the junction are decoupled.

Consider now the T-junction of three Kitaev chains as illustrated in Fig. 2.5(c). Initially both of the horizontal chains are assumed to be in the topological state and the vertical chain is trivial. Due to the universality of the braiding statistics, we are free to restrict our Kitaev Hamiltonian for each wire to be real as we perform the braiding. This restricts the superconducting phases to either 0 or $\pi$. Since the superconducting pairing term in the Hamiltonian gives us that $|\Delta|e^{i\phi}a_j a_{j+1} = |\Delta|e^{i\phi+\pi}a_{j+1}a_j$ we see that in order to rigorously define the problem, the superconducting phase must be defined relative to the direction in the wire for which the index $j$ increases. For the setup illustrated in Fig. 2.5(c), we define $j$ to increase as we move rightward/upward and so visualise the case that $\phi = 0$ with rightward/upward arrows and conversely $\phi = \pi$ is represented by leftward/downward arrows. The requirement that the coupling between MZMs at the junction should remain non-zero then manifests itself as requiring that one arrow should always point into the junction and one away from the junction throughout the braiding process. As demonstrated in Fig. 2.5(c), exchanging the MZMs $\gamma_1$ and $\gamma_2$ under this requirement results in a configuration for which the two arrows point in the opposite direction to the original configuration. In order to complete the process, a gauge transformation must then be performed to restore the Hamiltonian to its original form. This is achieved by multiplying all creation operators by $e^{i\pi/2} = i$, including the operator defined by the unpaired MZMs: $f^\dagger = (\gamma_1 - i\gamma_2)/2 \to (\gamma_2 + i\gamma_1)$. This corresponds to the transformation $\gamma_1 \to \gamma_2$ and $\gamma_2 \to -\gamma_1$, similar to that in the case

of braiding vortices in 2D (Eq. 2.40). Hence, exchanging Majoranas hosted by 1D superconducting nanowires results in the same non-Abelian operations achievable in 2D systems.

## 2.5 MZMs and quantum computation

Much of the excitement surrounding Majorana zero modes and their non-Abelian statistics results from their potential use for performing topologically protected quantum computation. A topological qubit can be implemented via a system consisting of two pairs of MZMs which correspond to fermionic operators $c_{AB}^{\dagger} = (\gamma_A + i\gamma_B)/2$ and $c_{CD}^{\dagger} = (\gamma_C + i\gamma_D)/2$. The four-fold degenerate ground-space is then spanned by the eigenstates $|00\rangle$, $|01\rangle$, $|10\rangle$ and $|11\rangle$ defined above Eq. 2.42. The parity conservation arising from the particle-hole symmetry of the superconducting system means that only coherent superpositions of states sharing the same parity are allowed and hence we can, without loss of generality, take the two states of our qubit system to be encoded as $|01\rangle$ and $|10\rangle$.

Crucially, since the MZMs are protected by the particle-hole symmetry of the system and are spatially separated, the states of such qubits would be protected against local perturbations at temperatures well below the superconducting gap $\Delta$. Furthermore, the requirement of fermionic parity conservation and the presence of the energy gap constrain the unitary evolution associated with the braiding to operate within the ground state subspace with fixed parity. These properties of the system completely determine the form of the braiding evolution operators given in Eq. 2.42 and hence render them independent of fluctuations in the driving process. The requirement of parity conservation also prevents fluctuations in the qubit occupation, rendering

its state immune to decoherence and circumventing the need for the error correction schemes necessary for other proposed methods of quantum computation.

As an example of how braiding operations can be used to execute quantum computational gates, we can once again consider the process illustrated in Fig 2.4(a). One can show that [8], by braiding the third MZM $\gamma_C$ in a complete circle around one of the existing MZMs, one exchanges the states spanning the ground-space of the system, corresponding to a NOT operation on the qubit:

$$U_{BC}^2 \begin{pmatrix} |01\rangle \\ |10\rangle \end{pmatrix} = i \begin{pmatrix} |10\rangle \\ |01\rangle \end{pmatrix} = i\sigma_x \begin{pmatrix} |01\rangle \\ |10\rangle \end{pmatrix}. \tag{2.44}$$

Similarly, the protected exchange of pairs of MZMs can be used to execute the remaining Pauli gates, $\sigma_y$ and $\sigma_z$, in addition to the Hadamard gate $H = \frac{1}{\sqrt{2}}(\sigma_x + \sigma_z)$. The action of single-qubit quantum gates can be represented as rotations on the Bloch sphere, which is the unit sphere spanned by the eigenstates of the qubit. In order to implement arbitrary rotations of the single qubit state on the Bloch sphere one additionally requires use of the $T$-gate:

$$T = \begin{pmatrix} 1 & 0 \\ 0 & e^{i\frac{\pi}{4}} \end{pmatrix}. \tag{2.45}$$

Achieving universal quantum computation, with a fundamental advantage over its classical counterpart, requires access to the $T$-gate, $H$-gate and the two-qubit controlled NOT gate [94]. While the latter can be executed in a topologically protected way via a combination of fermion-parity measurements and braiding [95], the same cannot be said about the $T$-gate. While proposals of how to implement the $T$-gate upon Majorana qubit systems do exist, via coupling to non-topological qubits for example [96], all

require the breaking of the topological protection and hence represent a fundamental limitation of this approach.

Despite the robust properties of Majorana qubit states and their manipulation, this potential topological protection against computational errors is reliant upon the maintenance of fixed fermionic parity in the superconducting system. Consequently, this protection is lost if the system is subject to quasiparticle poisoning (QPP) where single superconducting quasiparticles are able to tunnel into the host system from the environment. QPP is ubiquitous in proposed realistic non-trivial superconducting systems and hence poses a significant hurdle to performing protected computation [97, 98]. Minimizing the risk of qubit decoherence relies on ensuring that braiding processes are performed on timescales shorter than the quasi-particle poisoning time $\tau_{\mathrm{QP}}$ and hence understanding and potentially maximising this timescale is a subject of significant interest [28, 99, 100]. On the other hand, the coherence of the qubit state can also be lost if manipulations are performed fast enough to induce excitations out of the degenerate ground-space. Avoiding such non-adiabatic processes requires that braiding is performed over a timescale exceeding $\tau_{\Delta} = \hbar/\Delta$, set by the superconducting gap [25, 26]. These considerations present significant technological challenges in the quest to harness the advantage of topologically protected quantum computation and hence it seems the realization of such systems will likely need to be supplemented by quantum error correction schemes [101–103].

## 2.6 Physical realization of Majorana zero modes

To conclude our discussion of Majorana zero modes, we here briefly discuss the methods by which systems resembling Kitaev's toy model for a 1D, spinless, $p$-wave

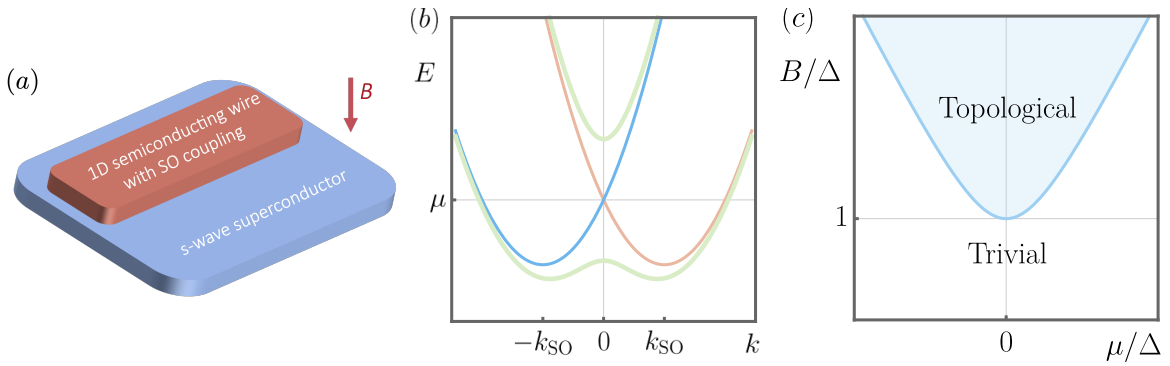


Figure 2.6: (a) Sketch of the fundamental components necessary to realize Majorana zero modes within a 1D spin-orbit coupled semiconducting nanowire, where $B$ is the strength of an external magnetic field. (b) Band structure corresponding to the Hamiltonian of a spin-orbit coupled wire, $H_{\text{wire}}$, in the absence (red and blue parabolas) and presence (green curves) of an external magnetic field. The parabolas are shifted on the momentum axis by $k_{\text{SO}} = m\alpha$, where $\alpha$ is the spin-orbit coupling strength. When the chemical potential $\mu$ lies in the gap induced by the magnetic field, the system is effectively spinless. The addition of a proximity-induced superconducting pairing term results in the phase diagram sketched in (c).

superconductor can be realized in practice. We will see that such a system can be constructed by endowing a semi-conducting nanowire with three key ingredients [92,93] (see Fig. 2.6(a)): spin-orbit coupling, proximity coupled $s$-wave superconductivity and an external magnetic field strong enough so that the system can be approximated as spinless.

Let us first focus upon the bulk Hamiltonian of a semi-conducting wire with spin-orbit coupling, subjected to an external magnetic field of strength $B$ [20]:

$$H_{\text{wire}} = \int \frac{dk}{2\pi} \left[ \psi^\dagger(k) \Big( \frac{k^2}{2m} - \mu + \alpha k \sigma_y + B\sigma_z \Big) \psi(k) \right]. \tag{2.46}$$

Here, $\mu$ is the chemical potential, $\alpha$ denotes the strength of the spin-orbit interaction and $\psi^\dagger(k) = (\psi^\dagger_\uparrow(k), \psi^\dagger_\downarrow(k))$, where $\psi^\dagger_\sigma(k)$ creates an electron with spin $\sigma$, effective mass

$m$ and momentum $k$. When the magnetic field is switched off, corresponding to $B = 0$, the electronic band structure is given by the red and blue parabolas sketched in Fig. 2.6(b). These parabolas correspond to electrons with spin aligned along $+y$ and $-y$ respectively and exhibit a crossing at the Kramers degenerate point $k = 0$ due the time-reversal symmetric nature of the system. This degeneracy results in an even number of pairs of Fermi points crossing the chemical potential $\mu$. Upon the addition of a superconducting pairing term, failure to lift this symmetry will result in two MZMs at each end of our nano-wire. These states will subsequently interact and conspire to remove the zero energy states from the system. Therefore, to have any hope of engineering a system capable of hosting unpaired MZMs, one must introduce a time-reversal symmetry breaking term in order to leave the system effectively spinless. This can be achieved via the addition of a non-zero magnetic field, $B \neq 0$, resulting in band energies

$$\epsilon_{\pm}(k) = \frac{k^2}{2m} - \mu \pm \sqrt{(\alpha k)^2 + B^2}, \tag{2.47}$$

illustrated by the green curves in Fig. 2.6(b). When the chemical potential $\mu$ lies within this induced energy gap, our system can be considered spinless as desired. Upon the addition of a superconducting pairing term to our system, this approximation can be maintained by focusing on this lower band only, an approximation that is valid in the limit $B \gg \Delta$.

We next briefly outline how to manipulate our wire in order to induce the $k$-dependent $p$-wave superconducting pairing present in the Kitaev chain Hamiltonian and required to induce non-trivial topological phases in the system. It can be shown [20, 90, 104], that by bringing a semi-conducting wire in close proximity with a bulk $s$-wave superconductor, Cooper pairing can be induced within the wire, leading to the

addition of an extra term to $H_{\text{wire}}$ of the form

$$H_\Delta = \int \frac{dk}{2\pi} \Delta\big(\psi_\uparrow(k)\psi_\downarrow(-k) + H.c.\big), \tag{2.48}$$

where $\Delta$ denotes the pairing amplitude of the proximity coupled $s$-wave superconductor. Rewriting the full Hamiltonian of the wire in terms of the eigenstates of the system with $\Delta = 0$, which we denote $\psi^\dagger_\pm(k)$, reveals the outcome of the interplay between the conventional superconducting pairing and spin-orbit interaction:

$$\begin{aligned}\tilde{H} = \int \frac{dk}{2\pi} \Bigg[ & \epsilon_+(k)\psi^\dagger_+(k)\psi_+(k) + \epsilon_-(k)\psi^\dagger_-(k)\psi_-(k) \\ & + \frac{\Delta_{\text{p}}(k)}{2}\Big(\psi_+(-k)\psi_+(k) + \psi_-(-k)\psi_-(k) + H.c.\Big) + \Delta_{\text{s}}(k)\Big(\psi_-(-k)\psi_+(k) + H.c.\Big)\Bigg],\end{aligned} \tag{2.49}$$

with pairing coefficients given by

$$\Delta_p(k) = \frac{\alpha k \Delta}{\sqrt{(\alpha k)^2 + B^2}}, \text{ and } \Delta_s(k) = \frac{B\Delta}{\sqrt{(\alpha k)^2 + B^2}}. \tag{2.50}$$

The first line in this expression simply describes the band energies of the system, whereas the second line encodes its proximity induced superconducting properties. We see that, as a result of the spin-orbit coupling interaction present in the wire, the system exhibits $p$-wave intraband pairing on top of the expected $s$-wave pairing term acting between the two bands. Taking the limit of strong magnetic field $B \gg \Delta$ is equivalent to sending $\psi_- \to 0$, leaving a spinless system with $p$-wave pairing only which connects smoothly to Kitaev's toy model in the topologically non-trivial phase. Since the band gap only closes when $B = \sqrt{\Delta^2 + \mu^2}$ we conclude that the system is topological for

field strengths satisfying

$$B > \sqrt{\Delta^2 + \mu^2}. \tag{2.51}$$

The phase diagram is sketched in Fig. 2.6(c). For values of $B$ below this critical value, the system can no longer be approximated as 'spinless' due to the increased influence of pairing between bands, resulting in a trivial state.

Following the initial theoretical proposals, the hunt for topologically non-trivial superconducting phases swiftly moved into the realm of experiments. Initial hybrid devices consisted of InAs or InSb semiconducting nanowires proximity coupled to a thin superconducting film of Al or Nb. [32, 105–108]. Such semiconductors have a spin-orbit interaction sufficient to open an appreciable $p$-wave superconducting gap $\Delta_p$, whilst being spin polarized by a magnetic field strength low enough to preserve the superconductivity of the proximity coupled $s$-wave superconductor.

Early experiments were concerned with identifying zero voltage bias conductance peaks by probing the superconducting nanowires using tunnelling spectroscopy techniques when coupled to a normal metal lead. Such a feature in the conductance spectrum would indicate the presence of localized states at the normal metal-superconductor interface that facilitate the resonant Andreev reflection of incoming electrons (see Sec. 3.3). Several studies reported evidence of such zero bias peaks that were found to persist over a range of magnetic field strengths within the expected topological regime [32, 105–107]. Such results were initially hailed as likely signatures of MZMs. However, later studies quickly began to demonstrate that the emergence of these features could also be accounted for by the existence of topologically trivial sub-gap excitations, known as Andreev bound states (ABSs) [38, 109–112]. Such states are formed when confined electrons are subjected to multiple coherent Andreev reflection

events and it has been demonstrated that such states are expected to exist within the hybrid superconducting devices under consideration here due to, for example, the presence of disorder [113] or the formation of quantum dots within the nanowire [37,114]. Furthermore, various mechanisms have been highlighted by which such states can become pinned to zero energy and hence mimic many of the features attributed to the presence of MZMs [38, 109–112]. As such, conclusive proof of the existence of MZMs is still lacking and the quest to differentiate between MZMs and ABSs continues. The focus of recent experiments is on probing the non-local nature of the exponentially separated MZMs, by examining correlations in the conductance measured at either end of the nanowire [115–117] or searching for signatures of the topological phase transition [118–120].

The engineered 1D topological superconducting nanowires outlined in this section also suffer from several technological challenges due to the fact that they require a high level of control of the system parameters in order enter the topological regime. For example, tuning the chemical potential using metallic gates is difficult due to screening by the proximity coupled superconductor. Furthermore, the strong magnetic field required can induce states within the superconducting gap, effectively softening the gap and reducing the topological protection of the system [121]. In an attempt to circumvent such issues, recent proposals have investigated a variety of 2D platforms for MZMs. For example, the use of a 2D electron gas coupled to a pair of superconductors forming a Josephson junction allows the onset of the non-trivial phase to be controlled via the tuning of the phase difference across the junction, even in the limit of a weak magnetic field [122]. Alternatively, it is hoped that 2D topological insulators hosting helical edge modes may play host to MZMs without the requirement of an external magnetic

field, potentially inducing a larger and more stable gap when proximity coupled to a superconductor [123]. For a detailed review of recent experimental advances in the field, see Refs. [108, 121, 124].

# Chapter 3

# Landauer-Büttiker Theory of Transport

## 3.1 Scattering theory

The Landauer-Büttiker scattering theory [125–128] provides a simple and effective tool for describing the electronic transport properties of mesoscopic conducting systems by mapping the process to a corresponding quantum-mechanical scattering problem [129, 130]. The theory assumes that our mesoscopic system of interest is coupled to $\mathcal{N}$ macroscopic particle reservoirs, as sketched in Fig. 3.1. These reservoirs act as a source of electrons which, upon entering the mesoscopic sample, are either reflected back into the reservoir from which they originated or transmitted into a different one. Such a scattering theory of transport is valid in a low enough temperature regime so that the phase coherence length, $L_\phi$, is much larger than the size of the sample [130]. Consequently, scattering events can be considered coherent and energy conserving. Under these conditions, electronic transport properties can be ascertained by observing

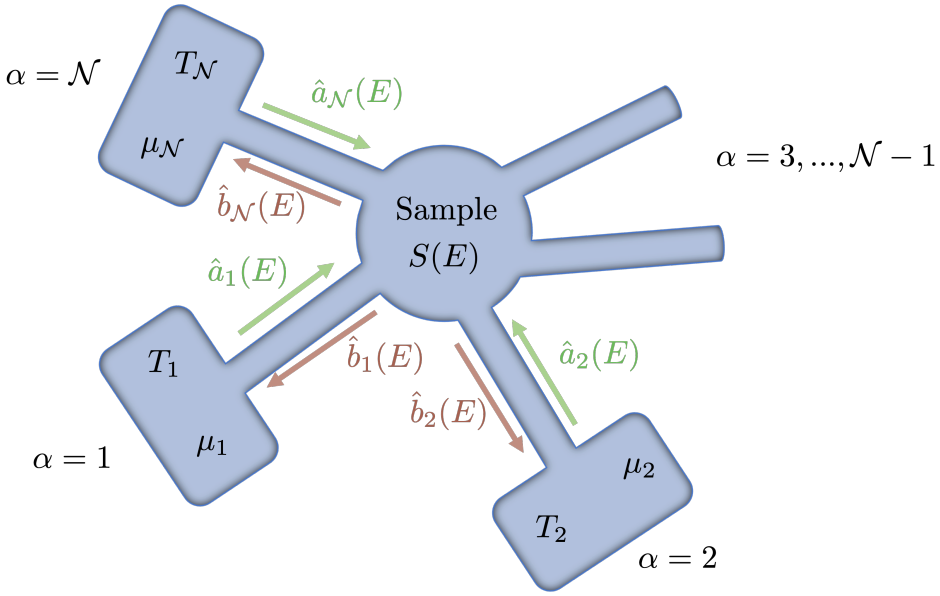


Figure 3.1: Mesoscopic sample coupled to multiple particle reservoirs (indexed $\alpha = 1, ..., \mathcal{N}$) via conducting metal leads. Each reservoir is characterised by a temperature and chemical potential, denoted $T_\alpha$ and $\mu_\alpha$ respectively. The green (red) arrows indicate the propagation direction of the incident (scattered) states in each lead, defined by the creation operators $\hat{a}^\dagger_\alpha(E)$ ($\hat{b}^\dagger_\alpha(E)$). The scattering matrix $S(E)$ encodes the relationship between the ingoing and outgoing operators at some energy $E$ and its exact form depends upon the physical properties of the mesoscopic sample in question.

the flow of electrons travelling towards or away from the scattering centre. The starting point of determining transport properties via scattering processes is the form of the eigenfunctions of ingoing and outgoing states in the leads connecting our sample to the particle reservoirs. The leads are defined as open in the longitudinal direction, $x$, and confined by some potential in the transverse direction, $y$. Such a situation results in separable wave functions, in each lead $j$, of the form [130]

$$\psi_\alpha(E, x, y) = \phi_{\alpha,n}(y) e^{ik_\alpha x}, \tag{3.1}$$

with wavenumber $k_j$ and transverse band number indexed by $n$. For simplicity, we will henceforward focus on the case in which only one transverse band exists for each lead. We denote wave functions propagating towards the scatterer, with positive wavenumber $k$, as $\psi_\alpha^{(\mathrm{in})}$ and those leaving the sample with negative wavenumber as $\psi_\alpha^{(\mathrm{out})}$.

In order to calculate the current flowing between the reservoirs, it is instructive to use the second quantization formalism and define creation and annihilation operators for particles in each of the leads. To this end, we use $\hat{a}_\alpha^\dagger(E)$ to represent an operator creating an ingoing electron in the lead $\alpha$, with wave function $\psi_\alpha^{(\mathrm{in})}(E)$ and $\hat{b}_\alpha^\dagger(E)$ for the creation operator of a scattered electron in the state $\psi_\alpha^{(\mathrm{out})}(E)$. These operators are subject to the usual fermionic anti-commutation relations:

$$\begin{aligned} \hat{a}_\alpha^\dagger(E)\hat{a}_\beta(E') + \hat{a}_\beta(E')\hat{a}_\alpha^\dagger(E) &= \delta_{\alpha\beta}\delta(E-E') \\ \hat{a}_\alpha^\dagger(E)\hat{a}_\beta^\dagger(E') + \hat{a}_\beta^\dagger(E')\hat{a}_\alpha^\dagger(E) &= 0 \\ \hat{a}_\alpha(E)\hat{a}_\beta(E') + \hat{a}_\beta(E')\hat{a}_\alpha^\dagger(E) &= 0. \end{aligned} \tag{3.2}$$

Similar relations hold for the outgoing operators $\hat{b}_\alpha^\dagger(E)/\hat{b}_\alpha(E)$.

The scattering matrix $S(E)$ is then defined as the linear operator mapping the vector of ingoing annihilation operators to the vector of outgoing annihilation operators at energy $E$:

$$\begin{pmatrix} \hat{b}_1(E) \\ \vdots \\ \hat{b}_{\mathcal{N}}(E) \end{pmatrix} = S(E) \begin{pmatrix} \hat{a}_1(E) \\ \vdots \\ \hat{a}_{\mathcal{N}}(E). \end{pmatrix} \tag{3.3}$$

From the conservation of particle flux in the system, we have that the scattering matrix

should be unitary:

$$S(E)S^{\dagger}(E) = \mathcal{I} \quad \Longrightarrow \quad \sum_{\beta=1}^{\mathcal{N}} |S_{\alpha\beta}(E)|^2 = 1. \tag{3.4}$$

In order to define the particle current flowing through the lead at some time $t$ and lead coordinate $\boldsymbol{r} = (x, y)$, it is first necessary to define field operators for electrons in the lead $\alpha$ as,

$$\hat{\Psi}_{\alpha}(t, \boldsymbol{r}) = \frac{1}{\sqrt{2\pi}} \int_0^{\infty} dE e^{-i\frac{E}{\hbar}t} \left( \hat{a}_{\alpha}(E) \frac{\psi_{\alpha}^{(\mathrm{in})}(E, \boldsymbol{r})}{\sqrt{\hbar v_{\alpha}(E)}} + \hat{b}_{\alpha}(E) \frac{\psi_{\alpha}^{(\mathrm{out})}(E, \boldsymbol{r})}{\sqrt{\hbar v_{\alpha}}(E)} \right), \tag{3.5}$$

where $v_{\alpha}(E) = \hbar k_{\alpha}/m$ denotes the electron's velocity. The particle current flowing in the lead $\alpha$ can then be expressed as [130–133]

$$\hat{I}_{\alpha}(t, x) = \frac{i\hbar}{2m} \int dy \left( \frac{\partial \hat{\Psi}_{\alpha}^{\dagger}(t, \boldsymbol{r})}{\partial x} \hat{\Psi}_{\alpha}(t, \boldsymbol{r}) - \hat{\Psi}_{\alpha}^{\dagger}(t, \boldsymbol{r}) \frac{\partial \hat{\Psi}_{\alpha}(t, \boldsymbol{r})}{\partial x} \right). \tag{3.6}$$

Upon inserting the definitions of the field operators, one finds that this expression for current will include terms which depend on two energies $E$ and $E'$. However, the situation can be significantly simplified by noting that when calculating observable quantities, such as average electronic and heat currents and their higher order moments, the corresponding expressions are dominated by terms for which the difference between these energies is small: $|E - E'| \ll E \sim \mu_0$, where $\mu_0$ is the Fermi energy [132]. Under this approximation, the energy dependence of the electron velocity follows $v_{\alpha}(E) \approx v_{\alpha}(E')$ and the particle current becomes

$$\hat{I}_{\alpha}(t) = \frac{1}{h} \iint dE dE' e^{i\frac{E-E'}{\hbar}t} \left( \hat{b}_{\alpha}^{\dagger}(E) \hat{b}_{\alpha}(E') - \hat{a}_{\alpha}^{\dagger}(E) \hat{a}_{\alpha}(E') \right). \tag{3.7}$$

In order to turn the particle current operator into a measurable quantity, one can calculate its expectation value $I_\alpha = \langle \hat{I}_\alpha(t) \rangle$, by taking the quantum statistical average over the state of the ingoing electrons. Our approach relies upon the assumption that the presence of the mesoscopic scattering sample does not affect the properties of the macroscopic reservoir from which any electron approaching the scatterer has arrived. Additionally, the reservoirs are assumed large enough to remain in their equilibrium state at all times and are uncorrelated with electrons in different wires [130]. Under these conditions, expectation values of ingoing particle operators take the form

$$\langle \hat{a}_\alpha^\dagger(E)\hat{a}_\alpha(E') \rangle = \delta_{\alpha\beta}\delta(E - E')f_\alpha(E), \tag{3.8}$$

where $f_\alpha(E)$ denotes the Fermi-Dirac distribution function for electrons in the reservoir $\alpha$:

$$f_\alpha(E) = \frac{1}{1 + e^{\frac{E-\mu_\alpha}{k_B T_\alpha}}}. \tag{3.9}$$

Here, $k_B$ is the Boltzmann constant and $\mu_\alpha$ and $T_\alpha$ represent the chemical potential and temperature in the reservoir of interest respectively. Using the definition of the scattering matrix given in Eq. 3.3, the expectation of the outgoing particle operators can also be expressed in terms of the distribution functions for ingoing states:

$$\begin{aligned} \langle \hat{b}_\alpha^\dagger(E)\hat{b}_\alpha(E') \rangle &= \sum_{\beta=1}^{\mathcal{N}} \sum_{\gamma=1}^{\mathcal{N}} S_{\alpha\beta}^*(E) S_{\alpha\gamma}(E') \langle \hat{a}_\alpha^\dagger(E)\hat{a}_\alpha(E') \rangle, \\ &= \sum_{\beta=1}^{\mathcal{N}} \sum_{\gamma=1}^{\mathcal{N}} S_{\alpha\beta}^*(E) S_{\alpha\gamma}(E') \delta(E - E')\delta_{\beta\gamma} f_\beta(E). \end{aligned} \tag{3.10}$$

Consequently, using the unitarity of the scattering matrix, the particle current can be

expressed as

$$I_\alpha = \frac{1}{h}\int dE \sum_{\beta=1}^{\mathcal{N}} |S_{\alpha\beta}(E)|^2 \Big(f_\beta(E) - f_\alpha(E)\Big). \tag{3.11}$$

Again using the fact that the scattering matrix is unitary, one can show that, in the case of a static sample, this particle current obeys the conservation law

$$\sum_{\alpha=1}^{\mathcal{N}} I_\alpha = 0. \tag{3.12}$$

Here, the positive direction of current flow is defined from the scatterer to the corresponding reservoir. This conservation law demonstrates that there is no accumulation of particles within the scattering centre.

The studies within this thesis are mainly be concerned with scattering systems in contact with just two particle reservoirs, referred to as 'left' ($L$) and 'right' ($R$) respectively. In this two-terminal scenario the scattering matrix will take the form

$$S(E) = \begin{pmatrix} r_{LL}(E) & t_{LR}(E) \\ t_{RL}(E) & r_{RR}(E) \end{pmatrix}. \tag{3.13}$$

Consequently, we see that only scattering events involving the transmission of particles between two different leads contribute to the current:

$$I_\alpha = \frac{1}{h}\int dE \mathcal{T}\Big(f_\beta(E) - f_\alpha(E)\Big), \tag{3.14}$$

with $\alpha \neq \beta = L, R$ and where $\mathcal{T}(E) = |t_{LR}(E)|^2 = |t_{RL}(E)|^2$ is the transmission probability between the two leads. The particle current can be used to calculate the electronic current, $I_\alpha^Q$, flowing in each of the leads as $I_\alpha^Q = eI_\alpha$. This in turn can be

utilised to find the differential conductance, $G_\alpha(V_\alpha) = dI_\alpha^Q/dV_\alpha$, for a voltage bias $V_\alpha$ in the lead $\alpha$. In the zero-temperature limit, this reduces to the well-known Landauer expression of conductance [129, 134]

$$G_{L/R}(V_\alpha) = \frac{e^2}{h}\mathcal{T}(V_\alpha - \mu_\alpha). \tag{3.15}$$

### 3.1.1 Scattering theory with superconductors

Here, we will outline how the scattering theory introduced in the previous section can be extended to the case for which our mesoscopic sample is superconducting [135–139]. This will allow for the study of transport properties of topological superconducting systems, such as the 1D Kitaev chain outlined in Sec. 2.2. The key difference that arises when superconducting pairing terms are introduced into our system Hamiltonian, is the need to treat particle and hole degrees of freedom explicitly due to the potential for incoming electrons to be reflected into a hole and vice versa. Such an event results in the injection of a Cooper pair into the superconducting sample and is known as Andreev reflection [140]. This necessitates the inclusion of an additional index when labeling the scattering states in each of the external leads. Concretely, we use $\hat{a}^\dagger_{\alpha^e}$ and $\hat{a}^\dagger_{\alpha^h}$ to denote operators creating electrons and holes traveling towards the scattering sample respectively. Similarly, $\hat{b}^\dagger_{\alpha^e}$ and $\hat{b}^\dagger_{\alpha^h}$ are used to describe the creation of the corresponding scattered states. The particle-hole symmetry present in superconducting systems dictates that the creation of a hole state at energy $E$, measured relative to the chemical potential of the superconductor, is equivalent to the annihilation of an electron with energy $-E$. This results in the following relationship between particle and hole

operators [133, 135]:

$$\hat{a}^{\dagger}_{\alpha^h}(E) = \hat{a}_{\alpha^e}(-E), \quad \hat{b}^{\dagger}_{\alpha^h}(E) = \hat{b}_{\alpha^e}(-E). \tag{3.16}$$

The relationship between the ingoing and scattered states in the leads is again encoded within the scattering matrix, which is now extended to include the particle-hole degrees of freedom, so that

$$\hat{b}_{\alpha^\gamma}(E) = \sum_{\delta=e,h} \sum_{\beta} S_{\alpha^\gamma \beta^\delta}(E) \hat{a}_{\beta^\delta}(E). \tag{3.17}$$

Transport quantities in the superconducting case can be calculated in much the same way as the case for which the mesoscopic sample is a normal metal conductor. However, now the relevant sign of contribution of the holes will depend upon whether we are considering charge or energy currents. Focusing here upon the case of charge current, the relevant operator can be expressed as [132]

$$\hat{I}^e_{\alpha}(t) = \frac{e}{h} \iint dE dE' e^{i\frac{E-E'}{\hbar}t} \Bigg( \hat{b}^{\dagger}_{\alpha^e}(E) \hat{b}_{\alpha^e}(E') - \hat{b}^{\dagger}_{\alpha^h}(E) \hat{b}_{\alpha^h}(E') \\ - \hat{a}^{\dagger}_{\alpha^e}(E) \hat{a}_{\alpha^e}(E') + \hat{a}^{\dagger}_{\alpha^h}(E) \hat{a}_{\alpha^h}(E') \Bigg). \tag{3.18}$$

The quantum-statistical average of the products of creation and annihilation operators for holes can be found by exploiting particle-hole symmetry:

$$\begin{aligned} f_{\alpha^h}(E) &= \left\langle \hat{a}^{\dagger}_{\alpha^h}(E) \hat{a}_{\alpha^h}(E) \right\rangle \\ &= \left\langle \hat{a}_{\alpha^e}(-E) \hat{a}^{\dagger}_{\alpha^e}(-E) \right\rangle = 1 - f_{\alpha^e}(-E). \end{aligned} \tag{3.19}$$

Hence, the distribution function for holes in the lead $\alpha$ takes the form

$$f_{\alpha^h}(E) = \frac{1}{1 + e^{\frac{E+\mu_\alpha}{k_B T}}}. \tag{3.20}$$

As we saw for the case of a normal system, these relations can be used to simplify the expression for the average electronic current flowing into the lead $\alpha$:

$$I_\alpha^Q = \frac{e}{h} \int dE \sum_{\beta=1}^{\mathcal{N}} \sum_{\gamma=e,h} |S_{\alpha^e \beta^\gamma}(E)|^2 \Big( f_{\beta^\gamma}(E) - f_{\alpha^e}(E) \Big) - \big|S_{\alpha^h \beta^\gamma}(E)\big|^2 \Big( f_{\beta^\gamma}(E) - f_{\alpha^h}(E) \Big). \tag{3.21}$$

## 3.2 Floquet scattering theory

The previous sections in this chapter have demonstrated the power of scattering matrix theory in simplifying the calculation of transport properties across static mesoscopic samples. Here, we show how this formalism can be extended to incorporate systems that are subject to some form of time dependent driving and, in particular, to Floquet systems for which this driving is periodic [130, 141–143]. Such non-equilibrium systems have been shown to exhibit a variety of properties and phases which are not present in their static counterparts [144–146]. For example, the emergence of additional driven topological phases will be of particular interest in the forthcoming chapters of this thesis [45–51].

Our starting point is the Floquet theorem, which states that for a system with a periodic Hamiltonian, with time-period $\mathcal{T}$,

$$H(t, \boldsymbol{r}) = H(t + \mathcal{T}, \boldsymbol{r}), \tag{3.22}$$

solutions to the time-dependent Schrödinger equation can be expressed in the form [130]

$$\Psi_\alpha(t,\boldsymbol{r}) = e^{-\frac{i\epsilon_\alpha t}{\hbar}}\psi_\alpha(t,\boldsymbol{r}), \tag{3.23}$$

where $|\psi_\alpha(t,\boldsymbol{r})\rangle$ is a periodic eigenstate of the effective Hamiltonian $H_{\text{eff}} = H(t,\boldsymbol{r}) - i\partial_t$,

$$H_{\text{eff}}(t,\boldsymbol{r})\,|\psi_\alpha(t,\boldsymbol{r})\rangle = \epsilon_\alpha\,|\psi_\alpha(t,\boldsymbol{r})\rangle\,. \tag{3.24}$$

Here, $\alpha$ is the band index and $\epsilon_\alpha$ are the *quasienergies* of the periodically driven system, in analogy with the *quasimomentum* characterizing the Bloch eigenstates of a spatially periodic system. The quasienergy $\epsilon_\alpha$ is unique up to multiples of the driving frequency $\hbar\omega_0$ and is therefore defined within the interval $-\pi/T < \frac{\epsilon_\alpha}{\hbar} \leq \pi/T$.

Expanding the periodic function $\phi(t,\boldsymbol{r})$ as a Fourier series, the Floquet wave function becomes

$$\begin{aligned} \Psi_\alpha(t,\boldsymbol{r}) &= e^{-\frac{i\epsilon t}{\hbar}} \sum_{q=-\infty}^{\infty} e^{-iq\omega_0 t}\psi_{\alpha,q}(\boldsymbol{r}), \\ \text{where}\quad \psi_{\alpha,q}(\boldsymbol{r}) &= \frac{1}{\mathcal{T}}\int_0^{\mathcal{T}} dt e^{iq\omega_0 t}\psi_\alpha(t,\boldsymbol{r}). \end{aligned} \tag{3.25}$$

In this form the effect of the periodic driving upon the wave functions becomes manifest. We see that the wave function now includes additional terms corresponding to the initial energy $\epsilon$ shifted by integer multiples of the driving frequency $E \pm q\hbar\omega_0$. In the context of scattering theory, this equates to inelastic scattering events resulting in the absorption or emission of energy quanta $\hbar\omega_0$.

The prospect of scattered particles exchanging energy with the driven mesoscopic sample means that the relevant scattering matrix for the problem now depends on two energies which differ by integer multiples of the energy quantum $\hbar\omega_0$. The details of such processes are captured by the *Floquet scattering matrix*, $S_F$ [130,141]. The element

$S_{F,\alpha^e\beta^e}(E_n, E)$ describes the process when an electron of energy $E$ in lead $\beta$ is scattered as an electron in lead $\alpha$ with a final energy of $E + n\hbar\omega_0$. The initial and resultant scattering states are assumed to be eigenstates of the stationary Hamiltonian of the leads.

As in the static case, conservation of particle flow implies that the Floquet scattering matrix is unitary:

$$\sum_{n=-\infty}^{\infty}\sum_{\alpha=1}^{\mathcal{N}} S^*_{F,\alpha\beta}(E_n, E_m)S^*_{F,\alpha\beta}(E_n, E) = \delta_{m0}\delta_{\beta\gamma} \tag{3.26}$$

Here, the sum over energy sidebands, $n$, runs from $-\infty$ to $\infty$ since we are considering superconducting systems for which electron and hole states at all energies contribute to the conductance. In order to determine the current operator for the periodically driven case, we first write down the operator for scattered states accounting for the fact that an outgoing electron may have exchanged energy with the dynamic scatterer:

$$\hat{b}_\alpha(E) = \sum_{n=-\infty}^{\infty}\sum_{\beta=1}^{\mathcal{N}} S^*_{F,\alpha\beta}(E, E_n)\hat{a}_\beta(E_n). \tag{3.27}$$

The periodic nature of the scattering properties in a Floquet system results in the generation of periodic oscillating currents between the leads. Using the definition of the outgoing scattering operators in Eq. 3.7, the current generated by a periodically driven scatterer can be expressed as

$$\begin{aligned} I^e_\alpha(t) &= \sum_{l=-\infty}^{\infty} e^{-il\omega_0 t} I^e_{\alpha,l}, \\ \text{where}\quad I^e_{\alpha,l} &= \frac{e}{h}\int dE \sum_{\beta=1}^{\mathcal{N}}\sum_{n=-\infty}^{\infty} S^*_{F,\alpha\beta}(E_n, E)S_{F,\alpha\beta}(E_{l+n}, E)\Big(f_\beta(E) - f_\alpha(E_n)\Big). \end{aligned} \tag{3.28}$$

Of particular interest is the time-independent, or direct, current that results in a finite transfer of charge between different leads. Within this formalism, this contribution can be isolated by focusing upon the $l = 0$ term in Eq. 3.28:

$$I^e_{\alpha,0} = \frac{e}{h}\int dE \sum_{n=-\infty}^{\infty}\sum_{\beta=1}^{\mathcal{N}} |S_{F,\alpha\beta}(E_n, E)|^2\Big(f_\beta(E) - f_\alpha(E_n)\Big). \tag{3.29}$$

When expressed in this form it becomes evident that the nature of the current is dictated by the difference in distribution functions $(f_\beta(E) - f_\alpha(E_n))$. Hence, for small frequencies relative to the chemical potential of the leads ($n_{\max}\hbar\omega_0 \ll \mu$), only electrons close to the Fermi energy contribute to the electronic current. Here $n_{\max}$ sets the maximum number of energy quanta that an electron can absorb/emit during a scattering process before the probability of such an event becomes negligible. This value is determined by the specific form of the Floquet scattering matrix in question and will depend upon the amplitude and frequency of the driving [130]. The energy window of current carriers can also be set by any potential biases between the leads, as well as the temperature of the selected leads.

### 3.2.1 Slow driving approximation of the Floquet scattering matrix

The possibility of scattering between energies differing by integer multiples of the driving frequency means that the Floquet scattering matrix has a very large number of elements and is hence difficult to calculate in practice. One possible method of combating the resultant numerical complexity is to consider situations for which the driving can be considered slow compared to other relevant energy scales in the problem. In this limit,

the time spent by an electron in the scattering sample is small compared to the driving period $\mathcal{T}$ and so, to all intents and purposes, the properties of the scatterer can be considered *frozen* throughout the scattering process.

With this in mind, for a given periodically driven system, we can define a stationary scattering matrix $S(t, E)$ that depends implicitly on time through several periodically modulated parameters $p_i,\ i = 1, ..., N_p$. This scattering is then itself time periodic, so that $S(t, E) = S(t+\mathcal{T}, E)$. This scattering matrix is *frozen* in the sense that if we fix the parameters $p(t)$ at some chosen time $t = t_0$, then the scattering matrix $S(t_0, E)$ would describe scattering from such a stationary or frozen system. This scattering matrix only depends upon a single energy and hence does not describe the true scattering properties of the dynamically driven system. However, connections can be drawn to the full Floquet scattering matrix in the slow driving limit. In order to see this, it is first useful to expand the Floquet scattering matrix in powers of the driving frequency [130, 141, 147]:

$$S_F = \sum_{q=0}^{\infty} (\hbar\omega_0)^q S_F^{(q)}. \tag{3.30}$$

We note that the scattering matrix element $S_{\alpha\beta}(E_n, E)$ induces a modification to the wave function of ingoing electrons of the form

$$\Psi_\beta^{(\text{in})}(E) \sim e^{-\frac{iEt}{\hbar}} \rightarrow \Psi_\alpha^{(\text{out})}(E_n) \sim S_{\alpha\beta}(E_n, E)\Psi_\beta^{(\text{in})}(E) \sim e^{-\frac{iEt}{\hbar}} e^{-in\omega_0 t}. \tag{3.31}$$

This can be compared with the action of the frozen scattering matrix, $\Psi_\alpha^{(\text{out})}(E) \sim S(t, E)\Psi_\beta^{(\text{in})}(E)$, in the case that we take the Fourier expansion of $S(t, E)$:

$$S(t, E) = \sum_{n=-\infty}^{\infty} e^{-in\omega_0 t} S_n(E). \tag{3.32}$$

From this, one can see that the scattered wave function inherits the same factor of $e^{-in\omega_0 t}$ as from the Floquet scattering matrix element $S_{\alpha\beta}(E_n, E)$. To zeroth order in $\omega_0$, the energies $E$ and $E_n$ can be considered equivalent and therefore the comparison between the effects of the Floquet and frozen scattering matrices yields

$$S_F^{(0)}(E_n, E) = S_F^{(0)}(E, E_{-n}) = S_n(E). \tag{3.33}$$

It will become apparent in the later chapters of this work that this zeroth order approximation of the Floquet scattering matrix is sufficient to exactly determine the direct current generated by a driven scatterer to first order in $\omega_0$.

It will also prove useful to consider the first order terms in the expansion in Eq. 3.30. Given the form of the zeroth order approximation in Eq. 3.33, it can be shown that [142], up to first order, the expansion can be expressed as

$$\begin{aligned} S_F(E_n, E) &= S_n(E) + \frac{n\hbar\omega}{2}\frac{\partial S_n(E)}{\partial E} + \hbar\omega A_n(E) + \mathcal{O}\big(\omega^2\big), \\ S_F(E, E_{-n}) &= S_n(E) - \frac{n\hbar\omega}{2}\frac{\partial S_n(E)}{\partial E} + \hbar\omega A_n(E) + \mathcal{O}\big(\omega^2\big). \end{aligned} \tag{3.34}$$

Here, $A_n$ denotes the Fourier coefficients of some matrix $A(t, E)$ which, by enforcing the unitarity of the Floquet scattering matrix, can be shown to share the following relationship with the frozen scattering matrix [130]:

$$\hbar\omega_0\Big[S^\dagger(t, E)A(t, E) + A^\dagger(t, E)S(t, E)\Big] = \frac{1}{2}P\Big\{S^\dagger(t, E), S(E, t)\Big\}, \tag{3.35}$$

where $P\Big\{S^\dagger(t, E), S(E, t)\Big\}$ denotes the Poisson bracket with respect to energy and

time:

$$P\Big\{S^\dagger(t,E), S(E,t)\Big\} = i\hbar\left(\frac{\partial S^\dagger}{\partial t}\frac{\partial S}{\partial E} - \frac{\partial S^\dagger}{\partial E}\frac{\partial S}{\partial t}\right). \tag{3.36}$$

The expression of the Floquet scattering matrix expansion in Eq. 3.34 reveals the form of the parameter that must be small in order to neglect the higher order terms. The use of the first order expansion requires that

$$\frac{\hbar\omega_0}{\delta E} \ll 1. \tag{3.37}$$

Here, $\delta E$ is the energy scale over which the frozen scattering matrix changes significantly. This may refer to the width of resonances or the distance between resonances depending upon the relevant energy $E$.

## 3.3 Symmetry classes and scattering matrices

In Chap. 2, we outlined how the principle of bulk-boundary correspondence demonstrates that topological invariants $\mathcal{Q}$, obtained from the bulk properties of some system, are related to the number of zero-energy conducting states localized at the edges of the system. Upon opening such a topologically non-trivial system, by connecting it to external metal leads, the presence or absence of edge modes will influence the scattering properties of electrons approaching the sample. This, in turn, provides a connection between the bulk topological invariant $\mathcal{Q}$ and the scattering matrix $S$ [41].

In order to demonstrate this connection, we consider the simple example of the interface between a normal metal wire and a topologically non-trivial superconducting wire capable of hosting Majorana zero modes at its ends. At energies far below the superconducting gap parameter $\Delta$, there are no states available to aid transmission

scattering events across the superconducting sample and consequently the only non-trivial elements of the scattering matrix are given by the sub-block governing scattering events within the same lead. For a superconducting system, this reflection matrix $r(E)$ can be written as

$$r_\alpha(E) = \begin{pmatrix} r_{ee} & r_{eh} \\ r_{he} & r_{hh} \end{pmatrix}. \tag{3.38}$$

Particle conservation once again ensures that this matrix is unitary $r^\dagger r = 1$. The particle-hole symmetry of the Hamiltonian (Eq. 2.13) results in a corresponding symmetry of the reflection matrix $r(E)$:

$$\sigma_x r^*(-E)\sigma_x = r(E). \tag{3.39}$$

This symmetry constrains the determinant of the reflection matrix at zero energy to be real since

$$\det r(0) = \det\left(\sigma_x r^*(0)\sigma_x\right) = \left(\det r(0)\right)^*. \tag{3.40}$$

This, along with the fact that $r(E)$ is unitary, constraints the determinant to take one of two possible values: $\det r(0) = \pm 1$. Furthermore, since this conclusion was attained using only the fundamental symmetries of the system, the determinant of $r(0)$ cannot be changed by continuous deformations of the Hamiltonian that preserve the energy gap. In fact, the determinant can only change upon the closing of this energy gap, due to the existence of possible transmission scattering events which violate the unitarity of the reflection matrix. Therefore, it is clear that the quantity $\mathcal{Q} = \det r(0)$ fulfills the requirements of a topological invariant for the system. The topological properties of the scattering matrix are also evident in the electronic transport induced by the scatterer.

| Symmetry | | | | Topology | |
|---|---|---|---|---|---|
| Class | $\chi$ | $\mathcal{C}$ | $\mathcal{T}$ | Phase | Scattering Index |
| D | 0 | 1 | 0 | $\mathbb{Z}_2$ | $\operatorname{sign}\det r$ |
| DIII | 1 | 1 | -1 | $\mathbb{Z}_2$ | sign Pf $ir$ |
| BDI | 1 | 1 | 1 | $\mathbb{Z}$ | $\nu(r)$ |
| AIII | 1 | 0 | 0 | $\mathbb{Z}$ | $\nu(r)$ |
| CII | 1 | -1 | -1 | $2\mathbb{Z}$ | $\nu(r)$ |

Table 3.1: Relationship between the topological invariant $\mathcal{Q}$ and the reflection submatrix $r$ for each of the possible symmetry classes for 1D systems exhibiting topologically non-trivial phases. For $\mathbb{Z}_2$ topological phases, the corresponding invariant is given either by the determinant (det) or Pfaffian (Pf) of $r$, whereas for $\mathbb{Z}$ phases the relevant quantity is given by the number $\nu$ of negative eigenvalues of $r$

The symmetry and unitary nature of the reflection matrix enforce the following simultaneous relationships upon the normal and Andreev reflection coefficients:

$$\begin{aligned} \mathcal{Q} =& |r_{ee}|^2 - |r_{eh}|^2 = \pm 1, \\ & |r_{ee}|^2 + |r_{eh}|^2 = 1. \end{aligned} \tag{3.41}$$

There are only two scenarios for which both of these requirements hold true. The first is the trivial case, where $|r_{ee}| = 1$ and we have perfect normal reflection resulting in no electronic transport between different leads. The second corresponds to the superconductor being in the topological phase and the presence of the MZMs leads to perfect Andreev reflection, $|r_{eh}| = 1$. Since, at low energies, only Andreev reflection events result in the transfer of charge between the leads, it follows that the conductance in a given lead $\alpha$ takes the form

$$G_\alpha(V_\alpha) = \frac{2e^2}{h}|r_{eh}(V)|^2. \tag{3.42}$$

Consequently, the existence of MZMs in the scattering sample is associated with a

quantised conductance peak at $V = 0$ of height $G(0) = \frac{2e^2}{h}$. This peak shares the robustness of the topological index $\mathcal{Q}$ and can only change upon the closure of the energy gap.

This example demonstrates the power of the scattering matrix as a tool for determining topological indices. This method circumvents the need for knowledge of the full spectrum of a given Hamiltonian, by reducing the problem to the scattering properties of the system at the Fermi level only. This approach has been extended to all of the symmetry classes listed in Table 2.1. Here, we will not include the details of the scattering matrix invariants for each class, however Table 3.1 includes the form of the invariant for each of the five non-trivial classes in 1D for reference [41].

# Chapter 4

# Transport Statistics in Non-equilibrium Systems

## 4.1 Introduction to fluctuation theorems

The thermodynamic properties of equilibrium systems, free from the subjection to thermodynamic forces or time-dependent driving, are well understood and the probability distribution governing their microscopic degrees of freedom can be easily formulated. The Hamiltonian, dictating the evolution of such systems, can be used to determine the partition function from which macroscopic, experimentally accessible thermodynamic quantities, such as average energy and specific heat, can be calculated.

However, the situation for non-equilibrium systems is far from as simple. Furthermore, such systems are prevalent in nature and arise in the presence of temperature and chemical potential gradients, in addition to the application of time-dependent external driving; the main focus of this thesis. Close to equilibrium, when the forces in question can be considered weak, the deviation of the system's properties with respect to the

unperturbed values can be calculated via linear response functions [148–150]. Despite this, analogous expressions valid arbitrarily far from equilibrium prove to be much more elusive.

Fluctuation theorems (FTs) provide information about non-equilibrium systems beyond the linear response regime by severely restricting the form of the probability distributions for thermodynamic quantities, such as work and entropy production, that are known to fluctuate at a microscopic level. Such relations describe the connection between the probability distribution functions associated with the forward, $P_F(x)$, and time-reversed, $P_R(x)$ processes and are typically expressed in the form [151]

$$\frac{P_F(x)}{P_R(-x)} = e^{a(x-b)}, \tag{4.1}$$

where $x$ is our fluctuating quantity of interest and $a$ and $b$ are constants determined by the equilibrium nature of the system.

## 4.2 Quantum fluctuation relations

Within the quantum setting, we are concerned with isolated systems, driven out of equilibrium, which can be described by a density matrix $\rho(t)$ obeying the von Neumann equation:

$$\frac{d}{dt}\rho(t) = -\frac{i}{\hbar}[H(t), \rho(t)]. \tag{4.2}$$

The solution to this expression takes the form

$$\rho(t) = U(t,0)\rho_0 U^\dagger(t,0), \tag{4.3}$$

where $\rho_0$ is the density matrix describing the system at $t = 0$ and the unitary evolution operator reads

$$\begin{aligned} U(t,0) &= \exp_+\left( -\frac{i}{\hbar}\int_0^t d\tau H(\tau)\right) \\ &\equiv 1 + \sum_{n=1}^{\infty}\Big(-\frac{i}{\hbar}\Big)^n \int_0^t dt_1 \int_0^{t_1} dt_2 ... \times \int_0^{t_{n-1}} dt_n H(t_1)H(t_2)...H(t_n), \end{aligned} \tag{4.4}$$

with the subscript + indicating the use of an anti-chronological time ordering from left to right.

Generalising the notion of the work performed on a system to the quantum regime was a concept that initially caused some difficulties in the development of quantum fluctuation relations [152]. Unlike other observables, which are defined by operators which can be measured at any single time, work is a two-point quantity obtained by finding the difference between the initial and final energy of the system after being allowed to evolve for some time interval [151, 153].

With this in mind, we now consider some general observable $A(t)$, with eigenvalues $a_t$ and eigenstates $|a_t\rangle$. We then imagine performing two consecutive measurements of $A(t)$ and define the joint probability of measuring $a_0$ at time 0 and $a_t$ at some later time $t$:

$$P[a_t, a_0] \equiv \mathrm{Tr}\left[P_{a_t} U(t,0) P_{a_0} \rho_0 P_{a_0} U^\dagger(t,0) P_{a_t}\right], \tag{4.5}$$

with projective measurement operators defined as $P_{a_t} = |a_t\rangle\langle a_t|$. This can also be expressed in the form

$$P[a_t, a_0] = \sum_{i,j} P[j, a_t; i, a_0], \tag{4.6}$$

where the indices $i$ and $j$ are used to distinguish degenerate energy states sharing the

same eigenvalue. Using Eq. 4.5, the joint probability accounting for the degenerate eigenstates is given by

$$P[j, a_t; i, a_0] = |\langle j, a_t|U(t,0)|i, a_0\rangle|^2 \langle i, a_0|\rho_0|i, a_0\rangle . \tag{4.7}$$

The time-reversed evolution is defined as the process that brings the final density matrix of the forward evolution back to its initial density matrix $\rho_0$. It can be shown that [151], the probability of measuring $a_t$ initially and $a_0$ after the application of the time-reversed evolution protocol for some time time $t$, can be expressed as

$$P^{\mathrm{tr}}[i, a_0; j, a_t] = |\langle j, a_t|U(t,0)|i, a_0\rangle|^2 \langle j, a_t|\rho_0|j, a_t\rangle . \tag{4.8}$$

The quantity of interest in the general form of FTs is the logarithm of the ratio of the forward and time-reversed probabilities:

$$R[j, a_t; i, a_0] \equiv \ln \frac{P[j, a_t; i, a_0]}{P^{\mathrm{tr}}[i, a_0; j, a_t]} = \ln \frac{\langle i, a_0|\rho_0|i, a_0\rangle}{\langle j, a_t|\rho_0|j, a_t\rangle}, \tag{4.9}$$

where we have used the expressions for the probabilities given in Eqs. 4.7 and 4.8. This immediately allows the determination of the *integral* FT, which takes the form

$$\langle e^{-R}\rangle = \sum_{j,a_t,i,a_0} P[j, a_t; i, a_0] e^{-R[j,a_t;i,a_0]} = \sum_{j,a_t,i,a_0} P^{\mathrm{tr}}[i, a_0; j, a_t] = 1, \tag{4.10}$$

following from the normalisation condition of the joint probability distribution $P^{\mathrm{tr}}[i, a_0; j, a_t]$. The fluctuation theorem can be expressed in an alternative formalism by introducing

the probability distributions associated with the forward and reversed evolution:

$$\begin{aligned} P(R) &= \sum_{j,a_t,i,a_0} P[j,a_t;i,a_0]\delta(R - R[j,a_t;i,a_0]), \\ P^{\mathrm{tr}}(R) &= \sum_{i,a_0,j,a_t} P^{\mathrm{tr}}[i,a_0;j,a_t]\delta(R - R^{\mathrm{tr}}[i,a_0;j,a_t]), \end{aligned} \tag{4.11}$$

where

$$R^{\mathrm{tr}}[i,a_0;j,a_t] \equiv \ln \frac{P^{\mathrm{tr}}[i,a_0;j,a_t]}{P[j,a_t;i,a_0]}. \tag{4.12}$$

From this we can write down the general form of the so-called *detailed* FT:

$$\ln \frac{p(R)}{p^{\mathrm{tr}}(-R)} = R. \tag{4.13}$$

### 4.2.1 Jarzynski and Crooks relations

To put the general form of the FT given in Eq. 4.13 into some physical context, we here consider the case for which our quantity of interest is the work performed on some isolated system by an arbitrary external source of driving [154, 155]. Our system is initially described by the Hamiltonian $H(0)$ and is assumed to be in an equilibrium state described by the density matrix $\rho_0 = e^{-\beta H(0)}/Z(0)$, where $Z(t) = \mathrm{Tr}\, e^{-\beta H(t)}$. At $t = 0$ the energy is measured before being subjected to driving up until a later time $t$, when a second energy measurement is performed. The corresponding backward process can be described by allowing the system to thermalise after the second measurement, so that we arrive at the equilibrium state, $\rho_0^{\mathrm{tr}} = e^{-\beta H(t)}/Z(t)$, of the system described by $H(t)$, and then taking another measurement of the energy. We then proceed to apply the time-reversed driving protocol to the system, before taking a final measurement of the energy after a time $t$ has passed, with the final Hamiltonian returning to $H(0)$.

Using Eqs. 4.7 and 4.8, the probabilities associated with the two-point energy measurements for the forward and reverse processes can be expressed as

$$\begin{aligned} P[j, E_t; i, E_0] &= |\langle j, E_t|U(t,0)|i, E_0\rangle|^2 e^{-\beta\left(E_0 - F(0)\right)}, \\ P^{\mathrm{tr}}[i, E_0; j, E_t] &= |\langle j, E_t|U(t,0)|i, E_0\rangle|^2 e^{-\beta\left(E_t - F(t)\right)}, \end{aligned} \tag{4.14}$$

and the expression for the quantity $R$ is given by

$$R[j, E_t; i, E_0] = \beta\big(w - \Delta F(t)\big). \tag{4.15}$$

Here we have defined the work done on the isolated system by the external driving as the difference in the energy measurements of the final and initial states; $w = E_t - E_0$. The free-energy difference is given by $\Delta F(t) = F(t) - F(0)$, where $F(t) = -\beta^{-1} \ln Z(t)$. Written in this form we see that the quantity $\beta^{-1}\langle R\rangle$ can be associated with the irreversible contribution to the entropy change of the process, a property shared by all manifestations of fluctuation theorems. The general form of the FT in Eq. 4.13 now takes the form of the Crooks relation [156]:

$$\frac{p(w)}{p^{\mathrm{tr}}(-w)} = e^{\beta(w - \Delta F)}, \tag{4.16}$$

which relates non-equilibrium work with the equilibrium free energy difference. From this relation, the Jarzynski equality [154] immediately follows:

$$\langle e^{-\beta w}\rangle = e^{\beta \Delta F}. \tag{4.17}$$

### 4.2.2 Steady state exchange fluctuation theorem

Fluctuation theorems can also be formulated to describe fluctuations in entropy production [157, 158] and various related quantities such as the heat exchange between two reservoirs via some embedded system of interest [159–161]. Fluctuation theorems of this form can also be extended to be valid in the long-time limit and are hence known as steady-state FTs. We study FTs of this form in Chap. 6, in the context of heat transport driven by the periodic modulation of a system's parameters.

In general, we can consider two reservoirs $A$ and $B$, described by Hamiltonians $H_A$ and $H_B$, each with inverse temperature $\beta_{A/B}$ and chemical potential $\mu_{A/B}$. The reservoirs are weakly coupled to a system of interest, described by the Hamiltonian $H_S$, which facilitates the transport of energy and particles between the reservoirs. We assume that the initial states of this composite system, for both the forward and time-reversed processes, are described by the equilibrium density matrix [151]

$$\rho_0 = \rho_0^{\mathrm{tr}} = \rho_A^{\mathrm{eq}}(\beta_A, \mu_A)\rho_B^{\mathrm{eq}}(\beta_B, \mu_B)\rho_S^{\mathrm{eq}}(\beta_S, \mu_S). \tag{4.18}$$

After an initial measurement of both energy $E_A$ and particle number $n_A$ in reservoir $A$, the system is allowed to evolve up until a second measurement at some time $t$. We denote the measurement outcomes of the combined system using $\alpha = (E_A, n_A, E_B, n_B, E_S, n_S)$ so that, in this scenario, Eq. 4.9 gives us

$$\begin{aligned} R[\alpha', \alpha] = &- \beta_A[(E_A - E'_A) - \mu_A(n_A - n'_A)] \\ &- \beta_B[(E_B - E'_B) - \mu_B(n_B - n'_B)] - \beta_S[(E_S - E'_S) - \mu_S(n_S - n'_S)]. \end{aligned} \tag{4.19}$$

For a weakly coupled system, conservation laws for energy and particle number result

in the following constraints on the respective changes in the constituent parts of the composite system:

$$E_B - E'_B \approx E'_A - E_A + E'_S - E_S \quad \text{and} \quad n_B - n'_B = n'_A - n_A + n'_S - n_S. \tag{4.20}$$

Under these constraints, the ratio of probabilities for the forward and reversed processes can be simplified as

$$R[E'_A, n'_A; E_A, n_A] \approx -\mathcal{A}_Q(E'_A - E_A) - \mathcal{A}_N(n'_A - n_A) + \mathcal{O}(E'_S - E_S) + \mathcal{O}(n'_S - n_S), \tag{4.21}$$

where we have defined $\mathcal{A}_Q = \beta_B - \beta_A$ and $\mathcal{A}_N = \beta_A\mu_A - \beta_B\mu_B$ as the affinities associated with heat and matter transport respectively.

The fact that the reservoirs $A$ and $B$ are considered macroscopic sources of particles and energy means that the changes in energy and matter that they experience over long time intervals in unbounded. This is in contrast to the internal mesoscopic system of interest which is small and finite. Consequently, in the steady state limit, $t \to \infty$, the FT describing heat and matter flow from the reservoir $A$ can be reduced to [151, 153]

$$\lim_{t\to\infty} \frac{1}{t} \ln \frac{p(\Delta E_A, \Delta n_A)}{p(-\Delta E_A, -\Delta n_A)} = \frac{1}{t}\big(\mathcal{A}_Q \Delta E_A + \mathcal{A}_N \Delta n_A\big). \tag{4.22}$$

From this exchange FT it is evident that positive $\mathcal{A}_Q$ ($\mathcal{A}_N$) indicates that the probability of an energy transfer $\Delta E_A$ (particle transfer $\Delta n_A$) from reservoir $A$ to reservoir $B$ is exponentially more likely to occur than from $B$ to $A$. The right-hand side of Eq. 4.22 takes the form of an entropy production and fluctuation relations of this kind are known generally as Gallavotti-Cohen (GC) type FTs [158]. When focusing on the nature of

heat transport between two reservoirs only, the relation reduces to the expression:

$$\lim_{t\to\infty} \frac{1}{t} \ln \frac{p(\Delta E)}{p(-\Delta E)} = \frac{\Delta E(\beta_R - \beta_L)}{t}. \tag{4.23}$$

In Chap. 6 we explore the validity of this expression in the case that the internal system is subjected to a source of slow, periodic driving. For such a scenario, the conservation law constraining the energy changes within each part of the system (Eq. 4.20) no longer holds true, since the driving itself acts as an additional energy source/sink. This exchange of energy can facilitate the driving of heat against a thermal gradient and hence results in a correction to the fluctuation relation in Eq. 4.23 [58–62].

# Part II

# Original Results

# Chapter 5

# Transport Properties of Floquet Majorana Systems

This chapter is based upon the results published in the paper:
T. Simons, A. Romito, and D. Meidan. *Relation between scattering matrix topological invariants and conductance in Floquet Majorana systems.* Phys. Rev. B **104**, 155422 (2021)

In Chap. 2 we discussed how, under certain conditions, $p$-wave superconducting structures can play host to zero-energy excitations known as Majorana zero modes. Their stability and non-Abelian nature ensure that such excitations receive great attention, particularly in relation to their potential application within a quantum computation setting. Building systems capable of hosting such a topologically non-trivial phase is experimentally challenging and hence exploring alternative mechanisms capable of achieving this goal are of great interest.

One possible direction is to exploit the emergent properties of systems driven out of

equilibrium by some source of periodic driving. It is known that such *Floquet* systems can exhibit a variety of distinct properties, for which there is no evidence of in their static counterparts [144–146]. These properties can be tuned solely by the driving, in contrast to equilibrium systems, for which they are intrinsic to the setup and hard to change in situ. In particular it is known that periodic driving can result in the emergence of additional topological phases, even in the case that the system is trivial at any given point during the cycle [45, 47–51].

The calculation of topological invariants, such as the Chern number defined in Eq. 2.4, from the bulk properties of the system cannot be straightforwardly generalised from the case of static to periodically driven systems [47, 52, 53]. However, the principle of bulk-boundary correspondence, and resulting existence of gapless surface modes, ensures that scattering properties continue to provide a reliable method for calculating topological invariants. In contrast to static systems, it has been shown [53] that the invariants of periodically driven systems are related to a *gedanken* scattering experiment, for which the leads are only coupled to the system at discrete times separated by the driving frequency. Despite this, the exact relationship between this stroboscopic scattering matrix and the DC transport properties measured in conductance experiments remains unclear and forms the subject of this chapter.

## 5.1 Floquet topological phases

In order to see how such phases can arise, we first use the Floquet theory introduced in Sec. 3.2 to study the stationary solutions of a periodically driven system described by a Hamiltonian of the form $H(t+T) = H(t)$, where $T$ is the period of the driving acting with frequency $\omega = 2\pi/T$.

The quasienergy spectrum can be determined by considering the unitary evolution operator $U(t,0)\,|\psi_\alpha(0)\rangle = |\psi_\alpha(t)\rangle$, and in particular the Floquet operator which gives the evolution over one entire period of the driving cycle, $F = U(T,0)$. From this we can construct the Floquet Hamiltonian:

$$H_F = \frac{i}{T}\log(F), \tag{5.1}$$

the eigenspectrum of which provides access to the quasienergies $\epsilon_\alpha$,

$$H_F\,|\psi_\alpha(0)\rangle = \epsilon_\alpha\,|\psi_\alpha(0)\rangle\,. \tag{5.2}$$

Similar to the case of static systems, we can determine the bulk quasienergy spectrum of a periodically driven system by applying spatial periodic boundary conditions and determining the momentum space Hamiltonian $\mathcal{H}(k)$.

For example, we can consider the case of a driven Kitaev wire, where the system Hamiltonian is of the form given in Eq. 2.12, with $\mu = \mu_1$ for $0 \leq t < T/2$ and $\mu = \mu_2$ for $T/2 \leq t < T$. Such a driving scheme is desirable from an experimental perspective since it requires the control of only a single Hamiltonian parameter and the modulation of the on-site potential can be achieved in $p$-wave superconducting systems by driving the gates controlling the electrostatic environment [162–164]. Furthermore, it is not a strict requirement that the value of $\mu$ be changed stroboscopically as it has been demonstrated that the emergence of non-trivial phases persists when the driving is performed in a sinusoidal manner [163].

Examples of the resultant quasienergy spectrum are plotted in Fig. 5.1. The particle-hole symmetry present in the system again results in a spectrum that is

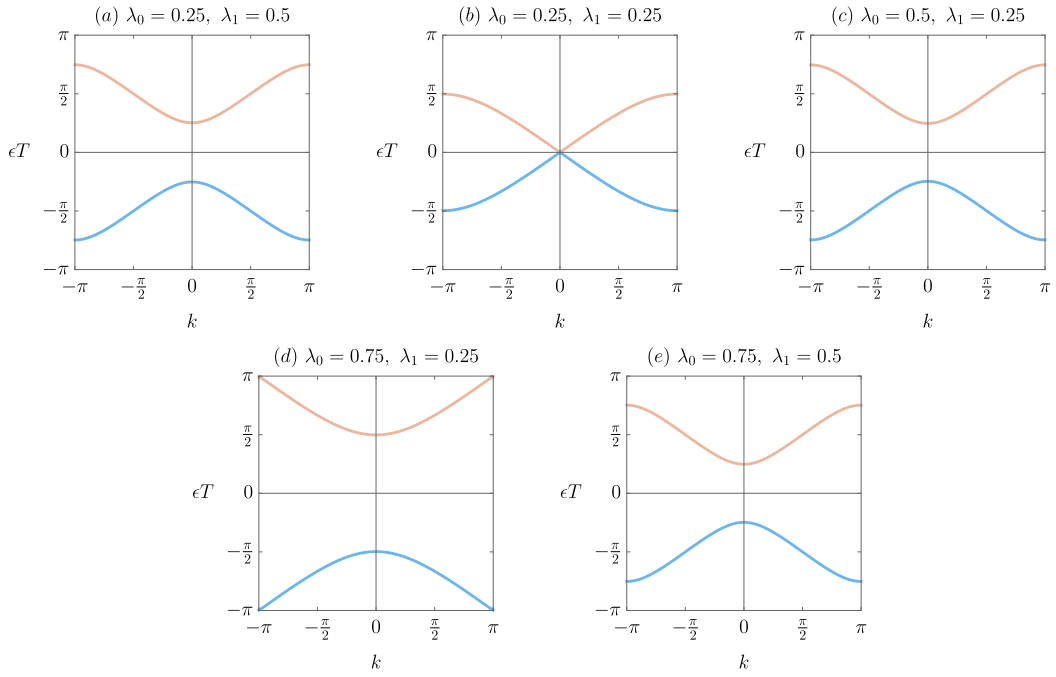


Figure 5.1: (a)-(e) Quasienergy band structure of a driven 1D Kitaev chain for various values of the Hamiltonian parameters. The driving protocol is outlined in Sec. 5.4.1 and the phase diagram corresponding to the parameters $\lambda_0$ and $\lambda_1$ is plotted in Fig. 5.3. The fact that the quasienergy is defined periodically results in the existence of two relevant energy gaps in the system, at $\epsilon T = 0$ and $\epsilon T = \pi$. These gaps close in (b) and (d) respectively, indicating a topological phase transition.

symmetric around $\epsilon = 0$, with eigenstates fulfilling $\psi_k(\epsilon) = \psi^\dagger_{-k}(-\epsilon)$. However, due to the periodic nature of the quasienergy spectrum, $\epsilon = \pi/T$ is an additional point mapped onto itself by the symmetry transformation $\epsilon \to -\epsilon$. Consequently, this results in a second relevant energy gap in the system when it comes to topological classification. As in the case of Majorana zero modes, wavefunctions at quasienergy $\epsilon = \pi/T$ also exhibit the property of being their own anti-particle $\psi = \psi^\dagger$ and can only be removed by the closing of the band gap at this energy. Such excitations are known as Majorana $\pi$-modes (MPMs) [46, 165–170] and their existence provides a clear example of how the periodic driving of a system can add to the richness of its topological order.

Furthermore, the fact that the presence of such Majorana modes can be controlled by tuning the versatile external driving protocol, holds promise for a wide range of potential applications [171–173]. In particular the driven Kitaev wire has been stipulated as a potential candidate for demonstrating a topologically protected Majorana braiding operation (Sec. 2.4) within a single 1D wire by utilizing the quasienergy as an effective second dimension [163, 174].

The realization and manipulation of such driven topological phases would require overcoming several experimental challenges. In particular it is known that, in generic interacting systems, subjection to periodic driving results in heating to infinite temperature, rendering any topological Floquet states unstable. Several mechanisms of how to avoid or suppress such heating have been stipulated, such as many-body localization and prethermalization [175, 176]. It has further been demonstrated that, for interacting systems, the switching on of the driving can stimulate the production of unwanted quasiparticles, again leading to the instability of the Floquet system [177]. Driven systems would also be subject to the same limitations as their static counterparts, such as the issue of quasiparticle poisoning, when considered as candidates for performing topologically protected quantum computation. Although several proposals of how to realize Floquet Majorana states in practice do exist [51, 164, 178], these are yet to be demonstrated in experiments.

## 5.2 Model Hamiltonian

With the objective of studying the electronic transport properties of periodically driven topological systems, we consider the setup sketched in Fig. 5.2(a). Our system of interest is driven via the periodic modulation of its Hamiltonian parameters $\{X_i(t)\}$

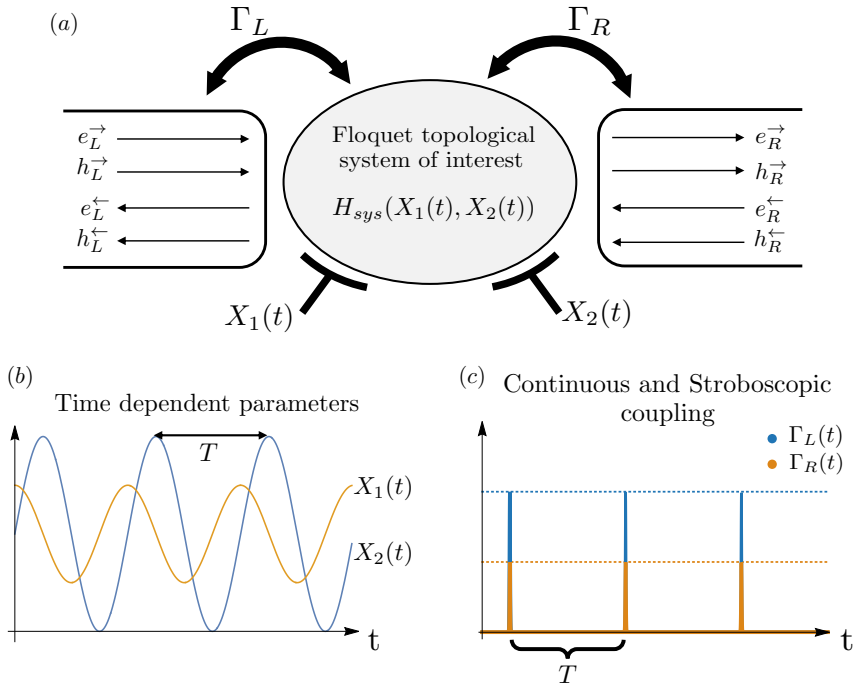


Figure 5.2: (a) Schematic of an electronic system connected to two external leads (terminals) via tunneling rates $\Gamma_L, \Gamma_R$ and driven via periodic control of its parameters $X_1, X_2$, the time dependence of which are sketched in (b). Each terminal $(L, R)$ includes ingoing and outgoing $(\leftarrow, \rightarrow)$ electron $(e)$ and hole $(h)$ scattering states. (c) Two scattering scenarios are depicted, corresponding to either a continuous coupling to the leads (dashed lines) or time-pulsed couplings with periodicity $T$ (solid lines).

(Fig. 5.2(b)), and is coupled to two electron reservoirs, labeled $L$ and $R$, via metallic leads. The relevant Hamiltonian therefore consists of three parts:

$$H = H_{\rm sys}(t) + H_{\rm T} + H_{\rm lead}, \tag{5.3}$$

where $H_{\rm sys}(t) = \sum_{j,k=1}^{N} c_j^{\dagger} h_{j,k}(t) c_k$ is the Hamiltonian of the system of interest, which is assumed to be a generic non interacting system of local fermionic degrees of freedom

annihilated by the operator $c_j$. The coupling to the external leads is captured by

$$H_T = \sum_{\alpha,k} \left[ \sqrt{\Gamma_\alpha} a^\dagger_{\alpha,k} K_\alpha c_{j_\alpha} + h.c. \right], \tag{5.4}$$

where $K_\alpha$ is the contact matrix between the system and the lead $\alpha$, with $\Gamma_\alpha$ characterizing the coupling strength, and $c_{j_\alpha}$ annihilating a particle in the mode $j_\alpha$. In a system modeled by spatially discretized sites, $j_\alpha$ labels the spatial coordinate of the system's site closest to lead $\alpha$. Finally, the metallic leads are modeled as generic free fermion reservoirs with constant density of states and linear dispersion:

$$H_\alpha = v_\alpha k \sum_k [a^\dagger_{\alpha,k} a_{\alpha,k} - b^\dagger_{\alpha,k} b_{\alpha,k}], \tag{5.5}$$

where $a_{\alpha,k}$ and $b_{\alpha,k}$ annihilate ingoing and outgoing particles with momentum $k$ in the reservoir $\alpha = L, R$. The creation/annihilation operators for energy eigenstates in each lead can be identified with the momentum creation operators, e.g. $b_L(E) \equiv b_{L,k}$ and $a_L(E) \equiv a_{L,k}$ via $E = \pm v_L k$ respectively.

## 5.3 Conductance for different system-lead couplings

In order to explore the connection between transport properties and topological classification in driven systems, we will consider two distinct coupling configurations, the behaviour of which are plotted in Fig. 5.2(c). Firstly we examine the case of constant coupling to the leads, as is typical in transport measurement setups, before comparing this to the scenario with $\delta$-like pulsed coupling, which is of importance for determining the scattering matrix topological invariants of the system.

### 5.3.1 Constant couplings

Using the Floquet scattering matrix $S$, one can express the time-averaged electronic current in the lead $\alpha$ by rearranging the expression introduced in Eq. 3.29 [141, 142]:

$$I_\alpha^e = \frac{e}{h}\int_{-\infty}^{\infty} dE \sum_{\beta\neq\alpha}\sum_n \left[|S_{\alpha\beta}(E_n,E)|^2 f_\beta(E) - |S_{\beta\alpha}(E_n,E)|^2 f_\alpha(E)\right]. \tag{5.6}$$

Here, $f_\alpha(E)$ gives the distribution function of particles entering the scatterer through the channel $\alpha$. In order to keep this formalism general for superconducting systems, the channels run over both particle and hole degrees of freedom in each of the external leads, $\alpha, \beta \in \{L^e, L^h, R^e, R^h\}$.

The current can subsequently be used to find the differential conductance in each lead via the derivative with respect to the voltage bias $V_\alpha$: $G_\alpha(V_\alpha) = dI_\alpha^e/dV_\alpha$. For simplicity we consider a symmetric voltage bias, $V$, with respect to the Fermi level of the superconductor, so that the corresponding Fermi distribution functions are given by: $f_{L^e} = f(E-eV)$, $f_{L^h} = f(E+eV)$, $f_{R^e} = f(E+eV)$ and $f_{R^h} = f(E-eV)$. In the zero temperature limit, the Fermi distribution functions reduce to step functions and hence the conductance in the left lead for example, reads

$$G_L(V) = G_{L^eL^h}(-V) + G_{L^eR^e}(-V) - G_{L^eR^h}(V) + \sum_{\beta\neq\alpha} G_{\beta L^e}(V), \tag{5.7}$$

where the contribution to the conductance from each element of the scattering matrix takes the form

$$G_{\alpha\beta}(V) = \frac{e^2}{h}\sum_n |S_{\alpha\beta}(V_n,V)|^2. \tag{5.8}$$

In order to determine the form of the Floquet scattering matrix we employ a

Green's function approach. To this end, we note that the evolution of the driven scattering sample, along with coupled leads, is captured by the effective non-Hermitian Hamiltonian $H_{\rm sys}(t) - i\Sigma$, where $\Sigma = \frac{1}{2}\sum_\delta \Gamma_\delta K_\delta^\dagger K_\delta$ is a self energy term accounting for the coupling between the system of interest and the external leads. The retarded Green's function in energy-time representation is then defined as [179]

$$\mathcal{G}(t,E) = \frac{1}{i\hbar}\int d\tau e^{iE\tau/\hbar}\mathcal{G}(t,t-\tau), \tag{5.9}$$

where $\mathcal{G}(t,t')$ satisfies

$$\left(i\hbar\frac{\partial}{\partial t} - H_{\rm sys}(t) + i\Sigma\right)\mathcal{G}(t,t') = \delta(t-t'). \tag{5.10}$$

The Green's function can be defined in terms of the evolution operator as

$$\mathcal{G}(t,t') = \frac{1}{i\hbar}\Theta(t-t')U(t,t'), \tag{5.11}$$

where $\Theta(t-t')$ is the Heaviside step function. The evolution operator can be expanded in terms of the Floquet-state solutions $\Psi_\alpha(t)$ of the Schrödinger equation, similar to those defined in Eq. 3.23. The difference in the case that the effective Hamiltonian is non-Hermitian, is that the eigenspectrum of the Floquet operator $F$ is no longer real:

$$F\left|\psi_\alpha(0)\right\rangle = \lambda_\alpha\left|\psi_\alpha(0)\right\rangle, \qquad \left\langle\tilde{\psi}_\alpha(0)\right| F = \lambda_\alpha\left\langle\tilde{\psi}_\alpha(0)\right|, \tag{5.12}$$

with $\lambda_\alpha = \exp\left[-i(\frac{\epsilon_\alpha}{\hbar} - i\gamma_\alpha)T\right]$. Here, $\epsilon_\alpha$ defines the quasienergy spectrum, whereas the coefficient $\gamma_\alpha$ denotes the inverse lifetime of the corresponding eigenstate. From this starting point, one can determine the left and right periodic Floquet states via the

application of the evolution operator

$$|\Psi_\alpha(t)\rangle = e^{i(\epsilon_\alpha/\hbar - i\gamma_\alpha)t} U(t,0)\,|\psi_\alpha\rangle\,, \quad \left\langle \tilde{\Psi}_\alpha(t)\right| = e^{-i(\epsilon_\alpha/\hbar - i\gamma_\alpha)t} \left\langle \tilde{\psi}_\alpha\right| U(0,t). \tag{5.13}$$

From these definitions the evolution operator can be expanded in terms of the Floquet states as

$$U(t,t') = \sum_\alpha e^{i(\epsilon_\alpha/\hbar - i\gamma_\alpha)(t-t')}\,|\Psi_\alpha(t)\rangle \left\langle \tilde{\Psi}_\alpha(t')\right|. \tag{5.14}$$

Using the definition in Eq. 5.11, we can express the so called *Floquet-Green functions* as [179]

$$\mathcal{G}^p(E) = \frac{1}{T}\int_0^T dt e^{ip\omega t}\mathcal{G}(t,E) = \sum_{r,\alpha} \frac{\left|\Psi_\alpha^{(p+r)}\right\rangle \left\langle \tilde{\Psi}_\alpha^{(r)}\right|}{E - [\epsilon_\alpha + r\omega - i\gamma_\alpha]}, \tag{5.15}$$

where the Floquet state harmonics $\left|\Psi_\alpha^{(p)}\right\rangle$, are defined via the Fourier transform

$$\left|\Psi_\alpha^{(p)}\right\rangle = \frac{1}{T}\int_0^T dt e^{ip\omega t}\,|\Psi_\alpha(t)\rangle\,, \quad \left\langle \tilde{\Psi}_\alpha^{(p)}\right| = \frac{1}{T}\int_0^T dt e^{-ip\omega t}\left\langle \tilde{\Psi}_\alpha(t)\right|. \tag{5.16}$$

From this expression the elements of the Floquet scattering matrix required to find the conductance across the scattering sample can be accessed via the relation [134, 180]

$$S_{\alpha\beta}(E_m, E_n) = \delta_{\alpha,\beta}\delta_{m-n,0} - i\sqrt{\Gamma_\alpha\Gamma_\beta}\mathcal{G}^{m-n}_{j_\alpha j_\beta}(E_n). \tag{5.17}$$

It has been demonstrated that the presence of Majorana zero/$\pi$ modes in driven systems results in specific features in the zero temperature conductance profile, similar to the case of static systems given in Eq. 3.42. In contrast to the static case, the resonance quantisation for a periodically driven system takes the form of a sum-rule [46]

$$\sum_m G_L(\epsilon_{0/\pi} + m\omega) = \frac{2e^2}{h}, \tag{5.18}$$

where $\epsilon_0 = 0$ and $\epsilon_\pi = \frac{\pi}{T} = \omega/2$.

### 5.3.2 Stroboscopic couplings

Contrary to their static counterparts, there is no direct relationship between the Floquet scattering matrix and the topological indices of driven systems. Despite this it has been demonstrated that the topological indices can be formulated in terms of a *gedanken* scattering configuration, consisting of instantaneously emitting and absorbing particles when the coupling to the leads is switched on at discrete times separated by the driving period $T$. Between two such coupling times $t$ and $t + T$, the system evolves under the influence of the Hermitian Hamiltonian $H_{\text{sys}}(t)$, which defines a unitary Floquet operator $F_t$. It can be shown [53, 181], that this configuration corresponds to a stroboscopic scattering matrix of the form

$$S_t^{\text{strob}}(E) = \sqrt{\mathcal{I} - WW^\dagger} - W\frac{1}{\mathcal{I} - e^{iET}F_t\sqrt{\mathcal{I} - W^\dagger W}}e^{iET}F_tW^\dagger, \tag{5.19}$$

where the matrix $W$ encodes the coupling to the leads and, using the notation from Eq. 5.3, takes the form: $W = \sum_\delta \sqrt{T\Gamma_\delta}K_\delta$.

This stroboscopic scattering describes the situation in which the scattering sample can only exchange particles with the leads at the beginning and end of each period, starting at some offset time $t$ with respect to the driving period. The relevant Floquet operator is defined as

$$F_t = U(t, 0)FU^\dagger(t, 0), \tag{5.20}$$

where $F = U(T, 0)$ is the evolution operator for one period starting at the beginning of the driving cycle. Although the quasienergy spectrum is of course independent of this offset time $t$, the stroboscopic scattering matrix can in principle be $t$ dependent, depending on specifics of the evolution between the coupling times $t$ and $t + T$.

Analogous to the case of the single energy static scattering matrix (Eq. 3.11), the stroboscopic scattering matrix can be used to define a corresponding conductance averaged over the offset time $t$, $I_\alpha^{\text{strob}} = \frac{1}{T}\int_0^T dt I_{t,\alpha}^{\text{strob}}$, where

$$I_{t,\alpha}^{\text{strob}} = \frac{e}{h}\int_{-\infty}^{\infty} dE \sum_\beta \left[ \left|S_{t,\alpha\beta}^{\text{strob}}(E)\right|^2 f_\beta(E) - \left|S_{t,\beta\alpha}^{\text{strob}}(E)\right|^2 f_\alpha(E) \right]. \tag{5.21}$$

Once again, we can define the contributions to the stroboscopic conductance from each element of the scattering matrix at zero temperature as

$$G_{\alpha\beta}^{\text{strob}}(V) = \frac{e^2}{h}\frac{1}{T}\int_0^T dt \left|S_{t,\alpha\beta}^{\text{strob}}(V)\right|^2, \tag{5.22}$$

so that the total conductance reads

$$G_L^{\text{strob}}(V) = G_{L^eL^h}^{\text{strob}}(-V) + G_{L^eR^e}^{\text{strob}}(-V) - G_{L^eR^h}^{\text{strob}}(V) + \sum_{\beta\neq\alpha} G_{\beta L^e}^{\text{strob}}(V). \tag{5.23}$$

The profile of this stroboscopic conductance behaves much in the same way as its static counterpart defined in Eq. 3.42. In particular, it exhibits quantized conductance peaks corresponding to the existence of topologically protected Majorana edge modes. Although both result in quantized conductance peaks in some form, the exact relationship between the stroboscopic and continuously coupled conductances remains to be explored.

We see that (Eq. 5.19), in contrast to the physical conductance associated with a system that is constantly coupled to the external leads, the stroboscopic scattering matrix, and consequently the corresponding conductance, are periodic in energy. This helps to explain why the quantisation rule in Eq. 5.18 required the sum over energies separated by integer multiples of the driving frequency. Further light is shed upon the relationship between the two quantities by considering the intermediate scenario for which the system is continuously coupled to the external leads, but scattered particles are only recorded at discrete intervals separated by the driving period and starting at the delay time $t$. We associate with this process an alternative stroboscopic scattering matrix $\tilde{S}_t(E)$ which is a non-unitary construction due the neglected scattered states flowing in the leads during the intervals between the discrete recording times. This setup allows us to draw a direct analytical connection between $\tilde{S}_t(E)$ and the Floquet scattering matrix (see Appendix A):

$$\tilde{S}_t(E) = \sum_{k,n} S(E_n, E_{n+k}) e^{ik\omega t}. \tag{5.24}$$

This relationship to the Floquet scattering matrix highlights the need to sum scattering events over all Floquet sideband energies, $E_n = E + n\omega$, in order to make a meaningful comparison with the stroboscopic conductance. We therefore define a summed conductance

$$\tilde{G}_\alpha(V) = \sum_n G_\alpha(V + n\omega), \tag{5.25}$$

which provides a natural quantity to be compared with that defined in Eq. 5.23.

### 5.3.3 Weak coupling limit

In order to compare the conductance quantities $\tilde{G}_\alpha(V)$ and $G_\alpha^{\text{strob}}(V)$, one can make use of the fact that they both exhibit quantized conductance peaks at $V = \epsilon_{0/\pi}$. Therefore, analysing their behaviour in the vicinity of these resonances can help to shed light on the relationship between the quantities around the resonant quasienergies. Furthermore, in the regime for which the coupling strength to the external leads can be considered small compared with the other energy scales associated with the system Hamiltonian, these resonances dominate the conductance spectra and hence we may expect the agreement between the two to extend, to some extent, beyond the resonant Majorana quasienergies.

In the weak coupling limit, the self energy term $\Sigma$ from Eq. 5.10 can be treated as a perturbation to the system Hamiltonian $H_{\text{sys}}(t)$. In particular, the Floquet state solutions can be approximated as solutions to the Floquet equation for an isolated system:

$$\left(H_{\text{sys}}(t) - i\frac{d}{dt}\right)|\phi_\alpha(t)\rangle = \epsilon_\alpha\,|\phi_\alpha(t)\rangle\,. \tag{5.26}$$

The first order corrections to the quasienergies $\epsilon_\alpha$ are found to be

$$\tilde{\gamma}_\alpha = \frac{1}{T}\int_0^T dt\,\langle\phi_\alpha(t)|\Sigma|\phi_\alpha(t)\rangle\,. \tag{5.27}$$

Using the expression for the Floquet scattering matrix in terms of the Floquet-Green functions in Eq. 5.17, the contributions to the current from each scattering matrix

element (Eq. 5.6) can be approximated by

$$|S_{\alpha\beta}(E_n,E)|^2 = \Gamma_\alpha\Gamma_\beta \sum_{ijrr'} \frac{\langle\alpha| K_\alpha \left|\phi_i^{(n+r)}\right\rangle \left\langle\phi_i^{(r)}\right| K_\beta^\dagger |\beta\rangle \langle\beta| K_\beta \left|\phi_j^{(n+r')}\right\rangle \left\langle\phi_j^{(r')}\right| K_\alpha^\dagger |\alpha\rangle}{\left[E-(\epsilon_i+r\omega-i\tilde{\gamma}_i)\right]\left[E-(\epsilon_j+r'\omega+i\tilde{\gamma}_j)\right]}. \tag{5.28}$$

Here $\langle\phi_j| K_\alpha |\alpha\rangle$ gives the tunneling amplitude for scattering into the mode $\alpha$, running over both particle and hole degrees of freedom, via the mode $\phi_j$ of the internal system.

Since the coupling strength $\Gamma_\alpha$ controls the width of conductance resonances, the weak coupling regime corresponds to a conductance spectra consisting of sharp Lorentzian peaks at energies $\epsilon_i + r\omega$ and $\epsilon_j + r'\omega$. As a result, the sums in the previous expression are dominated by contributions for which these energies coincide or for which the quasienergies $\epsilon_i$ are degenerate. Thus, the scattering matrix can be further simplified as

$$|S_{\alpha\beta}(E_n,E)|^2 \approx \Gamma_\alpha\Gamma_\beta \sum_{irk} \frac{\left|\sum_k \langle\alpha| K_\alpha \left|\phi_{i_k}^{(n+r)}\right\rangle \left\langle\phi_{i_k}^{(r)}\right| K_\beta^\dagger |\beta\rangle\right|^2}{\tilde{\gamma}_i^2 + (E-\epsilon_i+r\omega)^2}, \tag{5.29}$$

where $|\phi_{i_k}\rangle$ represent the eigenstates corresponding to the degenerate eigenvalue $\epsilon_i$. The degenerate states correspond to the Majorana bound states localized at each end of the chain. Since these states only couple to one of the external leads, only one will contribute to the scattering matrix elements and we henceforward drop the sum over degenerate states $k$.

The scattering matrix elements in this weak coupling regime can be used to produce approximations of the matching contribution to the summed conductance at zero

temperature:

$$\begin{aligned}\tilde{G}_{\alpha\beta}(V) &= \frac{e^2}{h}\Gamma_\alpha\Gamma_\beta \sum_{irnm} \frac{\left|\langle\alpha| K_\alpha \left|\phi_i^{(n)}\right\rangle \left\langle\phi_i^{(r)}\right| K_\beta^\dagger |\beta\rangle\right|^2}{\tilde{\gamma}_i^2 + (V - \epsilon_i + m\omega)^2}, \\ &= \frac{e^2}{h}\frac{\Gamma_\alpha\Gamma_\beta}{T^2} \sum_{im} \int_0^T dtdt' \frac{\left|\langle\alpha| K_\alpha |\phi_i(t)\rangle \langle\phi_i(t')| K_\beta^\dagger |\beta\rangle\right|^2}{\tilde{\gamma}_i^2 + (V - \epsilon_i + m\omega)^2}.\end{aligned} \tag{5.30}$$

Close to the resonant quasi-energies, $V \approx \epsilon_i/e$, the conductance contributions take the form of a Lorentzian distribution:

$$\tilde{G}_{\alpha\beta}(V) \approx \frac{e^2}{h}\frac{\tilde{\gamma}_i^{(\alpha)}\tilde{\gamma}_i^{(\beta)}}{\tilde{\gamma}_i^2}\mathcal{L}\Big(\frac{eV - \epsilon_i}{\tilde{\gamma}_i}\Big), \tag{5.31}$$

where $\mathcal{L}(x) = (1 + x^2)^{-1}$ is the Lorentzian function and

$$\tilde{\gamma}_i^{(\alpha)} = \frac{1}{T}\int_0^T \Gamma_\alpha |\langle\alpha| K_\alpha |\phi_i(t)\rangle|^2, \quad \text{so that} \quad \tilde{\gamma}_i = \sum_\delta \tilde{\gamma}_i^{(\delta)}. \tag{5.32}$$

Using the fact that the localization of the Majorana states dictates that they only contribute to the conductance through Andreev reflection events, along with the particle-hole symmetry constraint $\tilde{\gamma}_{0,\pi}^{(L^e)} = \tilde{\gamma}_{0,\pi}^{(L^h)}$ one sees that for $V \approx \epsilon_{0/\pi}/e$,

$$\tilde{G}(V) = 2\tilde{G}_{L^eL^h}(V) \approx \frac{2e^2}{h}\mathcal{L}\Big(\frac{eV - \epsilon_{0/\pi}}{\tilde{\gamma}_{0/\pi}}\Big). \tag{5.33}$$

We next turn our attention to deriving a similar expression for the stroboscopic conductance close to the resonances. In order to facilitate the comparison of the two quantities, it is necessary to express the stroboscopic conductance in terms of the unperturbed Floquet state solutions of the Hamiltonian $H_{\text{sys}}(t)$. Consequently, we

would like to perform a perturbative expansion, in the coupling strength $\Gamma_\alpha$, of the operator appearing as a fraction in Eq. 5.19. As a first step towards this goal we can write this operator as a geometric series,

$$\frac{1}{\mathcal{I} - e^{iET}F_t\sqrt{\mathcal{I}-W^\dagger W}} = \sum_k \left(e^{iET}F_t\sqrt{\mathcal{I}-W^\dagger W}\right)^k \approx \sum_k \left(e^{iET}(\underbrace{F_t}_{A_0} - \underbrace{\frac{1}{2}F_tW^\dagger W}_{\Gamma A_1})\right)^k. \tag{5.34}$$

Here we have defined the perturbed operator $A = A_0 + \Gamma A_1$. Expanding $A$ in terms of its eigenstates and eigenvalues, given by $A\left|x_i\right\rangle = x_i\left|x_i\right\rangle$, we can rewrite this expression as

$$\frac{1}{\mathcal{I} - e^{iET}F_t\sqrt{\mathcal{I}-W^\dagger W}} = \sum_k \left(e^{iET}\sum_i x_i\left|x_i\right\rangle\left\langle x_i\right|\right)^k = \sum_i \frac{1}{1-e^{iET}x_i}\left|x_i\right\rangle\left\langle x_i\right|. \tag{5.35}$$

The unperturbed Floquet operator $F_t = A_0$ can be expanded in terms of the Floquet state solutions of the uncoupled Schrödinger equation introduced in Eq. 5.26 as

$$F_t = \sum_i e^{-i\epsilon_i T}\left|\phi_i(t)\right\rangle\left\langle\phi_i(t)\right|. \tag{5.36}$$

The unperturbed eigenstates $\left|\phi_i(t)\right\rangle$ therefore form the zeroth order term in the expansion of the eigenstates of $A$, which will be sufficient for our requirements in the weak coupling regime. However, we will include the corrections to the eigenvalues $x_i(t)$ up to first order in $\Gamma$, so that

$$x_i(t) = e^{-i\epsilon_i T} + \frac{1}{2}\frac{\left\langle\phi_i(t)\right| F_tW^\dagger W\left|\phi_i(t)\right\rangle}{\left\langle\phi_i(t)|\phi_i(t)\right\rangle} = e^{-i\epsilon_i T}\Big(1 + T\underbrace{\left\langle\phi_i(t)\right|\Sigma\left|\phi_i(t)\right\rangle}_{\gamma_i(t)}\Big). \tag{5.37}$$

Using this expansion, the stroboscopic scattering matrix now takes the form

$$S_t^{\text{strob}}(E) = \sqrt{\mathcal{I} - W^\dagger W} - W \sum_i \frac{e^{i(E-\epsilon_i)T}}{1 - e^{iET} x_i(t)} \left|\phi_i(t)\right\rangle \left\langle\phi_i(t)\right| W^\dagger. \tag{5.38}$$

In this form it is possible to make meaningful comparisons between the conductance of the two coupling configurations. Again using the fact that, in the limit of weak coupling, the conductance profile is dominated by sharp Lorentzian peaks at the resonant quasienergies $\epsilon_i$, the expression for $S_t^{\text{strob}}(E)$ translates into the following contributions to the stroboscopic conductance defined in Eq. 5.23:

$$G_{\alpha\beta}^{\text{strob}}(V) = \frac{e^2}{h} T \Gamma_\alpha \Gamma_\beta \int_0^T dt \sum_i \frac{\left|\left\langle\alpha\right| K_\alpha \left|\phi_i(t)\right\rangle \left\langle\phi_i(t)\right| K_\beta^\dagger \left|\beta\right\rangle\right|^2}{\left|1 - e^{i(V-\epsilon_i)T}(1 + T\gamma_i(t))\right|^2}. \tag{5.39}$$

At this point we can return to our expression for the conductance summed over Floquet sidebands for constant couplings, defined in Eq. 5.30. This expression can be rearranged to a similar form as our stroboscopic conductance using the relation

$$\sum_p \frac{e^{ip\omega z}}{A - p\omega} = \frac{Tie^{iAz}}{e^{iAT} - 1}, \tag{5.40}$$

so that

$$\tilde{G}_{\alpha\beta}(V) = \frac{e^2}{h} \Gamma_\alpha \Gamma_\beta \sum_i \int_0^T dt dt' \frac{\left|\left\langle\alpha\right| K_\alpha \left|\phi_i(t)\right\rangle \left\langle\phi_i(t')\right| K_\beta \left|\beta\right\rangle\right|^2}{\left|1 - e^{i(V-\epsilon_i)T}(1 + T\tilde{\gamma}_i)\right|^2}. \tag{5.41}$$

It is clear that, from Eqs. 5.39 and 5.41, there exist clear similarities between the conductances for continuous and pulsed coupling in the regimes for which this coupling can be considered weak. Both expressions are clearly dominated by resonances at the quasienergies, however the parameters controlling the widths of those peaks are generically different in each case.

In order to highlight the exact nature of this difference, we can, as we did for the case of continuously coupled leads, examine the behaviour of the stroboscopic conductance (Eq. 5.39) at voltage biases close to resonant quasienergies, $V \approx \epsilon_i/e$. In doing so, one finds that the contributions to the conductance from each element of the scattering matrix can be further simplified as

$$\begin{aligned} G^{\text{strob}}_{\alpha\beta}(V) &= \frac{e^2}{h}\frac{1}{T}\int_0^T \frac{\left|\langle\alpha|\, K_\alpha\, |\phi_i(t)\rangle\, \langle\phi_i(t)|\, K^\dagger_\beta\, |\beta\rangle\right|^2}{\gamma_i^2(t)}\mathcal{L}\Big(\frac{eV-\epsilon_i}{\gamma_i(t)}\Big) \\ &= \frac{e^2}{h}\frac{1}{T}\int_0^T \frac{\gamma_i^{(\alpha)}(t)\gamma_i^{(\beta)}(t)}{\gamma_i^2(t)}\mathcal{L}\Big(\frac{eV-\epsilon_i}{\gamma_i(t)}\Big), \end{aligned} \tag{5.42}$$

where

$$\gamma_i^{(\delta)}(t) = \Gamma_\delta |\langle\delta|\, K_\delta\, |\phi_i(t)\rangle|^2, \text{ so that } \gamma_i(t) = \sum_\delta \gamma_i^{(\delta)}(t). \tag{5.43}$$

Once again, the particle-hole symmetry of the superconducting system, along with the localization of the Majorana modes, results in quantized conductance peaks at the corresponding voltage biases $V \approx \epsilon_i/e$ of the form

$$G^{\text{strob}}(V) = \frac{2e^2}{h}\frac{1}{T}\int_0^T dt\mathcal{L}\Big(\frac{eV-\epsilon_{0/\pi}}{\gamma_{0/\pi}(t)}\Big). \tag{5.44}$$

### 5.3.4 Comparison of conductance quantities

The expressions for the conductance due to the Majorana bound states for each of the coupling configurations, Eq. 5.33 and 5.44, constitute the key results from this chapter. Their comparison demonstrates that the discrepancy between the two quantities arises due to the time dependence of the function $\gamma_i(t)$, defined in Eq. 5.37, which controls the widths of the peaks in the conductance profiles. Agreement between the two quantities

therefore occurs when this function is time independent. The time dependence of $\gamma_i(t)$ is captured by the variance function

$$V_\alpha = \Big\langle \big(\gamma_\alpha(t) - \langle\gamma_\alpha(t)\rangle\big)^2 \Big\rangle. \tag{5.45}$$

This function acts as a figure of merit quantifying the discrepancy between the two coupling configurations at the resonances. As a more concrete measure of this variation we can also consider the difference between the two functions integrated around a particular resonant quasienergy $\epsilon_i$:

$$D_i = \frac{1}{\Gamma}\int_{\epsilon_i-\Gamma}^{\epsilon_i+\Gamma} dE \left[\mathcal{L}\Big(\frac{E-\epsilon_i}{\tilde{\gamma}_i}\Big) - \frac{1}{T}\int_0^T dt \mathcal{L}\Big(\frac{E-\epsilon_i}{\gamma_i(t)}\Big)\right]. \tag{5.46}$$

We note that this difference integrated over the entire voltage range vanishes identically:

$$\begin{aligned} D_i^\infty &= \int_{-\infty}^{\infty} dE \left[\mathcal{L}\Big(\frac{E-\epsilon_i}{\tilde{\gamma}_i}\Big) - \frac{1}{T}\int_0^T dt \mathcal{L}\Big(\frac{E-\epsilon_i}{\gamma_i(t)}\Big)\right] \\ &= \pi\tilde{\gamma}_i - \frac{\pi}{T}\int_0^T \gamma_i(t)dt = \pi\tilde{\gamma}_i - \pi\tilde{\gamma}_i = 0, \end{aligned} \tag{5.47}$$

where we have used the definition of $\tilde{\gamma}$ from Eq. 5.27. Consequently, in the weak coupling limit, we see that the total weight of the conductance peaks associated with Majorana modes are identical for the stroboscopic and constant coupling configurations.

In order to explore the difference between the conductance quantities $\tilde{G}$ and $G^{\text{strob}}$ for arbitrary values of the voltage bias, we will apply the analysis outlined in this section to the example of a periodically driven Kitaev chain subject to two different driving protocols.

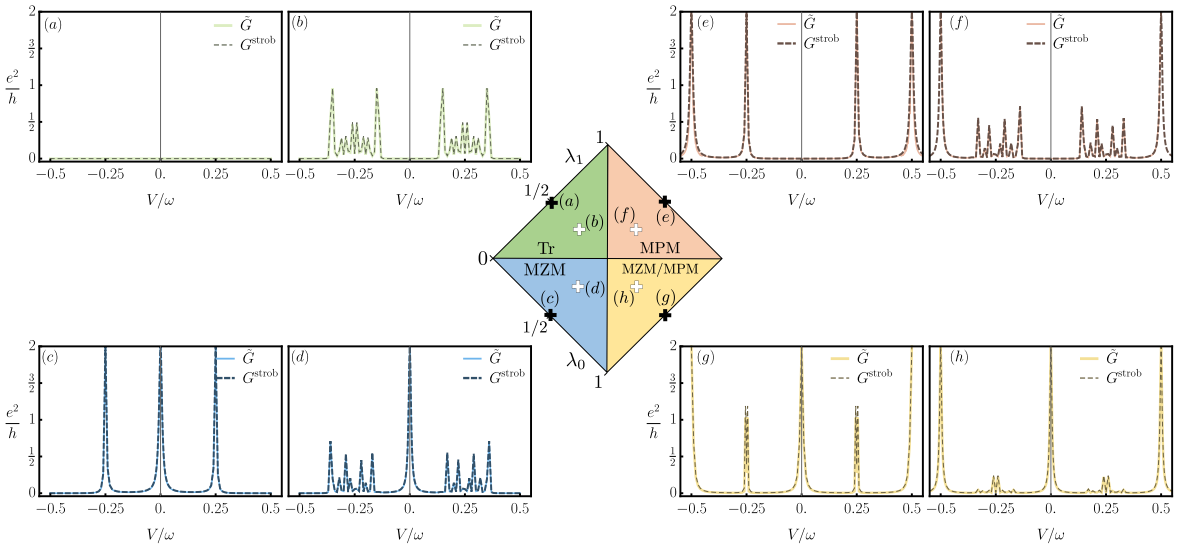


Figure 5.3: Phase space diagram illustrating how the topological phase of the Floquet Kitaev wire depends upon the Hamiltonian parameters $\lambda_0$ and $\lambda_1$ (see Eq. 5.50). (a-h) Numerical results for the zero temperature differential conductance summed over energy sidebands $\tilde{G}$ and the stroboscopic conductance $G^{\text{strob}}$, plotted as a function of the total voltage bias between the left and right external leads $V = V_L - V_R$. The plot colours correspond to those in the phase diagram. The conductance is evaluated at both the four sweet spots, marked by black crosses, as well as the points marked by the white crosses in each phase: (a,b) Trivial, (c,d) MZM, (e,f) MPM, (g,h) MZM/MPM. The results were obtained using a chain of 20 sites and with tunneling rates to the external leads given by $\Gamma_{L/R}/\omega = 0.016$.

## 5.4 Transport signatures of a periodically driven Kitaev chain

In this section we will explore the relationship between the conductance measured in transport experiments and the topological invariants defined via the stroboscopic scattering matrix by considering the example of a periodically driven Kitaev chain. For

this, we use the same toy model Hamiltonian introduced in Sec. 2.2:

$$H(w,\Delta,\mu) = -\sum_i \mu(t) a_i^\dagger a_i + \sum_i \Big( -\frac{J(t)}{2} a_i^\dagger a_{i+1} + \frac{\Delta(t)}{2} a_i a_{i+1} + \text{h.c.}\Big), \tag{5.48}$$

where the on-site potential $\mu$, the nearest neighbour coupling $J$ and the superconducting pairing strength $\Delta$ are all now time dependent with a period ($T$). We will consider two different step like driving protocols in which the parameters of the Hamiltonian are switched instantaneously between two different sets of values.

### 5.4.1 Protocol 1: Sudden switching between Hamiltonians in different topological phases

Firstly, we study the scenario in which the Kitaev chain is forced to alternate between the topologically non-trivial and trivial phases in each half of the cycle [163], so that the evolution is governed by a Floquet operator of the form

$$F = e^{-iH_1 T/2} e^{-iH_0 T/2}, \tag{5.49}$$

where

$$H_0 = H(2\pi\lambda_0/T, 2\pi\lambda_0/T, 0) \quad \text{and} \quad H_1 = H(0,0,2\pi\lambda_1/T). \tag{5.50}$$

Here $H_0$ is the Hamiltonian at the *sweet spot* of the static topological phase, characterised by the existence of Majorana zero modes localized on the final site of the chain, with zero correlation length.

By allowing the parameters $\lambda_0$, $\lambda_1$ to take values in the interval $\lambda_i \in [0,1]$, we see the emergence of four topologically distinct phases which are illustrated in the phase

diagram in Fig. 5.3. The phase in which the system resides is evidenced by the presence or absence of Majorana zero modes and Majorana $\pi$ modes. Due to the influence of these Majorana bound states upon the scattering properties, each phase can equally be characterised by a topological index expressed in terms of the single energy stroboscopic scattering matrix via

$$\nu_{0/\pi} = \frac{1}{i\pi} \log \det\{\mathcal{R}_L(\epsilon_{0/\pi})\}, \tag{5.51}$$

where $\mathcal{R}_L$ is the sub-block of the entire stroboscopic scattering matrix describing reflection in the lead $L$. The justification for the form of $\nu$ follows from the analogous discussion of static systems in Sec. 3.3 and via comparison with the static invariants listed in Table 3.1. To gain insight into how this quantity changes as we move across the phase diagram, it is useful to consider the stroboscopic scattering matrix at the sweet spots in each phase, which are identified by the relevant Majorana modes being localized at the left and right most sites of the Kitaev chain. We also consider the case for which the coupling to the external leads is perfectly transparent, i.e. $W = \sum_\delta \sqrt{T\Gamma_\delta} K_\delta = \sum_\delta K_\delta$. At these special points in the phase diagram, indicated by the black crosses in Fig. 5.3, there is no possibility of transmission events and the scattering matrix can be decoupled into a block sum of the reflection sub-matrices in each lead: $S(\epsilon) = \mathcal{R}_L(\epsilon) \oplus \mathcal{R}_R(\epsilon)$. Subsequent calculation of the index $\nu$ for each sweet spot yields:

(i) For the trivial phase sweet spot at $\lambda_0 = 0$ and $\lambda_1 = 1/2$ we have $\mathcal{R}_L(\epsilon) = \mathcal{R}_R(\epsilon) = -ie^{i\epsilon T}\sigma_z$, and the topological indices are:

$$\nu_{0/\pi} = 0. \tag{5.52}$$

(ii) The MZM phase, where the sweet spot is $\lambda_0 = 1/2$ and $\lambda_1 = 0$ results in $\mathcal{R}_L(\epsilon) = \frac{e^{i\epsilon T}}{2}[(1 - e^{i\epsilon T})\mathcal{I} - (1 + e^{i\epsilon T})\sigma_x]$ and $\mathcal{R}_R(\epsilon) = \frac{e^{i\epsilon T}}{2}[(1 - e^{i\epsilon T})\mathcal{I} + (1 + e^{i\epsilon T})\sigma_x]$, and the topological indices are:

$$\nu_0 = 1\,;\, \nu_\pi = 0. \tag{5.53}$$

(iii) The sweet spot of the MPM phase is at $\lambda_0 = 1/2$ and $\lambda_1 = 1$ with $\mathcal{R}_L(\epsilon) = \frac{e^{i\epsilon T}}{2}[(-1 - e^{i\epsilon T})\mathcal{I} + (1 - e^{i\epsilon T})\sigma_x]$ and $\mathcal{R}_R(\epsilon) = \frac{e^{i\epsilon T}}{2}[(-1 - e^{i\epsilon T})\mathcal{I} - (1 - e^{i\epsilon T})\sigma_x]$, and the topological indices are:

$$\nu_0 = 0\,;\, \nu_\pi = 1. \tag{5.54}$$

(iv) Finally, the sweet spot of the MPM+MZM phase at $\lambda_0 = 1$ and $\lambda_1 = 1/2$ gives $\mathcal{R}_L(\epsilon) = -\mathcal{R}_R(\epsilon) = e^{i\epsilon T}\sigma_y$ and hence

$$\nu_0 = 1\,;\, \nu_\pi = 1. \tag{5.55}$$

These results are directly reflected in the quantized values of $G^{\text{strob}}(V = \epsilon_{0/\pi})$.

In Fig. 5.3(a-h) we plot the zero temperature conductance profiles as a function of bias voltage $V$, for two points in each of the distinct phases. These points are marked by crosses on the phase diagram, with the black crosses corresponding to the four sweet spots and the white crosses marking points away from these localized limits. The chain length used in the numerics is sufficiently long for any interaction between the Majoranas at opposite ends of the wire, and any resultant splitting of the resonances, to be neglected. Each subplot includes profiles for both $\tilde{G}(V)$ (solid lines), the physical

conductance of a constantly coupled system summed over Floquet harmonics, alongside the stroboscopic conductance $G^{\text{strob}}(V)$ (dashed lines) defined via the fictitious pulsed scattering configuration. For both quantities, we see that resonant Andreev reflection via the Majorana bound states results in quantized conductance peaks of height $2e^2/h$ at $eV = 0$ and/or $eV = \pi/T$, corresponding to the existence of Majorana zero and $\pi$ modes, respectively.

As discussed in the preceding section, we expect that the conductance profiles corresponding to the different coupling configurations should differ in the widths of the resonant peaks due to the difference in the level broadening. For weak coupling, the conductance traces in Fig. 5.3 demonstrate very good agreement even away from the Majorana quasienergies $eV = 0$ and $eV = \pi/T$. In order to analyse this discrepancy in greater detail we plot the integrated difference function $D_{0/\pi}$ around the zero and $\pi$ mode resonances throughout the phase space spanned by $\lambda_0$, $\lambda_1$ in Fig. 5.4 (a) and (c) respectively. To complement this, we additionally plot $V_\alpha$, the function capturing the time variance of the resonance width $\gamma_\alpha(t)$ in Fig. 5.4(b) and (d). The correlation between the two quantities is clear and confirms that the difference between the conductances is indeed maximal at points where the offset time dependence of $\gamma_\alpha(t)$ is most pronounced. From the plots, it is evident that these points occur in the phase for which both Majorana zero and $\pi$-modes are present.

Fig. 5.4(e-h) show the stroboscopic and DC conductance traces at points in the phase diagram close to where the difference function $D_{0,\pi}$ is maximal, for bias voltages in close proximity to the resonant quasienergy in question. By focusing on this narrower range of biases the discrepancy between the quantities becomes visible and, although small, this difference persists in the limit $\Gamma \to 0$. In order to determine whether the

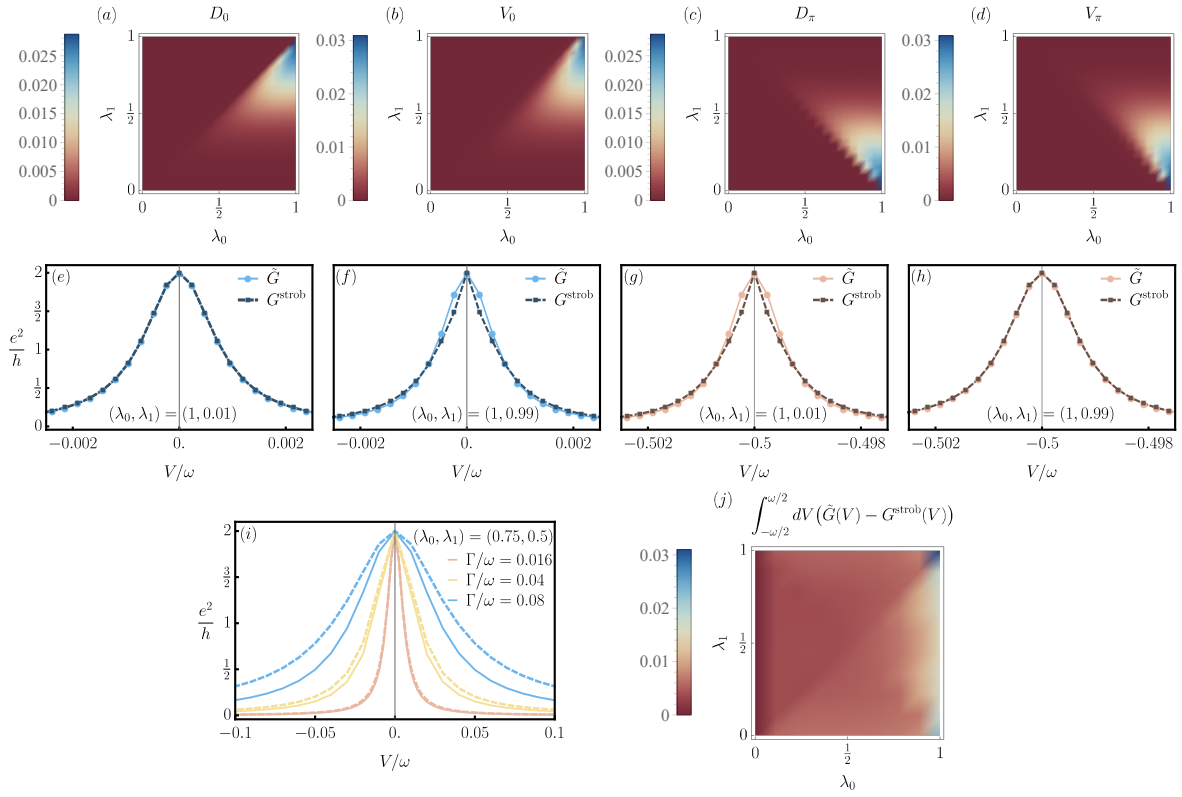


Figure 5.4: (a,c) Density plots illustrating the value of the difference function for both the zero mode resonance $D_0$ and $\pi$ mode resonance $D_\pi$ respectively throughout the parameter space $(\lambda_0, \lambda_1)$, with coupling strength $\Gamma_{L/R}/\omega = 0.0016$. (b,d) Corresponding plots of the time variance of the function $\gamma_\alpha(t)$ controlling the resonance widths. The comparison between the conductance summed over energy sidebands $\tilde{G}$ and the stroboscopic conductance $G^{\mathrm{strob}}$ for selected points are shown in (e-h), again with coupling strength $\Gamma_{L/R}/\omega = 0.0016$. (i) Comparison of $\tilde{G}$ (solid lines) and $G^{\mathrm{strob}}$ (dashed lines) for increased strength coupling to the external leads $\Gamma$, close to the MZM resonance. (j) Density plot illustrating difference between the stroboscopic and summed conductances integrated over the entire spectrum throughout the parameter space, calculated using a coupling strength of $\Gamma_{L/R}/\omega = 0.016$. All data was obtained using a chain of $n = 20$ fermionic sites.

discrepancy at the Majorana state resonances is indicative of the difference between the conductance quantities at all bias voltages, in panel (j) we plot the exact difference integrated over the entire Floquet energy range from $-\omega/2$ to $\omega/2$. From this plot we can conclude that the figures of merit $D_0$ and $D_\pi$ do a good job of quantitatively capturing the parameters for which this difference is greatest. Finally, we see from panel (i) that, upon increasing the coupling strength to the external leads, the agreement between the conductance quantities at the resonances breaks down and the difference between them becomes increasingly stark.

### 5.4.2 Protocol 2: Sudden switching between Hamiltonians within the trivial topological phase

As a second example, we consider an alternative driving of the Kitaev wire that comprises of alternating between two topologically trivial Hamiltonians in each half of the cycle [46], which differ by the value of the chemical potential $\mu_i(t)$:

$$H_0 = H(J, \Delta, \mu_0) \quad \text{and} \quad H_1 = H(J, \Delta, \mu_1), \tag{5.56}$$

such that $\mu_{0,1} > J/2$. In this case, distinct topological phases can be accessed by varying the driving frequency $\omega$, resulting in a phase diagram of the form illustrated in Fig 5.5 (a). We see that this driving protocol results in the existence of the same four phases as in the previous example, despite the fact that at any instant throughout the driving the Kitaev chain is in its trivial state.

As for the previous protocol, in Figs. 5.5(d-f) we plot the conductance quantities for the two coupling configurations, $\tilde{G}(V)$ and $G^{\text{strob}}(V)$, and again find that they show

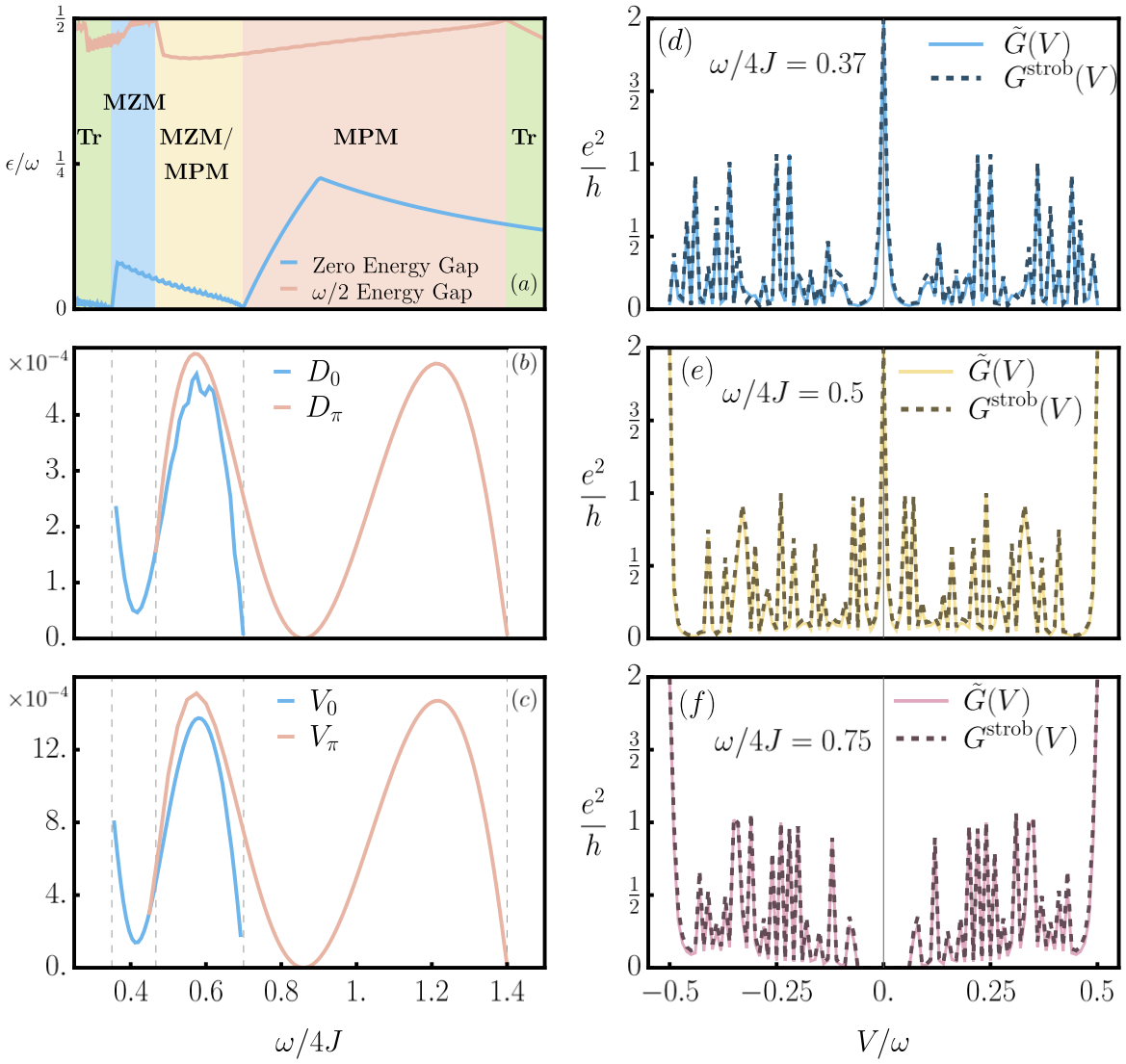


Figure 5.5: (a) Variation of the bulk quasi energy gaps around $\epsilon T = 0$ and $\epsilon T = \pi$ over a range of driving frequencies $\omega$. The possible phases over this range are denoted: Tr=Trivial, MZM=Zero-modes only, MPM=$\pi$-modes only and MZM/MPM=Both Zero and $\pi$ modes. (b) Illustration of the difference functions for the zero ($D_0$) and $\pi$ ($D_\pi$) mode resonances over this range of frequencies and (c) the corresponding behaviour of the time variance of $\gamma_i(t)$ dictating this difference. (d-f) Conductance profiles for selected driving frequencies comparing the measured conductance summed over sidebands with the stroboscopic construction. All data was obtained using a chain length of $n = 70$ and coupling strength $\Gamma_{L/R}/\omega = 0.04$.

good agreement across all values of the bias voltage. Furthermore, the concurrence between the plots in panels (b) and (c) illustrates that the difference between the conductances at the zero and $\pi$ Majorana peaks is well captured by the time variance of the function $\gamma_\alpha(t)$, at all relevant driving frequencies.

While both of the protocols studied are similar in the sense that the discrepancy between the conductances is small across all voltage biases and is captured by the difference between the widths of the resonances, there remain aspects of the connection between the conductances that are protocol-dependent. We notice that the maximum difference in the first protocol is roughly two orders of magnitude larger than in the second. This is down to the time dependence of $\gamma_\alpha(t)$, which is controlled by how the eigenstates of the Floquet operator behave as a function of the offset time between the pulsed stroboscopic coupling and the start of the driving cycle. Specifically, it depends on the time dependence of the contribution to the eigenstates on the left and right-most fermionic sites which are coupled to the external leads. In the example of the first protocol, at the points at which the difference is largest, the relevant eigenstate is localized entirely upon the first site, $n = 1$ at $t = 0$, but as the offset time increases this localization is shifted almost entirely to the site $n = 2$ and then back to the first at $t = 0.5T$ (See Fig. 5.6(a)). This results in a significant time dependence of $\gamma_\alpha(t)$ and consequently a difference between the conductance quantities. This is in contrast to the second protocol (Fig. 5.6(c,d)), for which the eigenstates are more evenly distributed throughout the entire chain irrespective of the offset time $t$. Accordingly, the contribution on the end-most coupled sites depends little on the variation of $t$.

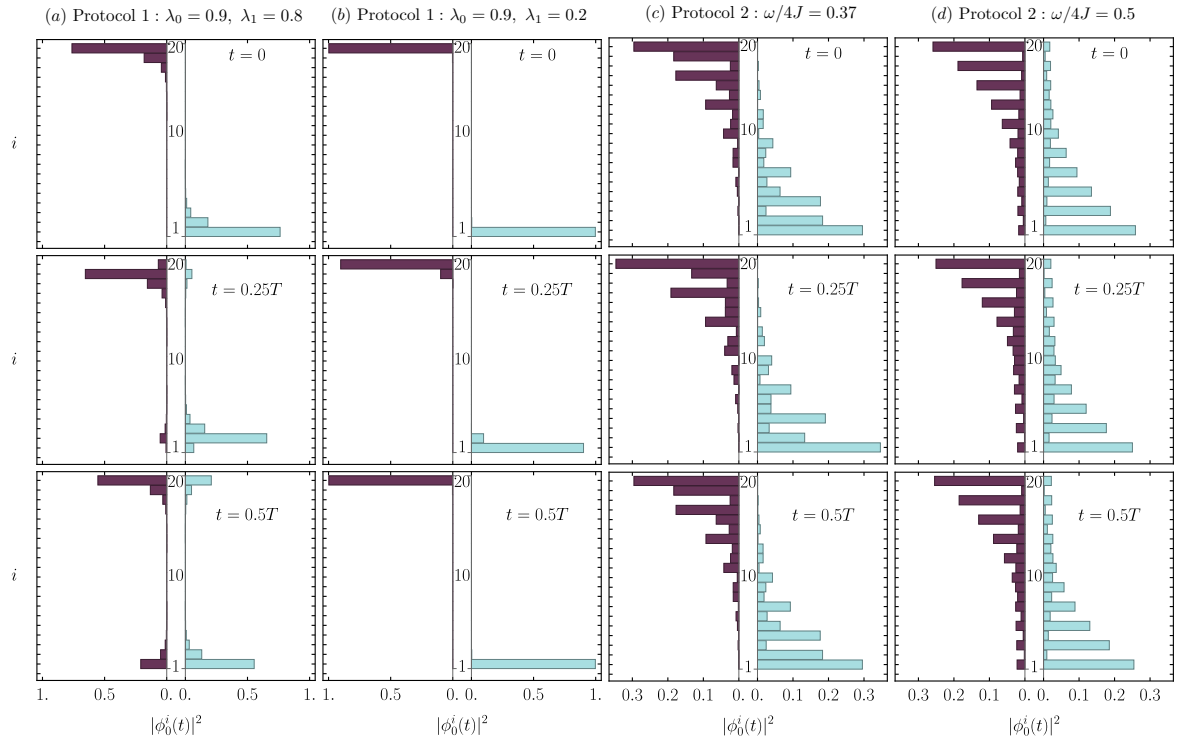


Figure 5.6: Weight of the time-dependent zero-mode Floquet states for an isolated system $|\phi_0(t)\rangle$ (Eq. 5.26) on each of the fermionic sites in a 1D driven Kitaev wire. (a) and (b) show solutions from two chosen points from the phase diagram for protocol 1 (see Fig. 5.3), whereas (c) and (d) show points from protocol 2 (see Fig. 5.5(a)). For each example, the spatial structure of the zero mode is shown for 3 snapshots throughout the driving period, illustrating the extent of the time dependence. In (a) the strong time dependence of the weight upon the end sites corresponds to the marked difference in the stroboscopic and summed conductance quantities at this point in the phase space. This is contrasted with (b), a point at which the time dependence is minimal and hence the agreement is good. The examples from protocol 2 show little dependence on time, corresponding to good agreement between the two conductances.

## 5.5 Discussion

Within this chapter, we have explored the connection between the experimentally accessible Floquet scattering matrix and a related scattering matrix formulated in terms of a gedanken stroboscopic coupling experiment, from which topological invariants of periodically driven systems can be formulated. The comparison between these two quantities provides a platform from which to explore signatures of Floquet topological phases in transport properties, such as differential conductance, building upon the relationships between scattering matrix invariants and topological phase classification already established for non-driven systems.

We have contrasted the electronic transport properties of periodically driven systems subjected to constant and periodically pulsed coupling to external leads, via the analysis of both the DC conductance summed over Floquet side-bands and the period-averaged stroboscopic conductance. In this way, we have demonstrated that the two quantities are equivalent at the resonant quasienergies associated with the Majorana bound states and hence see how the stroboscopically defined topological invariant results in quantized conductance peaks of height $2e^2/h$, in the sideband summed DC conductance. However, at arbitrary values of the voltage bias there exists no analytic connection between the two quantities and the general difference between them is captured by the resonance widths in the limit of small coupling to the external leads.

We have explored this relationship for the specific example of a driven Kitaev chain subjected to two different driving protocols, both consisting of instantaneous alterations of the Hamiltonian parameters half way through the cycle. Both protocols demonstrate the emergence of four distinct topological phases, distinguished by the presence or absence of Majorana zero and/or $\pi$-modes and characterized by topological invariants

derived from the stroboscopic scattering matrix. We have seen that, within the weak coupling regime, the stroboscopic conductance shows good agreement with the DC conductance summed over sidebands at all bias voltages. Furthermore, in this limit, the total weights of the Majorana quasienergy conductance peaks integrated over all bias voltages exactly agree for both quantities. However, we have further studied the dependence of the difference on the physical parameter space and the driving protocol in question, finding that generically the discrepancy is larger when the Majorana mode weight at the end of the chain depends strongly on the offset time between the driving cycle and the pulsed coupling period. Hence, for generic systems, the stroboscopic scattering matrix can only be guaranteed to predict the height and total weight of the conductance peaks associated with the presence of Majorana bound modes.

By exploring the factors which contribute to the discrepancy between the two conductance quantities being small, we can determine the regimes in which the stroboscopically defined single energy scattering matrix, containing the relevant topological invariant for the driven system, can provide a good approximation of experimentally accessible DC conductance profile.

# Chapter 6

# Transport Statistics of a Majorana Braiding Protocol

This chapter is based upon the results published in the paper:
T. Simons, D. Meidan, and A. Romito. *Pumped heat and charge statistics from Majorana braiding* Phys. Rev. B **102**, 245420 (2020)

In addition to stimulating the emergence of additional topological phases, not present in static systems, periodic modulation can also influence the transport properties of mesoscopic systems when the driving can be considered slow compared with the scattering time. When coupled to multiple particle reservoirs, the slow driving of a pair of Hamiltonian parameters is known to stimulate a pumping effect that can drive a current between different reservoirs in the absence of potential and temperature biases [6, 54, 182]. Interestingly, this contribution to the current emits a geometrical formulation, in that it depends only upon the contour traversed in the parameter space, and can be interpreted as an analogue of the Berry phase [75] accumulated when a

wavefunction is subjected to some periodic modulation [183]. However, the geometric phase of interest here is accumulated by the transported observable and is hence more akin to the Landsberg phase [184, 185], originally developed to describe the driving of classical dissipative systems. The ability to control currents, particularly in the case of heat, via an external driving protocol is of profound importance in context of building quantum thermal machines at the nanoscale [67–71].

Beyond the period averaged pumped current, geometric contributions are also known to manifest themselves in the full counting statistics, which encode the complete knowledge of transport process in question, including all higher order fluctuations [58, 186–188]. In recent years, several studies have demonstrated that such fluctuations can be accessed experimentally [189–193] and such measurements have important applications in metrology, such as in Johnson thermometry [61, 194]. Importantly, the presence of geometric contributions within the distribution function describing the transport means that the exchange fluctuation theorems known for static systems, introduced in Sec. 4.2.2, cannot be applied in the driven regime, without the consideration of the additional energy input of the driving source [58–62].

Geometric contributions to transport statistics are of particular interest for scenarios where the manipulation in question is topologically protected, in which case the geometric phase accumulated throughout the evolution shares this protection. One such example, that will form the main focus of this chapter, is the Majorana braiding protocol outlined in Sec. 2.4. Since they form one of the key building blocks in the pursuit of the realisation of topological quantum computation [23, 24, 29], understanding the signatures of such operations is of significant interest, in readiness for potential future experiments. It is known that heat transport, in particular, is non-trivially affected by

the presence of Majorana zero modes [195–197] and it has been recently demonstrated that a braiding operation would be expected to prompt a finite heat pumping between two external leads that, in the low temperature limit, is characterised by a universal value, independent of the driving details and coupling strength to the leads [57].

Motivated by these findings, it becomes of interest to explore how these topologically protected geometric contributions are reflected in the full counting statistics of transport induced by a Majorana exchange and, furthermore, how such contributions affect the relevant heat exchange fluctuation theorems.

## 6.1 Full counting statistics for pumped heat transport

Our system of interest throughout this chapter takes the form of that sketched in Fig. 3.1, where our sample of interest is connected to $\mathcal{N} = 2$ particle reservoirs via conducting leads. With the ultimate goal of studying the behaviour of thermal fluctuation theorems in driven topological systems, we require access to the full statistical distribution of the heat transport between these two leads. Consequently, we must calculate the probability distribution $P(Q_\alpha, \tau)$ for the heat $Q_\alpha$ entering the lead $\alpha$ in some time period $\tau$. This can be calculated via the characteristic function (CF) $\chi_{Q_\alpha}(\lambda_\alpha)$, defined as

$$\chi_{Q_\alpha}(\lambda_\alpha) = \int dQ_\alpha e^{i\lambda_\alpha Q_\alpha} P(Q_\alpha, \tau), \tag{6.1}$$

where $\lambda_\alpha$ denotes the counting field. The CF for heat can be calculated analogously to the case of charge FCS [198] using the following expectation operator,

$$\chi_{Q_\alpha}(\lambda_\alpha) = \langle e^{i\lambda_\alpha \hat{Q}_\alpha^{\rightarrow}} e^{-i\lambda_\alpha \hat{Q}_\alpha^{\leftarrow}} \rangle. \tag{6.2}$$

Here the operators $\hat{Q}_\alpha^{\rightarrow/\leftarrow}$ describe the heat flow associated with ingoing/outgoing scattering states and can be written as the particle number operators in each direction, weighted by the energy measured with respect to the chemical potential:

$$\begin{aligned} \hat{Q}_\alpha^{\rightarrow} &= \frac{\tau}{h}\int_{-\infty}^{\infty} dE(E-\mu_\alpha)\hat{a}_\alpha^\dagger(E)\hat{a}_\alpha(E) \\ \hat{Q}_\alpha^{\leftarrow} &= \frac{\tau}{h}\int_{-\infty}^{\infty} dE(E-\mu_\alpha)\hat{b}_\alpha^\dagger(E)\hat{b}_\alpha(E). \end{aligned} \tag{6.3}$$

As discussed in Chap. 3, the ingoing and outgoing particle operators in the external leads are connected by the scattering matrix $S$. Since the setup under consideration consists of just two external leads and we would like to consider superconducting systems, this relationship can be expressed as

$$\begin{pmatrix} \hat{b}_{L^e}(E') \\ \hat{b}_{L^h}(E') \\ \hat{b}_{R^e}(E') \\ \hat{b}_{R^h}(E') \end{pmatrix} = S(E',E) \begin{pmatrix} \hat{a}_{L^e}(E) \\ \hat{a}_{L^h}(E) \\ \hat{a}_{R^e}(E) \\ \hat{a}_{R^h}(E) \end{pmatrix}. \tag{6.4}$$

The CF in Eq. 6.2 has been previously evaluated using a scattering matrix formalism for the case of charge transfer between superconducting leads in static systems [198]. We extend this analysis hereafter, to the case of heat transport in slowly driven systems.

### 6.1.1 Slow and small amplitude driving limit

As discussed in Sec. 3.2.1, determining the general form of the inelastic scattering matrix $S(E', E)$ is a highly non-trivial problem. We choose to study a model subjected to two important approximations. Firstly, we assume that the driving of the system is slow, so that the driving period is large compared to the electron dwell time in the scattering region. This corresponds to the limit $\hbar\omega \ll \delta E$, introduced in Eq. 3.37, where $\delta E$ corresponds to the scattering matrix resonance width. This will allow us to utilise the so-called frozen scattering matrix, $S(E, t)$, introduced in Sec 3.2.1. This limit is appropriate for the study of Majorana manipulation, which must be performed slowly with respect to other relevant energy scales to avoid excitations out of the degenerate ground-space. Secondly, we will operate under the assumption that the amplitude of the driving, in the relevant parameter space of the system, is small. This will allow the Fourier expansion of $S(E, t)$ to be curtailed at first order and hence only inelastic scattering events between nearest energy sidebands of energies $E \pm \hbar\omega$ are relevant. This significantly simplifies the calculation of the CF and additionally, in Sec. 6.4, we demonstrate that the geometric contributions to the transport properties yielded from this approach can be extended to larger amplitude cycles and in particular to a Majorana braiding protocol, our chosen system of interest.

With these approximations in mind, we can consider a general system described by some Hamiltonian $H(t)$ which depends implicitly on time through the periodic modulation of a set of parameters $\{X_j(t)\}$ with driving frequency $\omega$:

$$X_j(t) = X_{j,0} + X_{j,\omega} e^{i(\omega t - \eta_j)} + X_{j,\omega} e^{-i(\omega t - \eta_j)}. \tag{6.5}$$

Here, $\eta_j$ is an arbitrary phase factor. Under the assumption that the amplitude of this modulation is weak, so that $X_{j,\omega} \ll X_{j,0}\ \forall j$, the frozen scattering matrix can be approximated as [199]

$$S(\epsilon,t) \approx\ S(\epsilon, X_{j,0}) + S_\omega(\epsilon)e^{-i\omega t} + S_{-\omega}(\epsilon)e^{i\omega t},\ \text{ where } S_{\pm\omega} = \sum_j X_{j,\omega} e^{\mp i\eta_j} \frac{\partial S}{\partial X_j}. \quad (6.6)$$

By comparison with the zeroth order approximation of the Floquet scattering matrix, given in Eq. 3.33, one can deduce that the operator responsible for annihilating an outgoing scattered state can be written as

$$\hat{b}_\alpha(\epsilon) = \sum_\beta \Big( S^{\alpha\beta}(\epsilon)\hat{a}_\beta(\epsilon) + S^{\alpha\beta}_{-\omega}(\epsilon)\hat{a}_\beta(\epsilon+\omega) + S^{\alpha\beta}_{+\omega}(\epsilon)\hat{a}_\beta(\epsilon-\omega)\Big). \quad (6.7)$$

This expression further highlights that we are restricted to the regime for which only elastic and nearest-energy sideband scattering events are of relevance.

The evaluation of the heat flow operators defined in Eq. 6.3, and subsequently of the CF, requires the calculation of the number operators for states traveling both towards and away from the scattering region, defined as

$$\hat{N}^{L^{e(h)}}_{\rightarrow}(\epsilon) = \hat{a}^\dagger_{L^{e(h)}}(\epsilon)\hat{a}_{L^{e(h)}}(\epsilon)\ \text{ and }\ \hat{N}^{L^{e(h)}}_{\leftarrow}(\epsilon) = \hat{b}^\dagger_{L^{e(h)}}(\epsilon)\hat{b}_{L^{e(h)}}(\epsilon). \quad (6.8)$$

These operators can both be compactly expressed in terms of the ingoing scattering states in a discretized energy basis as

$$\hat{N}^{L^{e(h)}}_{\rightarrow(\leftarrow)}(\epsilon_l) = \sum_{\substack{\alpha,\beta \\ \epsilon_i,\epsilon_j}} \Big[P^{L^{e(h)}}_{\rightarrow(\leftarrow)}(\epsilon_l)\Big]^{\alpha\beta}_{\epsilon_i\epsilon_j} \hat{a}_\alpha(\epsilon_i)^\dagger \hat{a}_\beta(\epsilon_j), \quad (6.9)$$

using projective matrices $P$. Since the ingoing scattering matrices are diagonal in both the discretized energy and electron-hole bases, we have that

$$\Big[P^{L^{e(h)}}_{\epsilon_l\rightarrow}\Big]^{\alpha\beta}_{\epsilon_i\epsilon_j} = \delta_{\alpha L^{e(h)}}\delta_{\alpha\beta}\delta_{\epsilon_i\epsilon_l}\delta_{\epsilon_i\epsilon_j}. \tag{6.10}$$

Whereas the possibility of inelastic scattering events results in a non-diagonal matrix being used to define the outgoing number operators:

$$\begin{aligned}\Big[P^{L^{e(h)}}_{\epsilon_l\leftarrow}\Big]^{\alpha\beta}_{\epsilon_i\epsilon_j} &= \delta_{\epsilon_i\epsilon_l}\Big(S^{\alpha L^{e(h)}}(\epsilon_l)\Big)^*\Big(S^{L^{e(h)}\beta}(\epsilon_l)\delta_{\epsilon_i\epsilon_j} + S^{L^{e(h)}\beta}_{-\omega}(\epsilon_l)\delta_{(\epsilon_i+\omega)\epsilon_j} + S^{L^{e(h)}\beta}_{\omega}(\epsilon_l)\delta_{(\epsilon_i-\omega)\epsilon_j}\Big)\\ &+\delta_{\epsilon_i(\epsilon_l+\omega)}\Big(S^{\alpha L^{e(h)}}_{-\omega}(\epsilon_l)\Big)^*\Big(S^{L^{e(h)}\beta}(\epsilon_l)\delta_{(\epsilon_i-\omega)\epsilon_j} + S^{L^{e(h)}\beta}_{-\omega}(\epsilon_l)\delta_{\epsilon_i\epsilon_j} + S^{L^{e(h)}\beta}_{\omega}(\epsilon_l)\delta_{(\epsilon_i-2\omega)\epsilon_j}\Big)\\ &+\delta_{\epsilon_i(\epsilon_l-\omega)}\Big(S^{\alpha L^{e(h)}}_{\omega}(\epsilon_l)\Big)^*\Big(S^{L^{e(h)}\beta}(\epsilon_l)\delta_{(\epsilon_i+\omega)\epsilon_j} + S^{L^{e(h)}\beta}_{-\omega}(\epsilon_l)\delta_{(\epsilon_i+2\omega)\epsilon_j} + S^{L^{e(h)}\beta}_{\omega}(\epsilon_l)\delta_{\epsilon_i\epsilon_j}\Big).\end{aligned} \tag{6.11}$$

By expressing the heat flow operators $\hat{Q}^{\rightarrow/\leftarrow}_{\alpha}$ in terms of the matrices $P$, the CF in Eq. 6.2 reads

$$\chi_{Q_\xi}(\lambda_\xi) = \Big\langle \exp\Big(i\tau\lambda_\xi \sum_{\substack{\alpha,\beta\\ \epsilon_i,\epsilon_j}} \Big[C^\xi\Big]^{\alpha\beta}_{\epsilon_i\epsilon_j}\hat{a}^\dagger_\alpha(\epsilon_i)\hat{a}_\beta(\epsilon_j)\Big)\exp\Big(-i\tau\lambda_\xi \sum_{\substack{\alpha,\beta\\ \epsilon_i,\epsilon_j}} \Big[D^\xi\Big]^{\alpha\beta}_{\epsilon_i\epsilon_j}\hat{a}_\alpha(\epsilon_i)^\dagger\hat{a}_\beta(\epsilon_j)\Big)\Big\rangle, \tag{6.12}$$

with $C^\xi = \sum_i \epsilon_i P^\xi_{\epsilon_i\rightarrow}$, $D^\xi = \sum_i \epsilon_i P^\xi_{\epsilon_i\leftarrow}$ and the sum of the electron and hole number operator matrices defined as $P^\xi_{\epsilon_i\rightarrow} = P^{\xi^e}_{\epsilon_i\rightarrow} + P^{\xi^h}_{\epsilon_i\rightarrow}$. Under the condition that the matrices $P$ are projective, as demonstrated in Appendix B, it can be shown [198] that the expectation values in Eq. 6.12 are evaluated as

$$\chi_{Q_\xi}(\lambda_\xi) = \Big[\det\Big(1-\rho+\rho e^{i\lambda C^\xi}e^{-i\lambda D^\xi}\Big)\Big]^\tau = \Big[\det\big(M^\xi(\lambda_\xi)\big)\Big]^\tau, \tag{6.13}$$

with $M^\xi(\lambda_\xi) = 1-\rho+\rho e^{i\lambda_\xi\sum_i\epsilon_i P^\xi_{\epsilon_i\rightarrow}}\Big(1+\sum_i P^\xi_{\epsilon_i\leftarrow}(e^{-i\lambda_\xi\epsilon_i}-1)\Big)$. Here, the relevant

density matrix $\rho$ is block diagonal in the energy basis, with the block at each energy $\epsilon$ being given by $\rho_{\alpha\beta}(\epsilon) = \langle \hat{a}^\dagger_\alpha(\epsilon)\hat{a}_\beta(\epsilon)\rangle = f_\alpha(\epsilon)\delta_{\alpha\beta}$.

In general, the matrix $M^\xi(\lambda_\xi)$ will be of block pentadiagonal form in an infinite energy basis, making the calculation of the determinant a highly non-trivial exercise. In order to make further analytical progress, we divide the matrices $P^\xi_{\epsilon_i\leftarrow}$ into two contributions as $P^\xi_{\epsilon_i\leftarrow} = P^{\xi,0}_{\epsilon_i\leftarrow} + \tilde{P}^\xi_{\epsilon_i\leftarrow}$. Here, $P^{\xi,0}_{\epsilon_i\leftarrow}$ includes only contributions arising from elastic scattering events that survive in the static limit and $\tilde{P}^\xi_{\epsilon_i\leftarrow}$ encompasses all contributions arising from the periodic driving. This allows us to split the matrix $M^\xi$ in a similar fashion as $M^\xi = M^\xi_0 + \tilde{M}^\xi$. Where

$$\begin{aligned} M^\xi_0 &= 1 - \rho + \rho \exp\left( i\lambda \sum_i \epsilon_i P^\xi_{\epsilon_i\rightarrow} \right) \left( 1 + \sum_i P^{\xi,0}_{\epsilon_i\leftarrow}(e^{-i\lambda\epsilon_i} - 1) \right), \\ \tilde{M}^\xi &= \rho \exp\left( i\lambda \sum_i \epsilon_i P^\xi_{\epsilon_i\rightarrow} \right) \left( \sum_i \tilde{P}^\xi_{\epsilon_i\leftarrow}(e^{-i\lambda\epsilon_i} - 1) \right), \end{aligned} \tag{6.14}$$

with

$$P^{\xi^e,0}_{\epsilon_i\leftarrow} = \begin{pmatrix} \ddots & & & & & & \\ & 0 & & & & & \\ & & 0 & & 0 & & \\ & & 0 & S^{\alpha\xi^e}(\epsilon_i)^* S^{\xi^e\beta}(\epsilon_i) & 0 & & \\ & & 0 & & 0 & & \\ & & & & & 0 & \\ & & & & & & \ddots \end{pmatrix}$$

and

$$\tilde{P}^{\xi^e}_{\epsilon_i\leftarrow} = \begin{pmatrix} \ddots & & & & & \\ & 0 & & & & \\ & & S^{\alpha\xi^e}_{\omega}(\epsilon_i)^* S^{\xi^e\beta}_{\omega}(\epsilon_i) & S^{\alpha\xi^e}_{\omega}(\epsilon_i)^* S^{\xi^e\beta}(\epsilon_i) & S^{\alpha\xi^e}_{\omega}(\epsilon_i)^* S^{\xi^e\beta}_{-\omega}(\epsilon_i) & \\ & & S^{\alpha\xi^e}(\epsilon_i)^* S^{\xi^e\beta}_{\omega}(\epsilon_i) & 0 & S^{\alpha\xi^e}(\epsilon_i)^* S^{\xi^e\beta}_{-\omega}(\epsilon_i) & \\ & & S^{\alpha\xi^e}_{-\omega}(\epsilon_i)^* S^{\xi^e\beta}_{\omega}(\epsilon_i) & S^{\alpha\xi^e}_{-\omega}(\epsilon_i)^* S^{\xi^e\beta}(\epsilon_i) & S^{\alpha\xi^e}_{-\omega}(\epsilon_i)^* S^{\xi^e\beta}_{-\omega}(\epsilon_i) & \\ & & & & 0 & \ddots \end{pmatrix}.$$

Corresponding expansions can be defined for the matrices $P^{\xi^h,0}_{\epsilon_i\leftarrow}$ and $\tilde{P}^{\xi^h}_{\epsilon_i\leftarrow}$. Through these definitions, the cumulant generating function (CGF) $G_{Q_\xi}(\lambda_\xi) = \ln \chi_{Q_\xi}(\lambda_\xi)$ can be reduced to the sum of two distinct contributions:

$$G_{Q_\xi}(\lambda_\xi) = \tau \ln\Big(\det\Big(M_0^\xi + \tilde{M}^\xi\Big)\Big) = \; G^{\text{elas}}_{Q_\xi}(\lambda_\xi) + G^{\text{pump}}_{Q_\xi}(\lambda_\xi) \tag{6.15}$$

where

$$G^{\text{elas}}_{Q_\xi}(\lambda_\xi) = \tau \ln\Big(\det\Big(M_0^\xi\Big)\Big),$$
$$G^{\text{pump}}_{Q_\xi}(\lambda_\xi) = \tau \,\text{Tr}\,\Big(\ln\Big(\mathcal{I} + (M_0^\xi)^{-1}\tilde{M}^\xi\Big)\Big),$$

with $\mathcal{I}$ denoting the identity matrix. Here, we have assigned the label $G^{\text{elas}}_{Q_\xi}(\lambda_\xi)$ to the contribution to the CGF arising from only elastic scattering events that would be present irrespective of whether or not the system is driven. The remaining contribution, arising from the driving itself, we call $G^{\text{pump}}_{Q_\xi}(\lambda_\xi)$. Since we are working in the limit of weak amplitude parameter modulation, $X_{j,\omega} \ll X_{j,0}\ \forall j$, this expression can be further simplified by only retaining terms up to order $\mathcal{O}(X_{j,\omega})^2$. Performing a Taylor

expansion of the small driven contribution to the CGF under this assumption results in the approximation

$$G^{\mathrm{pump}}_{Q_\xi}(\lambda_\xi) \approx \tau \,\mathrm{Tr}\left((M^\xi_0)^{-1}\tilde{M}^\xi - \frac{1}{2}\big((M^\xi_0)^{-1}\tilde{M}^\xi\big)^2\right), \tag{6.16}$$

which leads to a significant simplification of our calculation. Exploiting the block diagonal nature of the matrix $M^\xi_0$ in the discretized energy basis, and taking the continuous limit, the static contribution to the CGF reduces to an integral over all energies:

$$G^{\mathrm{elas}}_{Q_\xi}(\lambda_\xi) = \tau \int_{-\infty}^{\infty} d\epsilon \ln\big(\det\Big(M^\xi_0(\epsilon)\Big)\big). \tag{6.17}$$

Similarly, since the dynamic contribution can be expressed in the form of a matrix trace, the diagonal blocks at each energy can each be evaluated individually and in the continuous limit we have that

$$G^{\mathrm{pump}}_{Q_\xi}(\lambda_\xi) = \tau \int_{-\infty}^{\infty} d\epsilon \,\mathrm{Tr}\left[M^\xi_0(\epsilon)^{-1}\tilde{M}^\xi(\epsilon) - \frac{1}{2}\Big((M^\xi_0)^{-1}(\epsilon)\tilde{M}^\xi(\epsilon)\Big)^2\right]. \tag{6.18}$$

Eqs. 6.17 and 6.18 enable the determination of the heat transport statistics and fluctuation theorem for weakly and adiabatically driven systems from scattering matrices and constitute the first main results of this work.

In the case that the Hamiltonian is subjected to the simultaneous driving of just two parameters, the dynamic contribution to the CGF can be further separated into two distinct contributions. The first consists of terms that depend on only one of the parameters and are hence proportional to $X^2_{j,\omega}$. This contribution remains present in the case that only one parameter is driven and is independent of the direction of traversal of the driving contour in parameter space. The remaining contribution is, in contrast,

geometric in nature and hence only depends upon the path traced out in parameter space throughout the driving. This contribution, which we denote as $G^{\text{geom}}_{Q_\xi}(\lambda_\xi)$, is independent of the driving frequency and identified by its proportionality to $X_{1,\omega}X_{2,\omega}$. The fact that the sign of this contribution is sensitive to the driving direction allows for the possibility of this contribution being isolated from the static and non-geometric pumped contributions in an experiment capable of accessing the FCS of heat transport.

### 6.1.2 Application to charge transport

Here, we briefly outline how the calculation in the previous section can be applied to the case of electronic transport properties. Analogously to the case of heat transport, the CF associated with the transport of charge $q_\xi$ into the lead $\xi$ in some time $\tau$ can be expressed as

$$\chi_{q_\xi}(\lambda_\xi) = \left\langle e^{i\lambda_\xi \hat{q}_\xi^{\rightarrow}} e^{-i\lambda_\xi \hat{q}_\xi^{\leftarrow}} \right\rangle, \tag{6.19}$$

with ingoing and outgoing charge operators defined as

$$\hat{q}_\xi^{\rightarrow(\leftarrow)} = e\tau \int d\epsilon \Big( \hat{N}^{\xi^e}_{\rightarrow(\leftarrow)}(\epsilon) - \hat{N}^{\xi^h}_{\rightarrow(\leftarrow)}(\epsilon) \Big) \tag{6.20}$$

and where $e$ is the unit of electronic charge. This expression reflects the fact that electrons and holes carry electronic current in opposite directions when traveling in the same direction, in contrast to the case of heat current. From here, corresponding expressions for the CGF can be derived and take the form

$$\begin{aligned} G^{\text{elas}}_{q_\xi}(\lambda) =& \tau \int_{-\infty}^{\infty} d\epsilon \ln\big( \det\Big( M^{\xi}_{q,0}(\epsilon) \Big) \big). \\ G^{\text{pump}}_{q_\xi}(\lambda) =& \tau \int_{-\infty}^{\infty} d\epsilon \, \text{Tr}\Big( M^{\xi}_{q,0}(\epsilon)^{-1} \tilde{M}^{\xi}_{q}(\epsilon) \Big), \end{aligned} \tag{6.21}$$

where now

$$
\begin{aligned}
M^{\xi}_{q,0} &= 1-\rho+\rho\exp\left(i\lambda_{\xi}\sum_i P^{\xi}_{\epsilon_i\rightarrow}\right)\left(1+\sum_i P^{\xi,0}_{\epsilon_i\leftarrow}(e^{-i\lambda_{\xi}}-1)\right),\\
\tilde{M}^{\xi}_{q} &= \rho\exp\left(i\lambda_{\xi}\sum_i P^{\xi}_{\epsilon_i\rightarrow}\right)\left(\sum_i \tilde{P}^{\xi}_{\epsilon_i\leftarrow}(e^{-i\lambda_{\xi}}-1)\right).
\end{aligned}
\tag{6.22}
$$

In this case, $P_{\epsilon_i\rightarrow(\leftarrow)} = P^{e}_{\epsilon_i\rightarrow(\leftarrow)} - P^{h}_{\epsilon_i\rightarrow(\leftarrow)}$ and the matrices $P^{e(h)}_{\epsilon_i\rightarrow(\leftarrow)}$ are defined as in Eq. 6.10 and 6.11. These results are again valid for any cyclically driven system for which the driving can be considered weak and slow with respect to the scattering time.

## 6.2 Model: Majorana braiding cycle

In this section, we apply our expressions for the full counting statistics of heat and charge transport to a concrete example of a topologically non-trivial system subjected to periodic driving, in the form of a Majorana braiding protocol (see Sec. 2.4). We consider the minimum setup required to achieve a Majorana exchange using only 1D $p$-wave superconducting nanowires, similar to the system illustrated in Fig. 2.5(c). Executing a braiding by tuning the on-site potential locally along the wire, as described in Sec. 2.4.2, requires precise control over the system that may be challenging in practice. Furthermore, the opening and closing of the band gap along the wire increases the likelihood of unwanted non-adiabatic excitations during the manipulation [200, 201]. A protocol that effectively braids the Majorana operators without physically manipulating their positions is therefore desirable. Our system of interest consists of three nanowires arranged in a Y-junction configuration, as sketched in Fig. 6.1(a). Each of the superconducting wires hosts a MZM at each end, however the interaction of

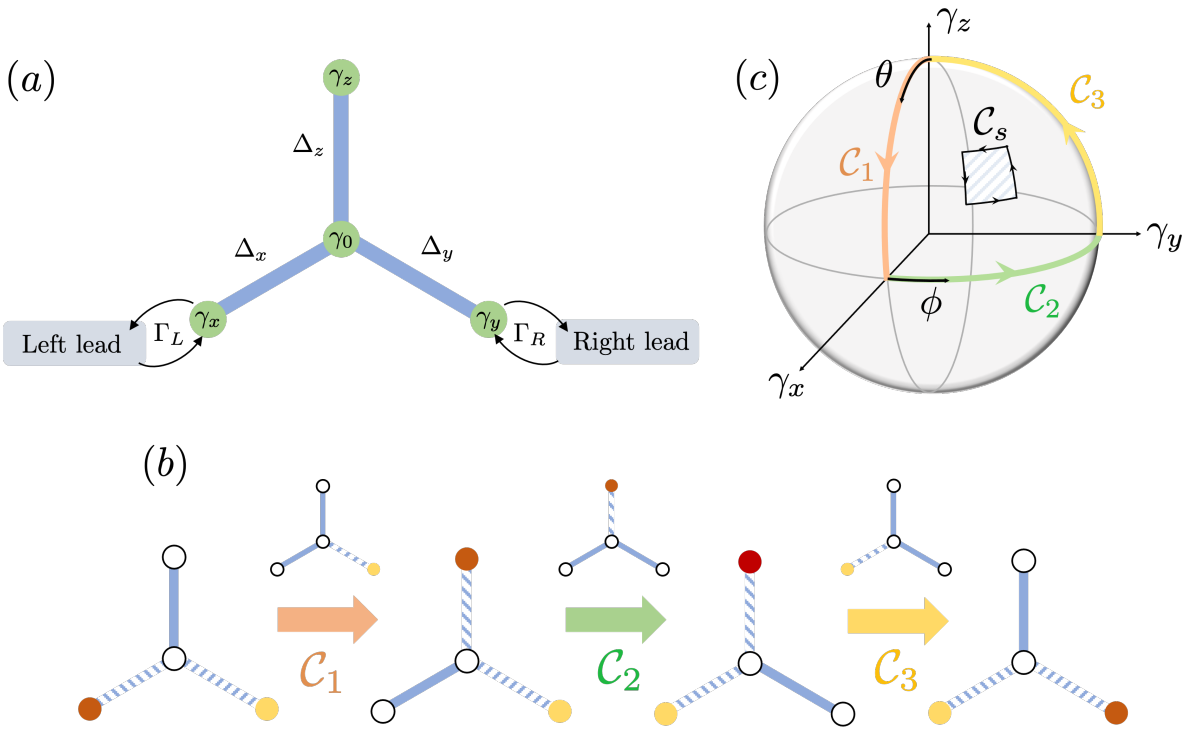


Figure 6.1: (a) Y-junction of $p$-wave superconducting nanowires (blue) with Majorana zero modes at positions indicted by the green dots. Each of the external Majorana modes, $\gamma_{x,y,z}$, are coupled to the central mode with corresponding coupling strengths $\Delta_{x,y,z}$ and the modes $\gamma_x$ and $\gamma_y$ are further coupled to conducting normal metal leads with strengths $\Gamma_L$ and $\Gamma_R$. (b) Illustration of the required sequence of couplings to perform a Majorana exchange, where the solid blue lines illustrate the couplings which are turned on and dashed lines indicate those that are turned off. White circles indicate Majoranas with a large Coulomb splitting whereas coloured circles correspond to those with a vanishly small Coulomb splitting. The small diagrams above each arrow show the intermediate steps with two couplings turned on and one of the zero energy Majoranas delocalised over the two corresponding external sites. (c) The corresponding evolution, $\mathcal{C}_1+\mathcal{C}_2+\mathcal{C}_3$, is shown as a path in spherical parameter space on the left. Also illustrated is an example of a small amplitude driving contour $\mathcal{C}_s$.

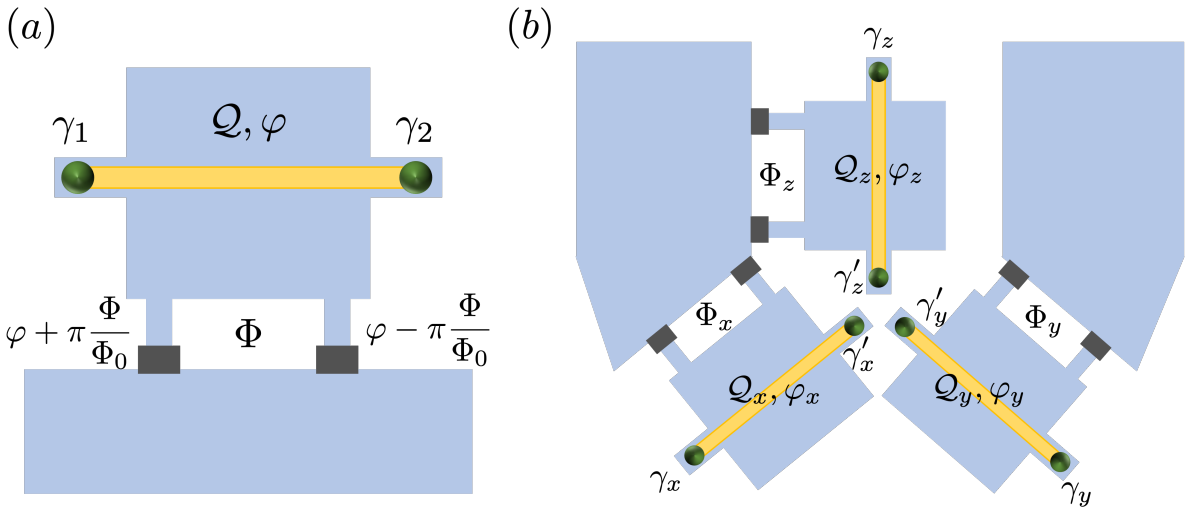


Figure 6.2: (a) Schematic of a Cooper pair box composed of a superconducting island (blue), carrying charge $\mathcal{Q}$ and superconducting phase $\varphi$, connected to a bulk superconductor via a split Josephson junction (grey). A nanowire (yellow) can be added to the island so that the system can host two MZMs when in the topological phase. These spatially separated Majoranas can be coupled using the Coulomb charging energy on the island, which can be tuned by changing the magnetic flux $\Phi$ passing through the Josephson junction. (b) Three Cooper pair boxes connected in a Y-junction configuration via the tunnel coupling between the three internal MZMs. By controlling the couplings between MZMs on the same island, this setup can be used to perform a Majorana exchange.

the three Majoranas that meet in the centre results in the ground-space of the system being spanned by just four Majorana states: $\gamma_x$, $\gamma_y$, $\gamma_z$ and $\gamma_0$, formed by a linear combination of the internal Majoranas from each wire. The Y-junction is coupled to left ($L$) and right ($R$) external metal leads, so that the transport properties associated with the braiding process can be probed. In the following we work in the limit that the lead temperature can be considered small with respect to both the magnitude of the superconducting gap in the nanowires and the tunnel coupling strength between the Majoranas at the centre of the junction. In this way, the transport is only mediated by the fourfold degenerate ground-space of the system.

It can be demonstrated that, by systematically modulating the couplings between each of the external MZMs and the central state $\gamma_0$, the states $\gamma_x$ and $\gamma_y$ can be exchanged [39, 202]. A proposal of how these couplings could be controlled in practice is illustrated in Fig. 6.2(a). The proposed system consists of a Cooper pair box: a superconducting island (charge $\mathcal{Q}$, capacitance $C$) connected to a bulk superconductor via a split Josephson junction enclosing a magnetic flux $\Phi$. The Hamiltonian describing such a device consists of the sum of charging and Josephson energies:

$$H_{\mathrm{CPB}} = \frac{\hat{\mathcal{Q}}^2}{2C} + E_J(\Phi)\cos(\varphi), \tag{6.23}$$

where $\varphi$ is the superconducting phase on the island, related to the charge operator as $\hat{\mathcal{Q}} = -2eid/d\varphi$. The Josephson energy takes the form $E_J(\Phi) = E_0\cos(e\Phi/\hbar)$, with $E_0$ corresponding to the coupling energy to the bulk superconductor [39, 201].

The addition of a segment of semiconducting nanowire allows the system to host two MZMs when in the topologically non-trivial phase. Although the MZMs themselves are charge neutral quasiparticles, an effective Coulomb interaction exists between them due to the fact that the charging energy of the Cooper pair box is related to the fermionic parity, $\hat{\mathcal{P}} = i\gamma_1\gamma_2$, of the island. This relationship can be expressed through the following constraint on the eigenstates of $H_{\mathrm{CPB}}$:

$$\Psi(\varphi + 2\pi) = (-1)^{\frac{1-\mathcal{P}}{2}}\Psi(\varphi), \tag{6.24}$$

ensuring that the eigenvalues of $\hat{\mathcal{Q}}$ are even multiples of $e$ for $\mathcal{P} = 1$ and odd multiples for $\mathcal{P} = -1$. It can be shown (see Ref. [39] for a detailed derivation) that, in the limit that $E_J$ is large compared to the single electron charging energy $E_C$, this condition

results in a contribution to the effective low energy Hamiltonian of the form

$$H_{\mathrm{CPB}}^{\mathrm{eff}} = -U(\Phi)\hat{\mathcal{P}} = -iU(\Phi)\gamma_1\gamma_2, \tag{6.25}$$

where $U(\Phi) \propto e^{-\sqrt{8E_J(\Phi)/E_C}}$. This leads to a Coulomb coupling between the spatially separated MZMs that can be controlled via the modulation of the magnetic flux through the split Josephson junction, avoiding the need for microscopic control of the system. The Josephson energy could alternatively be controlled electrostatically by the tuning of a gate voltage to modulate the transparency of the Josephson junction as proposed in Ref. [26]. The ratio $U_{\min}/U_{\max} \sim e^{-\sqrt{8E_0/E_C}}$ can be made exponentially small in the limit $E_0 \gg E_C$. We will see shortly that this factor governs the protection of the braiding protocol and the associated geometric transport properties.

Fig. 6.2(b) demonstrates how three Cooper pair boxes can be combined to create the Y-junction setup introduced in Fig. 6.1(a). Despite the existence of the proposals outlined here, in addition to alternative mechanisms based only upon executing projective measurements on the system of MZMs [203], the experimental realization of a Majorana exchange process is yet to be attempted.

The Hamiltonian for the Y-junction describing the time-dependent couplings $\Delta_i$ between the external MZMs $\gamma_i$ and $\gamma_0$ can be written as

$$H_Y = i\gamma_0\vec{\Delta}\cdot\vec{\gamma}, \tag{6.26}$$

where $\vec{\Delta} = (\Delta_x, \Delta_y, \Delta_z)$ and $\vec{\gamma} = (\gamma_x, \gamma_y, \gamma_z)$. The complete Hamiltonian for the system is then given by $H = H_Y + H_{\mathrm{coup}} + H_{\mathrm{leads}}$ where the contributions from the coupling to

the external leads and the leads themselves can be written as

$$\begin{aligned} H_{\text{coup}} &= \sqrt{\Gamma_L}(c_{Lk} - c_{Lk}^\dagger)\gamma_x + \sqrt{\Gamma_R}(c_{Rk} - c_{Rk}^\dagger)\gamma_y, \\ H_{\text{leads}} &= \sum_k \sum_{\alpha=L,R} \xi_{\alpha k} c_{\alpha k}^\dagger c_{\alpha k}, \end{aligned} \tag{6.27}$$

respectively. Here, $\Gamma_{L/R}$ denote the coefficients associated with particle tunneling from the leads onto the superconducting Y-junction and $\xi_{\alpha k}$ are the energy dispersion relations in the leads.

It can be shown [39] that the execution of the sequence of Coulomb couplings illustrated in Fig. 6.1(b) results in the exchange of the Majoranas $\gamma_x$ and $\gamma_y$. In order to better understand this evolution, it is useful to rewrite $H_Y$ using the basis vectors of a spherical coordinate system, letting $\Delta_x = \Delta \sin\theta \cos\phi$, $\Delta_y = \Delta \sin\theta \sin\phi$ and $\Delta_z = \Delta \cos\theta$, so that

$$\begin{aligned} H_Y = i\Delta\gamma_0\gamma_r, \text{ where } \gamma_r &= \vec{\gamma} \cdot (\sin\theta\cos\phi, \sin\theta\sin\phi, \cos\theta), \\ \gamma_\theta &= \vec{\gamma} \cdot (\cos\theta\cos\phi, \cos\theta\sin\phi, -\sin\theta), \\ \gamma_\phi &= \vec{\gamma} \cdot (-\sin\phi, \cos\phi, 0), \end{aligned} \tag{6.28}$$

for $\Delta \in [0, \infty]$, $\theta \in [0, \pi]$ and $\phi \in [0, 2\pi)$. The absence of the MZMs $\gamma_\theta$ and $\gamma_\phi$ in the Hamiltonian $H_Y$ indicates that these states span the two-fold degenerate ground-space throughout the braiding operation and the evolution of the system now corresponds to changing the projection of these zero-energy states onto the space of physical Majoranas $\gamma_x$, $\gamma_y$ and $\gamma_z$. The manipulation of the coupling strengths $\Delta_i$ can then be mapped to a rotation of $\gamma_r$ on the unit sphere as illustrated in Fig. 6.1(c). The exchange operation then corresponds to the curve $\mathcal{C} = \mathcal{C}_1 + \mathcal{C}_2 + \mathcal{C}_3$. We notice that only two of the Coulomb

couplings are switched on at any one time during this cycle. This constrains our path in parameter space to the plane spanned by the two corresponding Majoranas and hence fixes the contour, making it insensitive to any fluctuations in the two couplings being driven and only dependent upon the order in which the couplings are switched on/off. For example, along $\mathcal{C}_1$ the parameter $\phi = \arctan(\Delta_y/\Delta_x)$ is independent of both driven couplings $\Delta_x$ and $\Delta_z$, so long as $\Delta_y$ remains switched off. As a consequence, any geometric contributions to the transport statistics, that only depend upon the shape of this contour, will also inherit this protection. The robustness of the cycle is subject to errors of the order of the ratio $\Delta_i^{\min}/\Delta_i^{\max}$ which, as mentioned previously, is exponentially suppressed in the limit $E_0 \gg E_C$. It is thought that a ratio $\Delta_i^{\min}/\Delta_i^{\max} \approx 10^{-5}$ would be realistically achievable in practice [39, 204].

In the energy regime far below the gap associated with the superconducting wires, $\Delta_{\text{sc}}$, particle transport between the external leads can only occur via the occupation of the non-local fermionic state, $\hat{a} = \frac{1}{2}\big(\gamma_\theta + i\gamma_\phi\big)$, defined in terms of the ground-space Majoranas. The degeneracy associated with the occupation of this state is protected by the particle-hole symmetry of the system and the spatial separation of the constituent Majoranas. This affords further protection to the energy dependence of the low energy scattering events facilitated by the occupation of this state and the associated transport properties.

It can be shown that performing the sequence of couplings sketched in Fig. 6.1(b) corresponds to the operator $\hat{a}$ accumulating a phase factor $e^{i\Omega_{\mathcal{C}}}$, where $\Omega_{\mathcal{C}}$ denotes the solid angle enclosed by the curve, $\mathcal{C}$, traversed in parameter space during the cycle. For the case of the Majorana braiding we have that $\Omega_{\mathcal{C}} = \pi/2$ and this phase factor shares the topological protection of the braiding operation, as discussed in Sec. 2.4.

Executing the cycle results in system evolution described by the operator $U = e^{-\frac{\pi}{4}\gamma_\phi\gamma_\theta}$, corresponding to the desired exchange of the Majoranas $\gamma_x$ and $\gamma_y$:

$$U^\dagger\gamma_x U = \gamma_y \quad \text{and} \quad U^\dagger\gamma_y U = -\gamma_x. \tag{6.29}$$

It should be noted here that a full treatment of the effect of allowing electrons to coherently scatter between the external leads via the internal system upon the physical setup of coupled Cooper pair boxes has not been included in this work. Tunnelling events will certainly lead to changes in the fermionic parity of the system and hence limit its performance as a qubit when coupled to the leads. However, the assumption that the driving is slow enough for the scattering to be considered instantaneous should mean that such tunnelling events have a limited impact upon the evolution associated with the exchange process. Furthermore, the protection of the path in parameter space and the scattering properties are only reliant on the suppression of the ratio $\Delta_i^{\min}/\Delta_i^{\max}$ and the degeneracy of the ground state and hence these should remain unaffected by the coherent scattering of electrons from the leads. However, as with all Majorana braiding proposals, this protection is subject to the issue of quasi-particle poisoning from other environmental sources, as discussed in Sec. 2.5.

### 6.2.1 Determining the scattering matrix

Before calculating the FCS associated with the Majorana braiding protocol, we must first determine the form of the instantaneous scattering matrix $S(\epsilon, t)$ associated with the Y-junction. This can be achieved via the use of the so-called Mahaux-Weidenmuller

formula [205]:

$$S(\epsilon,t) = 1 + 2\pi i W^\dagger (H_Y(\theta(t),\phi(t)) - \epsilon - i\pi W W^\dagger)^{-1} W. \tag{6.30}$$

Here, $W$ is the contact matrix describing the coupling between the Y-junction and the external leads and its form can be deduced from the coupling Hamiltonian $H_{\text{coup}}$. In the basis of the physical MZMs, it takes the form

$$W = \sqrt{\Gamma_L}\Big( |\gamma_x\rangle \langle e^L| - |\gamma_x\rangle \langle h^L| \Big) + \sqrt{\Gamma_R}\Big( |\gamma_y\rangle \langle e^R| - |\gamma_y\rangle \langle h^R| \Big). \tag{6.31}$$

With this, the specific form of the scattering matrix for the Majorana braiding is found to be

$$\begin{aligned} S(\epsilon) &= \begin{pmatrix} S^{L^eL^e} & 1-S^{L^eL^e} & S^{L^eR^e} & -S^{L^eR^e} \\ 1-S^{L^eL^e} & S^{L^eL^e} & -S^{L^eR^e} & S^{L^eR^e} \\ S^{L^eR^e} & -S^{L^eR^e} & S^{R^eR^e} & 1-S^{R^eR^e} \\ -S^{L^eR^e} & S^{L^eR^e} & 1-S^{R^eR^e} & S^{R^eR^e} \end{pmatrix}, \\ \text{where } \; S^{L^eL^e} &= 1 - 4\pi i\Gamma\left( \frac{\sin^2\phi}{\epsilon + 2\pi i\Gamma} + \frac{\cos^2\theta\cos^2\phi}{\epsilon + 2\pi i\cos^2\theta\Gamma} \right), \\ S^{R^eR^e} &= 1 - 4\pi i\Gamma\left( \frac{\cos^2\phi}{\epsilon + 2\pi i\Gamma} + \frac{\cos^2\theta\sin^2\phi}{\epsilon + 2\pi i\cos^2\theta\Gamma} \right), \\ \text{and } \; S^{L^eR^e} &= \frac{4\pi i\epsilon\cos\phi\sin^2\theta\sin\phi\Gamma^2}{(\epsilon + 2\pi i\Gamma)(\epsilon + 2\pi i\cos^2\theta\Gamma)}. \end{aligned} \tag{6.32}$$

Here we only show the case of equal coupling to the left and right leads, $\Gamma_L = \Gamma_R = \Gamma$, for brevity. The components of this scattering matrix can be used in Eq. 6.17 and 6.18 in order to determine the heat and charge transfer statistics of a driven Majorana Y-junction.

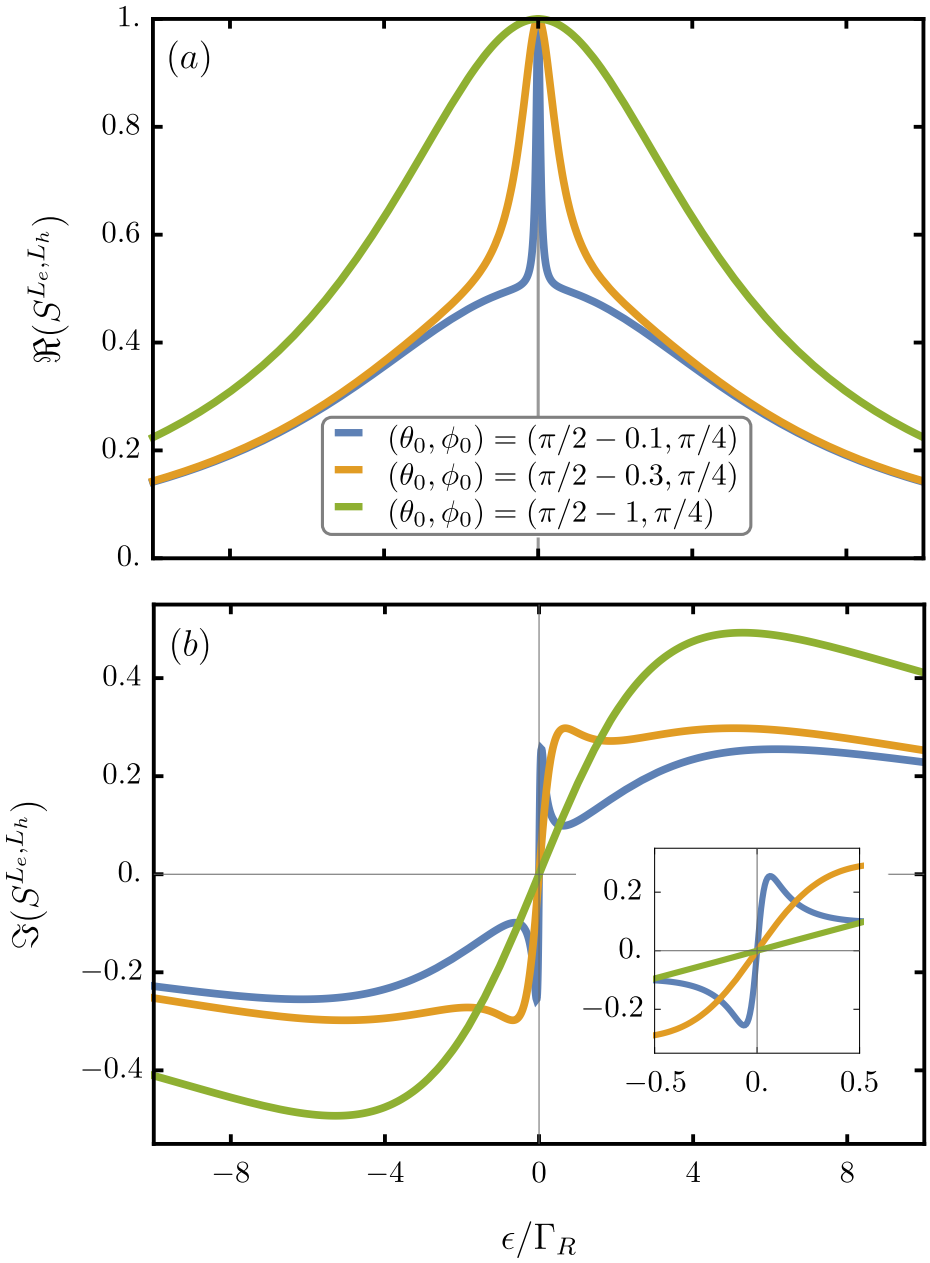


Figure 6.3: (a) Real and (b) imaginary parts of the Andreev reflection component of the scattering matrix for the topological superconducting Y-junction. Results are plotted for several positions in the parameter space, $(\theta_0, \phi_0)$, and for equal coupling to the left and right external leads $\Gamma_L = \Gamma_R$.

The expressions for the scattering matrix components allow for the identification of two distinct energy scales that will shape the transport properties of the system. The energy dependence of the real and imaginary parts of the Andreev reflection component of the scattering matrix $S^{L_e,L_h}(\epsilon)$ are shown in Fig. 6.3(a) and (b) respectively. We see that the real part comprises of the sum of two peaks centered at $\epsilon = 0$. The width of the larger of these two peaks is set by the strength of the coupling to the external leads $\Gamma_{L/R}$. However, at energies close to $\epsilon = 0$ the behaviour is denominated by a narrower peak with a width given by $\Gamma_R \cos^2\theta$ and which is controlled by the location in parameter space $(\theta, \phi)$, with the width decreasing as we approach the equator corresponding to the line $\theta = \pi/2$.

From Fig. 6.3 we also learn that the real and imaginary components exhibit different energy dependence in the limit $\epsilon \to 0$. Whereas the real part can be approximated as constant in this limit, the imaginary part varies linearly with energy and hence quantities that include this contribution will show sensitivity to the energy dependence of the scattering matrix, even in the limit $T \to 0$.

## 6.3 Heat and charge transport statistics for small amplitude cycles

With the ultimate goal of studying the FCS of a Majorana braiding cycle, we start by considering the situation wherein our superconducting Y-junction is driven through some small amplitude cycle in the parameter space $(\theta, \phi)$. Such cycles also result in the manipulation of the projection of the MZMs $\gamma_\theta$ and $\gamma_\phi$ in the space spanned by the physical Majoranas, but do not correspond to an exchange process and hence the

corresponding contours in parameter space are not protected against fluctuations in the driving. In this scenario one can utilise our expressions for the elastic and dynamic contributions to the CGF given in Eq. 6.17 and 6.18 respectively.

In order to focus attention on the contributions to the transport arriving purely from the periodic driving, we will study the case in which we have no chemical potential or temperature biases between the leads, so that $\mu_L = \mu_R = 0$ and $T_L = T_R = T$. Accordingly, the distribution functions for electrons and holes in each lead are identical: $f_{\rm in}^{L^e}(\epsilon) = f_{\rm in}^{L^h}(\epsilon) = f_{\rm in}^{R^e}(\epsilon) = f_{\rm in}^{R^h}(\epsilon)$. Our analysis will focus on the energy regime far below the superconducting gap and upon the case for which the driving can be considered slow compared to the scattering time, so that $\omega \ll \Gamma_{L,R} \ll \Delta_{\rm sc}$.

The CGF provides access to all the higher order cumulants for both heat, $\mathcal{M}_{Q_\xi}^{(k)}$, and charge, $\mathcal{M}_{q_\xi}^{(k)}$, transport in the lead $\xi$ via the derivatives with respect to the counting field:

$$\mathcal{M}_{Q_\xi}^{(k)} = \left.\frac{\partial^k G_{Q_\xi}(\lambda_\xi)}{\partial(i\lambda_\xi)^k}\right|_{\lambda_\xi=0} \text{ and } \mathcal{M}_{q_\xi}^{(k)} = \left.\frac{\partial^k G_{q_\xi}(\lambda_\xi)}{\partial(i\lambda_\xi)^k}\right|_{\lambda_\xi=0}. \tag{6.33}$$

### 6.3.1 Elastic contributions

We first focus upon the contribution to the CGF that would survive in the static limit and therefore arises from elastic scattering events only. Since this quantity does not depend upon the driving, these results are valid for arbitrary amplitude cycles. The elastic component of the CGF for heat transport takes the form

$$G_{Q_L}^{\rm elas}(\lambda_L) = \mathcal{T}\int_{-\infty}^{\infty} d\epsilon \ln\left(1 + \sum_{n=-1}^{1} B_n(\epsilon)(e^{i\lambda_L \epsilon n} - 1)\right), \tag{6.34}$$

where $\mathcal{T}$ denotes the period of the driving and the coefficients $B_n(\epsilon)$ take the form

$$B_1(\epsilon) = B_{-1}(\epsilon) = 4|S^{L^e,R^e}(\epsilon,\theta_0,\phi_0)|^2 f(\epsilon)\big(1-f(\epsilon)\big). \tag{6.35}$$

Here, $(\theta_0,\phi_0)$ corresponds to the location of the driving cycle centre in parameter space. Written in this form it becomes evident that heat can only be transferred to or from the external leads via normal and Andreev transmission events involving electrons and holes. The coefficients $B_n(\epsilon)$ capture the probability of scattering events resulting in the transfer of $n$ particles from the lead $\xi$ into other leads. For example, the transmission of an electron from the left to the right lead will occur with a probability of $|S^{L^eR^e}(\epsilon)|^2 f(\epsilon)(1-f(\epsilon))$, as expected. The corresponding expression for charge transport is found to be

$$G^{\text{elas}}_{q_L}(\lambda_L) = \mathcal{T}\int_{-\infty}^{\infty} d\epsilon \ln\left(1+\sum_{n=-2}^{2} B_n(\epsilon)(e^{i\lambda_L n}-1)\right), \tag{6.36}$$

where

$$B_{-1}(\epsilon) = B_1(\epsilon) = 4|S^{L^eR^e}(\epsilon,\theta_0,\phi_0)|^2 f(\epsilon)\big(1-f(\epsilon)\big),$$
$$B_{-2}(\epsilon) = B_2(\epsilon) = |S^{L^eL^h}(\epsilon,\theta_0,\phi_0)|^2 f(\epsilon)\big(1-f(\epsilon)\big).$$

In the case of electronic transport, we see that, in addition to transmission events, Andreev reflection also contributes via the creation or annihilation of Cooper pairs in the superconducting Y-junction. These processes result in the propagation of an electronic charge of $\pm 2e$, but no energy transport in the form of heat.

Of course, in the absence of chemical potential and temperature biases between the leads, the contribution to the average heat and charge currents arising from the elastic CGF are identically zero $\langle \hat{Q}^{\text{elas}} \rangle = \langle \hat{q}^{\text{elas}} \rangle = 0$. Despite this, the thermal fluctuations

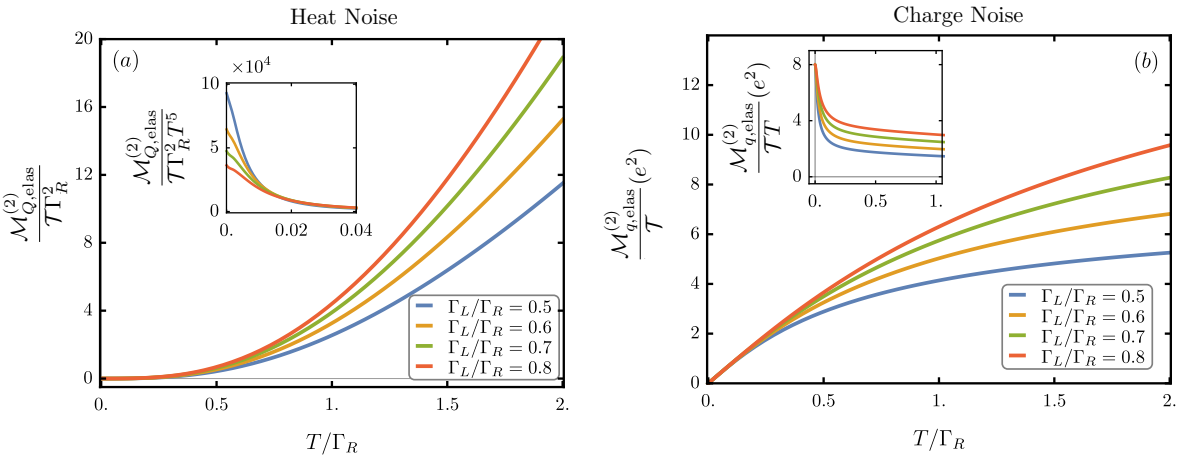


Figure 6.4: Period-averaged static contribution to the second cumulant of (a) the pumped heat and (b) pumped charge throughout the driving of a Majorana Y-junction centred at $(\theta_0, \phi_0) = (\pi/2 - 0.1, \pi/4)$, with amplitude $\theta_\omega = \phi_\omega = 0.01$. The noise is plotted as a function of the external lead temperature $T/\Gamma_R$, for a driving frequency $\omega/\Gamma_R = 0.001$. The insets show the temperature dependence of this quantity scaled by $T^5$ and $T$ for heat and charge respectively, highlighting the behaviour as $T \to 0$. The different colours correspond to various values of the coupling between the Y-junction and the external leads $\Gamma_L/\Gamma_R$ (cf. legend).

in the occupation of ingoing scattering states result in a contribution to the second cumulant from elastic processes. Such contributions are present in the FCS for both heat and charge transport and their behaviour as a function of the lead temperature for each case are illustrated in Fig. 6.4(a) and (b) respectively. For both heat and charge transport, the elastic contribution to the noise vanishes in the limit $T = \mu = 0$, in which case the occupation probability of all ingoing states is fixed and no charge or energy transfer processes take place. From the behaviour sketched in Fig. 6.4, it is natural to identify two distinct temperature regimes relative to the coupling strength to the external leads.

### Thermal noise at low temperature

In the low temperature regime, $T \ll \min \Gamma_{L/R}$, the energy dependence of the frozen scattering matrix can be considered weak and consequently the dominating factor in the energy dependence of the thermal noise should arise from the combination of Fermi distribution functions, $f(\epsilon)$, appearing in the elastic component of the CGF (Eqs. 6.34, 6.36). If the scattering matrix is taken to be energy independent, the form of the elastic CGF implies that the thermal charge noise should vary linearly in $T$, whereas for the case of heat this quantity should vary as $T^3$ [141, 199].

The elastic contribution to the second cumulant of both heat and charge transport for the example of the driven Y-junction are plotted in Figs. 6.4(a) and (b) respectively. The insets within each plot highlight the behaviour at low temperatures. For the case of charge transport we see that, as anticipated, the energy dependence of the scattering matrix can be neglected and that the thermal noise scales linearly with temperature. Additionally, we see that the dependence upon the coupling strength to the leads is lost as $T \to 0$; a further consequence of weak energy dependence of the scattering matrix.

Conversely, we find that the thermal contribution to the heat noise maintains its sensitivity to the scattering matrix energy dependence in the low temperature regime. One can show that this property arises due to the fact that this contribution is influenced by the imaginary component of the scattering matrix which, as we see in Fig. 6.3(b), cannot be considered constant at energies close to $\epsilon = 0$. In fact, the removal of the energy dependence of the scattering matrix would result in the elastic part of the second cumulant for heat being identically zero. The result is that the elastic heat noise scales as $T^5$ in the limit $T \to 0$ and that the dependence upon the coupling strength $\Gamma$ remains evident at all temperatures.

We will soon see that, although the energy dependence of the scattering matrix, discussed in Sec. 6.2.1, could be neglected for the case of electronic transport thermal noise, its influence will be present in the transport cumulants arising from the driving, even in the limit of low temperatures.

**Thermal noise at high temperature**

As the temperature becomes comparable with the coupling strength to the external leads, the influence of the scattering matrix energy dependence can no longer be neglected for both heat and charge transport. Since the transport is facilitated by the MZMs, the scattering is dominated by low energy states and hence fluctuations in the occupation of higher energy states do not contribute to the noise, even as $T$ is increased. Consequently, we find that the rate of increase of the elastic contributions to the noise slows down at high temperatures, eventually reaching a constant value in the case of charge current and scaling linearly in $T$ in the case of heat. In Fig. 6.4 it can clearly be seen that this change occurs at a temperature of the order of the coupling strength $\Gamma$.

### 6.3.2 Average pumped heat and charge

We next focus upon the more interesting contributions to the FCS for transport arising from the time-dependent driving of the system. These are the charge and heat cumulants originating from the pumped contributions to the CGF introduced in Eq. 6.18. We start by considering the first order cumulants, describing the average heat and charge driven between the leads throughout the cycle. Still assuming the absence of temperature and chemical potential biases between the leads, one finds that the charge

pumped during any modulation of the Majorana Y-junction identically vanishes. This property occurs as a direct consequence of the particle-hole symmetry of the scattering processes between the MZMs and the leads. This result is in contrast to previous works studying adiabtic pumps in the absence of this symmetry, where the driven charge is found to vary linearly with the driving frequency [199].

In spite of the absence of charge pumping, the driven Y-junction is seen to facilitate the transfer of a finite heat current between the leads which, in the absence of biases, arises purely from the geometric contribution to the CGF $G^{\text{geom}}_{Q_\xi}(\lambda_\xi)$. This heat can be expressed as

$$\left\langle Q^{\text{pump}}_{\xi} \right\rangle = \left\langle Q^{\text{geom}}_{\xi} \right\rangle = 2 \int_0^\infty d\epsilon \; \epsilon \; Q_{0,\xi}(\epsilon) \frac{\partial f(\epsilon)}{\partial \epsilon}, \tag{6.37}$$

with

$$Q_{0,\xi}(\epsilon) = \iint d\theta d\phi \sum_{\beta = L^e, L^h, R^e, R^h} \text{Im} \left[ \frac{\partial S^{\xi^e \beta}(\epsilon)}{\partial \theta} \frac{\partial S^{\xi^e \beta}(\epsilon)}{\partial \phi} \right]. \tag{6.38}$$

Expressed in this way, as an integral over an area in parameter space spanned by $\theta$ and $\phi$, the geometric nature of the pumped heat becomes manifest. This quantity bares no dependence upon the driving frequency but is fixed by the path traversed in the parameter space. We will see (Sec. 6.4.1) that, since the pumped heat arises solely from the geometric contribution, this expression is equally valid for arbitrary amplitude cycles such as the Majorana braiding.

The extension of this expression to the example of a Majorana braiding is of significant interest due to the fact that the topological protection of this non-Abelian operation ensures that the path traversed in parameter space, $\mathcal{C}$ in Fig. 6.1(c), is immune to fluctuations in the driving mechanism. Therefore, any transport properties that are geometric in nature will share this protection. Furthermore, in the limit $T \to 0$

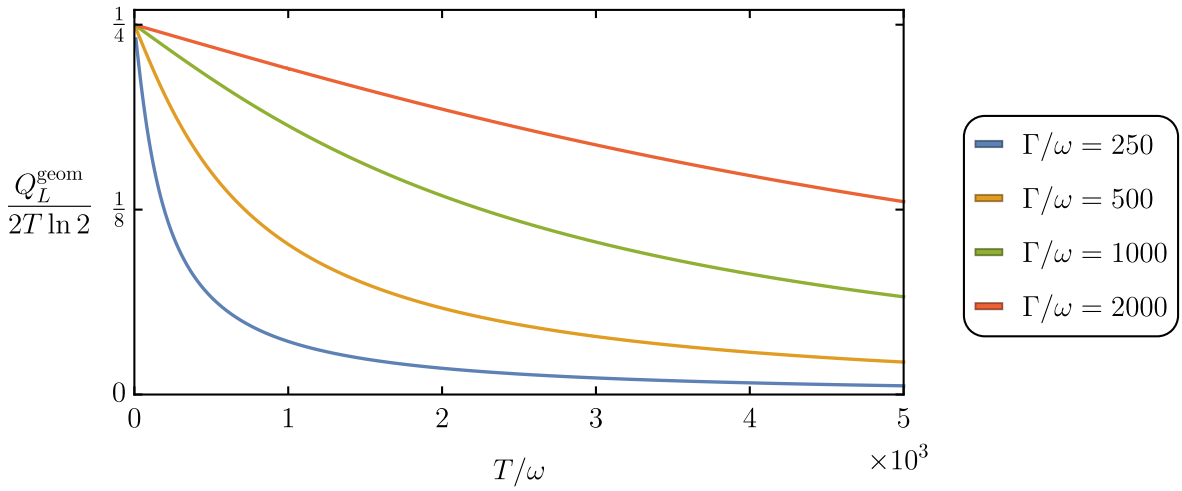


Figure 6.5: The total heat $Q_L$ pumped into the left lead throughout the Majorana braiding process as a function of the lead temperature, in the absence of a temperature bias. Results are shown for a selection of symmetric lead coupling strengths $\Gamma_{L/R} = \Gamma$. When scaled by temperature, we see that this purely geometric heat becomes independent of the coupling strength in the low temperature limit, tending to a universal value.

the parameter space contour corresponding to the braiding can be mapped onto a fixed path in scattering matrix space, independent of the coupling strength to the leads. In this limit, the pumped heat tends to a universal quantized value independent of fluctuations to both the driving and coupling to the leads [57]:

$$\frac{Q}{2T\log 2} = \frac{1}{4}. \tag{6.39}$$

This behaviour is illustrated in Fig. 6.5, which shows the pump heat as a function of temperature for various coupling strengths to the external leads.

As well as this robust quantization in the low temperature limit, the pumped heat provides further signatures of the presence and manipulation of MZMs and allows them to be distinguished from Andreev bound states (ABS) that are known to exhibit similar

transport features in static setups. Specifically, a non-zero pumped heat relies on the fact that the zero energy fermionic state, defined by the MZMs $\gamma_\theta$ and $\gamma_\phi$, is non-local in nature and that the projection of the component MZMs onto the physical Majoranas $\gamma_x$, $\gamma_y$ and $\gamma_z$ can be manipulated. A localized ABS, on the other hand, would exhibit no long range coupling with any other bound state at the opposite end of the wire, as such states would have no connection through the parity operator of the system. Consequently, modulating the flux passing through the Cooper pair boxes, as outlined in Sec. 6.2, will only result in heat pumping in the presence of Majorana excitations.

Furthermore, this driven transport cannot be mimicked by simply varying the coupling strength to the external leads. In this case, any pumping stimulated by, for example, turning off $\Gamma_L$ would be exactly cancelled when $\Gamma_L$ is restored to its original value, which is required to ensure that the driving is periodic. Consequently, pumping a net heat between the leads requires a non-trivial manipulation of the ground state of the internal system.

### 6.3.3 Heat and charge noise from pumping

Our expression for the CGF can further be used to analyse the nature of contributions to the higher order transport cumulants arising from the periodic driving of the system. The inclusion of time dependent processes allows for noise arising not only from thermal fluctuations, but additionally from the non-equilibrium nature of the outgoing scattering states resulting from the possibility of scattering events between nearest energy sidebands. Such events result in correlations between outgoing particle distributions at energies within the range $\epsilon \pm \omega$, which manifest themselves as a source of noise in the average pumped heat and charge. This contribution to the noise is

exclusively present when the system is driven and vanishes in the case that the driving is switched off and inelastic scattering events cease to occur.

Henceforward we will use $\mathcal{M}^{(2)}_{Q_\xi,\mathrm{geom}}$ to denote the part of the driven noise stemming from the geometric CGF $G^{\mathrm{geom}}_{Q_\xi}(\lambda_\xi)$. This is the additional noise appearing when two parameters are driven simultaneously. The noise arising from the remaining part of the pumped CGF, that survives when only a single parameter is driven, we call $\mathcal{M}^{(2)}_{Q_\xi,\mathrm{pump}}$. These driven contributions to the second cumulant of the heat and charge transport are shown in Fig. 6.6 and 6.7 respectively. They highlight the existence of three temperature regimes in which both the heat and charge noise exhibit differing behaviour.

**Low temperature regime:** $T \ll \omega$

In the low temperature regime, the noise associated with the periodic driving dominates over the thermal noise discussed in Sec. 6.3.1. The key quantity dictating the behaviour of the noise in this regime is the difference in Fermi occupation functions between neighboring energy sidebands, $f(\epsilon) - f(\epsilon \pm \omega)$. At low temperature, the energy window over which this quantity is non-zero is centred around $\epsilon = 0$, with a width which scales linearly with $\omega$ and is insensitive to the temperature of the leads.

This lack of temperature dependence can be seen in Figs. 6.6(a,d) and 6.7(a,d) for heat and charge transport respectively. From the insets in each of these panels, it is also clear that this contribution to the noise persists in the limit $T \to 0$, in contrast to the case of thermal noise which vanishes in this limit.

The negligible energy dependence of the real part of the scattering matrix around $\epsilon = 0$ (cf. Fig. 6.3) would suggest that, at low temperatures, this energy dependence

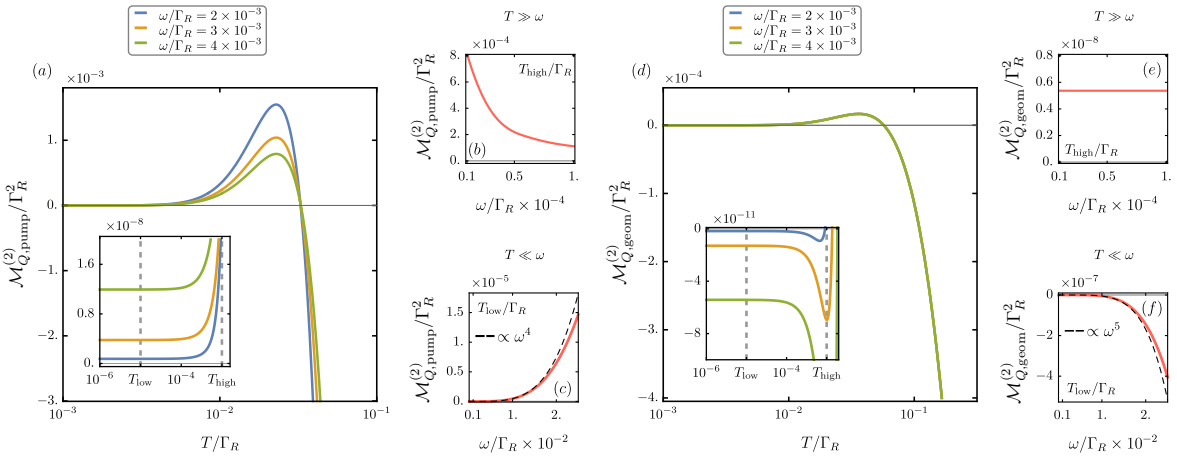


Figure 6.6: The pumped contribution to the second cumulant of the heat transport throughout the driving of a Majorana Y-junction centred at $(\theta_0, \phi_0) = (\pi/2 - 0.1, \pi/4)$, with amplitude $\theta_\omega = \phi_\omega = 0.01$. Plots $(d, e, f)$ show the geometric contribution whereas $(a, b, c)$ illustrate the remaining non-geometric part. Plots $(a, d)$ show the second cumulants as a function of temperature, with the inset highlighting the region $T \ll \omega$. Panels $(b, c, e, f)$ show the same quantities plotted against frequency. $(b, e)$ illustrate the behaviour as a function of low frequencies $\omega < T$ and $(c, f)$ at high frequencies $\omega > T$.

should not influence the transport. However, the linear variation of the imaginary part, along with the behaviour of the scattering matrix derivatives appearing in the inelastic terms $S_{\pm\omega}(\epsilon)$, mean that this factor cannot be neglected, even in this limit. This energy dependence manifests itself in the form of a difference in the frequency dependence between the geometric and non-geometric contributions to the driven noise. Specifically, for heat transport we see, in Fig. 6.6(c,f), that $\mathcal{M}^{(2)}_{Q_\xi,\rm pump} \propto \omega^4$ and $\mathcal{M}^{(2)}_{Q_\xi,\rm geom} \propto \omega^5$ and for charge, in Fig. 6.7(c,f), that $\mathcal{M}^{(2)}_{q_\xi,\rm pump} \propto \omega^2$ and $\mathcal{M}^{(2)}_{q_\xi,\rm geom} \propto \omega^3$. This difference in behaviour between the geometric and non-geometric terms occurs as a result of their differing dependence upon the scattering matrix, as implicit in Eq. 6.14. Furthermore, the difference between the frequency dependence of the charge and heat noise is explained by considering that both are underpinned by the same

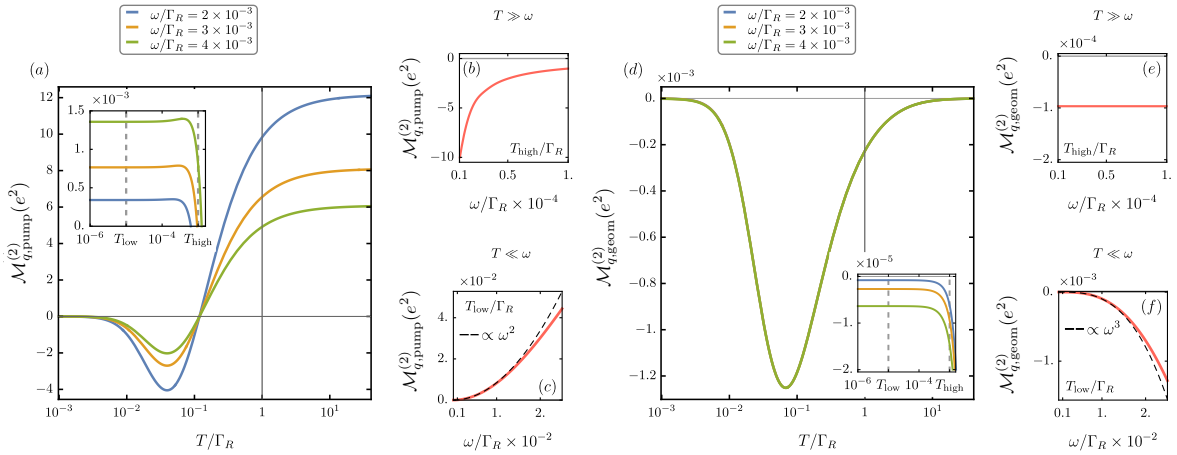


Figure 6.7: The pumped contribution to the second cumulant of the charge transport throughout the driving of a Majorana Y-junction centred at $(\theta_0, \phi_0) = (\pi/2 - 0.1, \pi/4)$ with amplitude $\theta_\omega = \phi_\omega = 0.01$. Plots $(d, e, f)$ show the geometric contribution whereas $(a, b, c)$ illustrate the remaining non-geometric part. Plots $(a, d)$ show the second cumulants as a function of temperature, with the inset highlighting the region $T \ll \omega$. Panels $(b, c, e, f)$ show the same quantities plotted against frequency. $(b, e)$ illustrate the behaviour as a function of low frequencies $\omega < T$ and $(c, f)$ at high frequencies $\omega > T$.

fluctuations and differ only in whether the scattering events are weighted by the energy absorbed/emitted. In the case of scattering between nearest energy sidebands, this energy is given by the driving frequency $\omega$.

**Mid-temperature regime:** $\omega < T \ll \Gamma_{L,R}$

When the temperature of the leads is raised beyond the energy associated with the driving frequency, the temperature takes over as the dominant quantity in determining the size of the energy window within which scattering events can occur. Panels (a) and (d) of Figs. 6.6 and 6.7 illustrate this transition via the deviation of the driven noises away from their corresponding low temperature constant values at approximately $T = \omega$. In this mid-temperature regime, the behaviour is governed by both the distribution

functions $f(\epsilon)$, in addition to the energy dependence of the scattering matrix.

Immediately following the transition into this regime, the heat noise initially varies as $T^5$ whereas the charge noise goes as $T^3$. Here, temperature plays the same role as frequency in the low temperature regime and we have a similar ratio of $T^2$ between the quantities for charge and heat transport. This behaviour is well understood and documented in many previous works [142]. However, as the temperature is increased further it exceeds the width of the narrower resonance present in the scattering matrix elements, set by the location of the driving centre in parameter space $(\theta_0, \phi_0)$ (cf. Fig. 6.3). We see that this results in non-monotonic behaviour of the driven noise, where the turning point is independent of the coupling strength to the leads. This also results in the noise changing sign as the temperature is raised, however we stress that the sum of the static and driven contributions to the noise remain positive at all temperatures. Since the existence of this narrower resonance arises due to the fact that the projection of the zero energy modes in the space of physical Majorans can be controlled, this corresponding behaviour of the noise is unique to our system of interest and indicative of the presence of MZMs.

In terms of frequency dependence, both the heat and charge noise now exhibit the same behaviour. The difference between the non-geometric and geometric contributions, present in the low temperature regime, does persist at higher $T$ as illustrated in panels (b) and (e) respectively. Whereas the non-geometric part is proportional to $1/\omega$, we see that geometric contribution is now independent of the driving frequency similar to the average pumped heat discussed previously. Its geometric nature ensures that $\mathcal{M}^{(2)}_{Q/q_\xi,\mathrm{geom}}$ depends only upon the path traversed in parameter space and not upon the details of the driving itself.

**High temperature regime:** $T > \Gamma_{L,R}$

Increasing the temperature beyond the broadening of the scattering matrix resonance, set by the coupling strength to the external leads, means that the noise is dictated purely by the energy dependence of the scattering matrix. At high energies, both the real and imaginary components of the scattering matrix vary as $1/\epsilon^2$. This results in a saturation of the charge noise and heat noise that is linear in $T$. This behaviour can be seen in panels (a,d) of Figs. 6.6 and 6.7.

**Measuring heat and charge transport**

We end this section with a brief description of how the driven charge and heat transport statistics may be detected in practice. The FCS of electronic transport has long been measurable by use of a quantum point contact capable of detecting single electron tunnelling events and hence counting electrons [189,190]. Repeating this over many time intervals allows the construction of the statistical distribution of the charge transport and subsequently the determination of the average current and noise.

Similar measurements for the case of heat transport can be achieved using quantum calorimetric techniques, by which the energy of individual particles is converted into a measurable temperature change [191–193]. Recent advances in this field have lead to proposals of ultra-sensitive, real-time detection of heat pulses of energy $\lesssim 100\mu$eV [193]. The challenge when working in the low temperature regime is that, as seen in Fig. 6.5, the pumped heat scales linearly with temperature and is therefore small. For our braiding setup we require that the energy scales associated with the temperature and coupling to the external leads are small compared to the superconducting gap, $T, \Gamma \ll \Delta_{\text{sc}}$, with $\Delta_{\text{sc}} \sim 0.2$meV and $\Gamma \sim 0.05$meV examples of typical experimental

parameters [32, 57]. Under these conditions a temperature of $T \sim 20$mK, so that $T/\Gamma \sim 0.04$, would allow access to the low temperature regime in which shot noise dominates. This would lead to a resultant pumped heat of $Q = 0.3\mu$eV per cycle [57], which is below the latest level of achievable sensitivity. Consequently, with the detection schemes currently available, it seems only the higher temperature regime of the heat transport statistics would be accessible in experiments.

## 6.4 Impact of geometric contributions upon fluctuation theorems

Beyond the cumulants associated with charge and heat transport, we can further explore the thermodynamics of driven systems by analysing the nature of fluctuation theorems. In particular, working in the setting of heat transport between two reservoirs, we focus here upon the Gallavotti-Cohen type exchange fluctuation theorem introduced in Sec. 4.2.2 and formulated as

$$\lim_{\tau\to\infty} \frac{1}{\tau} \ln\left[\frac{P_\tau(Q)}{P_\tau(-Q)}\right] = \frac{Q(\beta_R - \beta_L)}{\tau}, \tag{6.40}$$

where $P_\tau(Q)$ denotes the probability distribution of the heat $Q$ transferred from the left to the right bath in some time $\tau$ and $\beta_{L,R} = \frac{1}{k_B T_{L,R}}$. Although this FT is known to hold for non-equilibrium stationary systems, it fails to account for the possibility that heat is exchanged with the source of external driving [61] and previous studies have indicated that it is the geometric contributions to the heat transfer statistics in particular, that result in the need for additional correction terms when making the

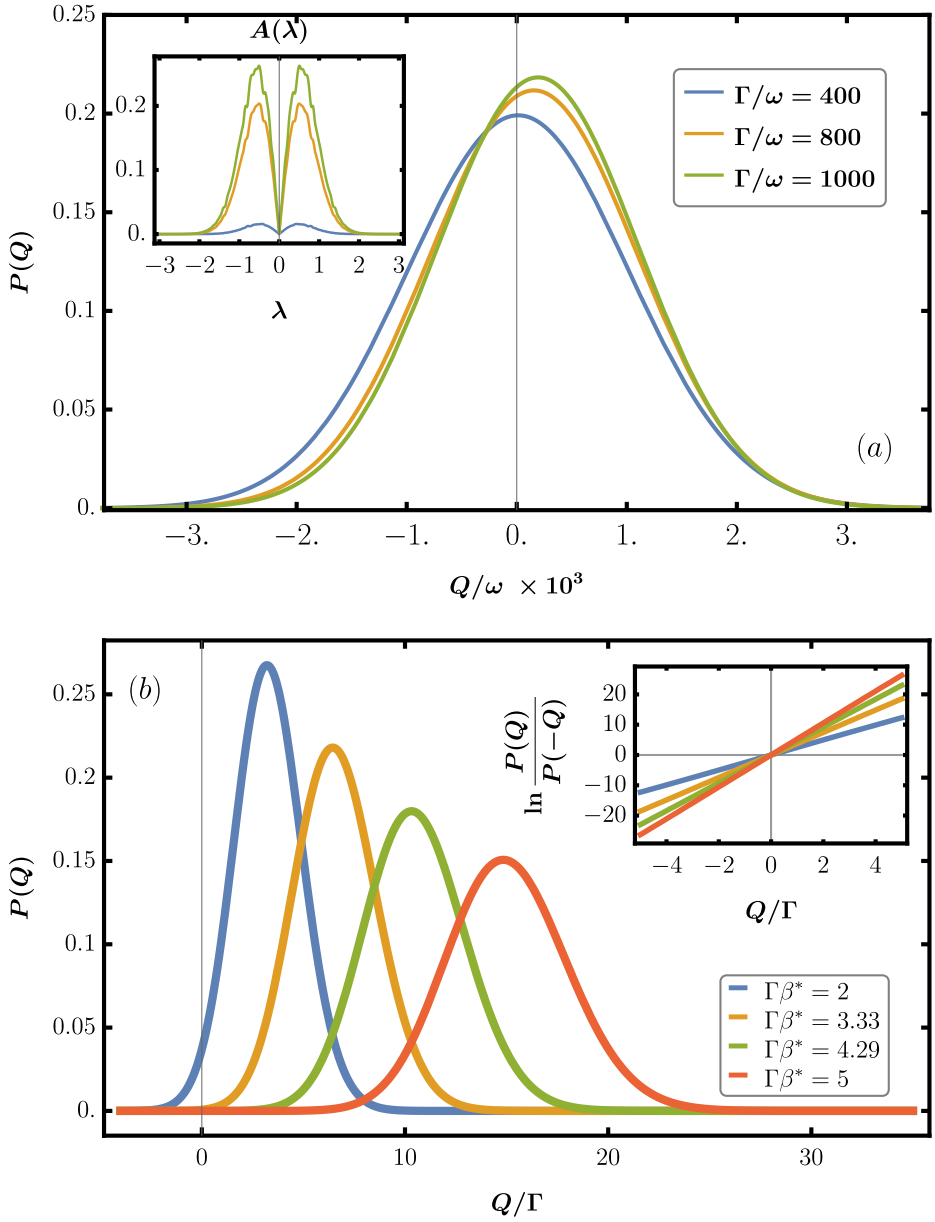


Figure 6.8: (a) Probability distribution, $P(Q)$, for the heat pumped via the small amplitude ($\theta_\omega = \phi_\omega = 0.01$) driving of a Majorana Y-junction centred at $(\theta_0, \phi_0) = (\frac{\pi}{2} - 0.01, \frac{\pi}{4})$. Results are shown for several values of the coupling to the external leads, $\Gamma_L = \Gamma_R = \Gamma$, with an external lead temperature of $T/\omega = 10$. The inset shows the corresponding behaviour of the fluctuation theorem violation quantifier $A(\lambda) = |\chi(\lambda) - \chi(-\lambda)|$ which is identically zero when the Gallavotti-Cohen fluctuation theorem holds true. (b) Probability distribution for the case of a static Majorana Y-junction at $(\theta_0, \phi_0) = (\frac{\pi}{2} - 0.1, \frac{\pi}{4})$. Results are plotted for several temperature gradients, $\beta^\star$ and the inset shows the corresponding behaviour of the fluctuation theorem.

extension to driven systems [58–62]. The formalism presented in this chapter enables the computation of such corrections for systems for which the geometric contributions are topologically protected.

To highlight the fact that it is indeed the cyclic driving of the system that results in the aforementioned correction terms, we first consider the case of a static superconducting Y-junction subjected to a temperature bias between the external leads. Such a system is physically equivalent to a single superconducting nanowire hosting a MZM at each end. The probability distributions $P(Q_L)$ for the heat transport that flows in response to several different temperature gradients $\beta^\star \equiv \beta_R - \beta_L$ are plotted in Fig. 6.8(b). The inset panel demonstrates that, for a static system, the quantity $\ln[P(Q)/P(-Q)]$ corresponds exactly to a straight line of gradient $\beta^\star$, confirming the validity of the GCFT in this scenario.

Returning now to the case of our periodically driven superconducting Y-junction, we first note that the GCFT can be reformulated in terms of the presence of the following symmetry in the characteristic function:

$$\chi_{Q_\xi}(\lambda_\xi) = \chi_{Q_\xi}(-\lambda_\xi + i\beta^\star), \tag{6.41}$$

where $\beta^\star = 0$ for our system of interest, since the temperatures of the external leads are assumed to be equal and remain constant throughout the modulation of the Y-junction. Using this symmetry we can define a function capturing the nature of the corrections to the fluctuation theorem:

$$A(\lambda_\xi) = |\chi_{Q_\xi}(\lambda_\xi) - \chi_{Q_\xi}(-\lambda_\xi)|. \tag{6.42}$$

Therefore, a non-zero value of $A(\lambda_\xi)$ at any value of the counting field, $\lambda_\xi$, indicates the presence of an additional contribution to the GCFT.

For weak amplitude driving of the Y-junction we can calculate the probability distribution for heat transport via the Fourier transform of the exponentiated total CGF $G_{Q_\xi}(\lambda_\xi)$ defined in Eq. 6.15. The probability distributions associated with one such cycle are plotted in Fig. 6.8(a), for several values of $\Gamma$. Despite the absence of any temperature or chemical potential gradients between the leads, we see that heat is pumped across the system throughout the cycle and is indicated by the asymmetry of $P(Q)$ with respect to $Q = 0$. The inset in panel (a) illustrates the behaviour of the function $A(\lambda_\xi)$, which is non-zero around $\lambda = 0$ and hence indicative of a correction to the FT.

The behaviour of $A(\lambda_\xi)$ also suggests that the magnitude of the correction term is increasing with the coupling strength to the external leads $\Gamma$. This is a consequence of the increasing translation of $P(Q)$ away from $Q = 0$, as an increasing heat current is pumped across the system. However, increasing noise at higher temperatures will act to obscure any translation of $P(Q)$ and hence decrease the magnitude of the correction term. Despite the fact that at low temperatures the variance of $P(Q)$ is found to decrease with increasing coupling strength (cf. Fig. 6.6(a) inset), in the high temperature regime the static component of the noise becomes linearly dependent upon $\Gamma$ and dominates over the driven contributions in this limit.

### 6.4.1 Extension to arbitrary amplitude pumps

In this section, we illustrate that our results for the correction term of the GCFT can be extended to include large amplitude driving cycles and hence applied to our example of

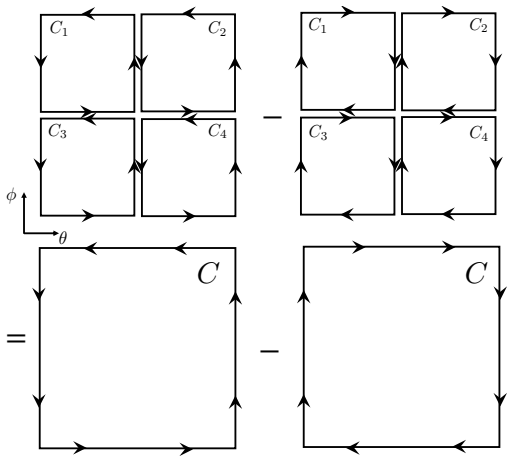


Figure 6.9: An illustration of how the difference between contour integrals in opposite directions for arbitrary amplitude cycles can be broken down into the sum of similar differences on smaller cycles. This result is due to the cancellation of the integrals along the interior sides of the smaller cycles and is valid upon division of the contour $C$ into an arbitrary number of smaller cycles $\{C_i\}$.

a Majorana braiding cycle. Central to this extension is the fact that the total CGF for an arbitrary small amplitude cycle can be written as a sum of geometric and dynamical contributions: $G_{Q_\xi}(\lambda_\xi) = G^{\text{geom}}_{Q_\xi}(\lambda_\xi) + G^{\text{dyn}}_{Q_\xi}(\lambda_\xi)$. Here, the dynamical component contains both the static contributions and the part of the driven contributions that is not geometric in nature. Our numerical simulations show the dynamical part of the GCF obeys the GC symmetry for all $\lambda$ and hence any correction term in the FT arises solely from geometric contributions. Using this fact, an equivalent indicator of FT corrections can be defined as

$$A^{\text{geom}}(\lambda_\xi) = |\chi^{\text{geom}}_{Q_\xi}(\lambda_\xi) - \chi^{\text{geom}}_{Q_\xi}(-\lambda_\xi)|, \tag{6.43}$$

where $\chi^{\text{geom}}_{Q_\xi}(\lambda_\xi) = \exp\left(G^{\text{geom}}_{Q_\xi}(\lambda_\xi)\right)$. This quantity, in contrast to $A(\lambda_\xi)$, can be calculated for arbitrary amplitude driving cycles.

To see the validity of this extension, it is useful to notice that the generating function is dependent upon the direction in which we traverse the contour in parameter space induced by the driving. We denote the clockwise and counter-clockwise CGFs as $G^{\circlearrowleft}_{Q_\xi}(\lambda_\xi)$ and $G^{\circlearrowright}_{Q_\xi}(\lambda_\xi)$ respectively. The difference between these two functions, $D_{Q_\xi}(\lambda_\xi) = G^{\circlearrowleft}_{Q_\xi}(\lambda_\xi) - G^{\circlearrowright}_{Q_\xi}(\lambda_\xi)$, will clearly change sign under time reversal. This allows the calculation of this quantity for a large amplitude cycle by breaking down the area enclosed by the contour in parameter space into smaller segments, within which the weak amplitude approximation is valid. This reasoning is sketched in Fig. 6.9. We can write each of the directional generating functions for each small cycle as closed contour integrals in the parameter space as $G^{\circlearrowleft}_{Q_\xi}(\lambda_\xi) = \oint_C ds \frac{dt}{ds} G_{Q_\xi}(\lambda_\xi, \theta, \phi)$. The subtraction of this integral along contours with opposing orientation results in the cancellation of the interior contributions, leaving only the desired line integral around the boundary of the larger cycle:

$$\begin{aligned} D_{Q_\xi}(\lambda_\xi) &= \int_0^{\mathcal{T}} dt \big( G^{\circlearrowleft}_{Q_\xi}(\lambda_\xi, t) - G^{\circlearrowright}_{Q_\xi}(\lambda_\xi, t) \big) \\ &= \oint_C ds \frac{dt}{ds} G_{Q_\xi}(\lambda_\xi, \theta, \phi) - \oint_C ds \frac{dt}{ds} G_{Q_\xi}(\lambda_\xi, \theta, \phi) \\ &= \sum_i \left[ \oint_{C_i} ds_i \frac{dt}{ds_i} G_{Q_\xi}(\lambda_\xi, \theta, \phi) - \oint_{C_i} ds_i \frac{dt}{ds_i} G_{Q_\xi}(\lambda_\xi, \theta, \phi) \right]. \end{aligned} \tag{6.44}$$

In this way, we can obtain the quantity $D_{Q_\xi}(\lambda_\xi)$ for arbitrary amplitude cycles by summing the contributions from cycles in which the small amplitude approximation is valid. Taking the limit of infinitesimally small interior cycles, this technique can be used to determine $D_{Q_\xi}(\lambda_\xi)$ for contours of arbitrary shape and size via the integration over the area enclosed by the contour. The quantity $D_{Q_\xi}(\lambda_\xi)$ isolates the contribution to the CGF that is sensitive to pumping direction and hence, for a small amplitude,

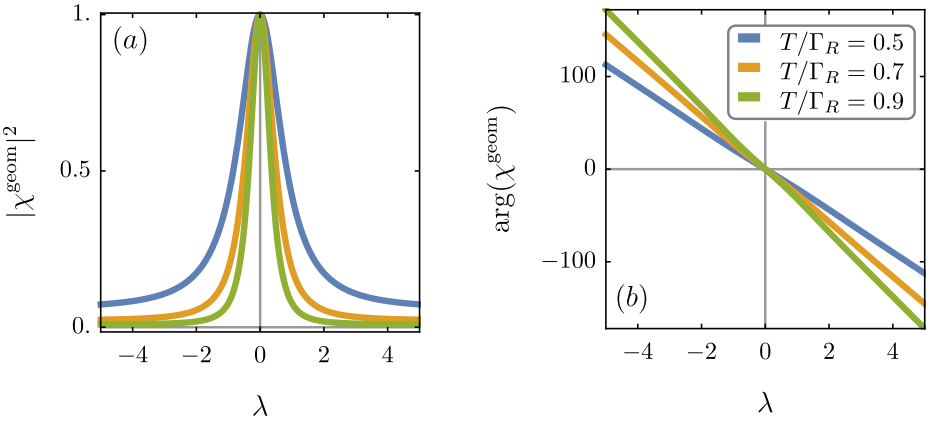


Figure 6.10: Absolute value (a) and argument (b) of the geometric contribution to the heat transport characteristic function $\chi^{\text{geom}}(\lambda)$ for the case of a Majorana braiding protocol. Results are plotted for several values of the external lead temperature. Asymmetry of this function in $\lambda$ indicates an apparent violation of the Gallavotti-Cohen type fluctuation theorem.

two parameter pump, this quantity corresponds exactly to $2G^{\text{geom}}_{Q_\xi}(\lambda_\xi)$. This therefore enables the calculation of the FT correction function $A^{\text{geom}}(\lambda_\xi)$ for arbitrary amplitude driving cycles.

We plot the absolute value and argument of the geometric contribution to the CF, $\chi^{\text{geom}}_{Q_\xi}(\lambda_\xi)$, for a Majorana braiding process in Figs. 6.10(a) and (b) respectively. From this one can deduce that, although the real part fulfills the GC symmetry, this symmetry is not present in the imaginary component of the CF, which is found to be antisymmetric around $\lambda_\xi = 0$. Consequently, the correction function, in this example, can be written as

$$A^{\text{geom}}(\lambda_\xi) = 2\left|\chi^{\text{geom}}_{Q_\xi}(\lambda)\sin\left(\arg(\chi^{\text{geom}}_{Q_\xi}(\lambda_\xi))\right)\right|. \tag{6.45}$$

In the case of a Majorana braiding, this non-zero correction to the GCFT stems solely from the cyclic variation of the system's internal parameters in the form of a non-trivial rotation of the degenerate ground-space. The lack of requirement for modulation of the

properties of the external leads and the energy level of the internal system, along with the fact that the ground state facilitating the transport is degenerate, makes this system distinct from those appearing in previous studies of topologically trivial systems that highlight the existence of the same correction term [58, 188]. In the Y-junction setup the relevant driving parameters, which appear in geometric transport properties, are not the physical parameters (the magnetic flux passing through the Cooper pair boxes) that would be driven if the process was carried out experimentally. In the case of the braiding operation, this allows for the possibility that the contour appearing in the geometric contribution to the FCS, and consequently in the FT correction term, is immune to fluctuations in the value of the driving parameters in addition to the driving frequency for $T \gg \omega$.

We can also briefly comment on the temperature dependence of the correction term by noting that two competing factors must be taken into account. Although the pumped heat increases as a function of $T$, illustrated by the increasing gradient of $\arg\left(\chi^{\text{geom}}_{Q_\xi}(\lambda_\xi)\right)$ in Fig. 6.10(b), we also know that the second cumulant of the pumped heat, $\mathcal{M}^{(2)}_{Q_\xi}$ varies as $T^5$. This increased variance, indicated by the rate of decay of $|\chi^{\text{geom}}_{Q_\xi}(\lambda_\xi)|^2$ plotted in Fig. 6.10(a), leads to the overlap of the probability distributions $P(Q)$ and $P(-Q)$ and hence a reduction in the correction to the GCFT.

## 6.5 Discussion

A system driven in an periodic cycle shows corrections to thermodynamic fluctuation theorems which depend on geometric properties of the cycle, as opposed to its dynamical features. Here we have studied the statistics of heat transfer for slowly driven cycles associated with the topologically protected evolution of a quantum system, specifically,

an exchange of Majorana excitations present in 1D superconducting nanowires. We have first obtained general expressions for the statistics of heat transfer from scattering matrices, which extend known results for the charge transport full counting statistics. This approach was then utilized to highlight features unique to the presence of Majorana zero modes in the heat and charge current noise and additionally analyse the nature of the Gallavotti-Cohen type exchange fluctuation theorem for this driven system.

We have successfully demonstrated that our initial approach, based upon the approximation of weak amplitude driving, can be extended to explore the geometric transport features of arbitrary amplitude cycles and showed that the heat transfer associated with Majorana braiding induces a correction to a Gallavotti-Cohen type fluctuation theorem. As opposed to analogous corrections in non-topological systems, which require cyclical variation of the external lead properties, coupling strengths to the leads or energy level of the internal system [58, 188], our contribution stems solely from a cycle in the system's parameter space, at constant temperature gradient, and is a result of the coherent dynamics of the driven degenerate ground state of the internal system. Moreover, in the limit of slow driving, this correction term is purely geometric in nature and hence inherits the topological protection of the braiding operation against small, slow fluctuations of the driving.

Since it relies upon the non-local nature of the fermionic mode defined by the MZMs, the analysis of the heat transport could potentially provide an invaluable alternative to charge transport signatures of topological excitations, that are difficult to discriminate from other features of the system such as localized Andreev bound states [37, 38]. The quantized nature of the pumped heat further provides a signature of the execution of a non-trivial manipulation of the zero modes themselves. Finally,

the identification of corrections to transport fluctuation theorems, in terms of quantum coherent contributions to scattering processes, allows for further investigation to incorporate such contributions in properly modified fluctuation theorems.

# Chapter 7

# Majorana Y-junction as a Heat Engine

As demonstrated in Chap. 6, the manipulation of Majorana zero-modes within a superconducting nanowire Y-junction results in the pumping of heat between coupled fermionic reservoirs. This setup therefore resembles the behaviour of a thermal machine operating via a genuinely quantum cycle by which, depending on the initial parameters, the manipulation of a working substance can be used to transform heat into useful work or use work to pump heat from cold to hot reservoirs resulting in refrigeration [63–66]. Since the topologically protected nature of the Majorana braiding protocol results in a highly controlled contribution to the driven heat current [57], it is interesting to explore the thermodynamic properties of this process and assess the Y-junction's performance as a geometric thermal machine. The content of this chapter is based upon preliminary, as yet unpublished, results.

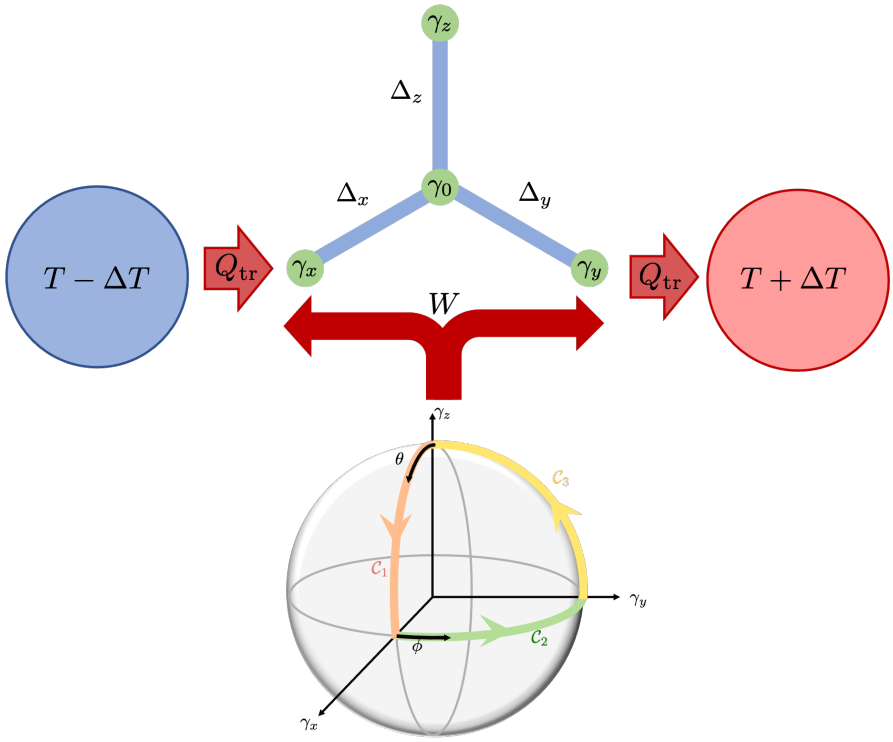


Figure 7.1: Schematic of a Majorana braiding driven thermal machine. The superconducting Y-junction introduced in Sec. 6.2 is coupled to hot and cold fermionic reservoirs with a temperature bias of $\Delta T$. The execution of the braiding cycle, in addition to the temperature gradient, stimulates the flow of heat $Q_{\rm tr}$ between the reservoirs. The work done $W$ by the driving also results in an additional flow of heat into the system.

## 7.1 Model of the Y-junction as a thermal machine

We are interested in determining the thermodynamic performance of the driven Majorana Y-junction as a working substance in a quantum thermal machine. As such, we consider the scenario sketched in Fig. 7.1, in which the Y-junction is coupled to two external metal leads now held at different temperatures $T_L = T - \Delta T$ and $T_R = T + \Delta T$. Apart from the coupling to the leads, the Y-junction is considered closed so that energy is only exchanged with the source of driving and dissipated into the leads. We will

again be concerned with the slow driving regime introduced in the previous chapter. Additionally, we are interested in the case for which the temperature gradient $\Delta T$ is small enough so that the heat that flows as a result of this bias is comparable to the heat flow induced by the Majorana braiding protocol. In this regime, under the right conditions, it will be possible to realise the case for which a net heat current flows from the cold to the hot reservoirs and hence refrigeration occurs.

### 7.1.1 Heat, work and entropy production

In addition to the heat transport induced between external reservoirs by both the temperature gradient and adiabatic modulation of the internal system, the driving is itself a source of heating that results in dissipation in the leads [63, 130, 206]. Together these contributions make up the total heat flux $Q_\alpha$ entering each lead $\alpha$ after a single driving period

$$Q_\alpha = E_\alpha - \mu_\alpha N_\alpha, \tag{7.1}$$

with $Q_\alpha$ and $N_\alpha$ the energy and particle fluxes entering the lead $\alpha$ respectively. In order to focus solely on energy currents, throughout the following we will set $\mu_\alpha = 0 \; \forall \; \alpha$. In the case of a setup involving just two external leads, the component of the heat arising due to transport $Q_{\mathrm{tr},\alpha}$ will necessarily satisfy the condition

$$Q_{\mathrm{tr},L} = -Q_{\mathrm{tr},R} \equiv Q_{\mathrm{tr}}. \tag{7.2}$$

The additional work performed by the parameter driving can therefore be isolated as the additional heat generated by the driving

$$W = Q_L + Q_R. \tag{7.3}$$

It is also interesting to consider the entropy current induced by the driving of such a thermal machine. This is defined as the sum of the entropy production in each of the leads throughout the process:

$$S = \frac{Q_L}{T_L} + \frac{Q_R}{T_R}. \tag{7.4}$$

Expanding to first order in the temperature bias $\Delta T$ this can be expressed as the sum of two distinct contributions [206]:

$$ST \approx Q_L + Q_R + \frac{(Q_R - Q_L)\Delta T}{T} = W + \frac{Q_{\mathrm{tr}}\Delta T}{T}. \tag{7.5}$$

Here the first term corresponds to the work done by the driving forces, whereas the second term describes the work required to drive the $Q_{\mathrm{tr}}$ against the thermal bias $\Delta T$.

### 7.1.2 Efficiencies

Depending upon the direction of heat transport between the hot and cold reservoirs, the driven Majorana Y-junction has the potential to operate as either a heat engine or a refrigerator. In the case that heat is transported from the hot to cold reservoir, the resultant change in free energy can be used to perform useful work upon the source of

the driving. The efficiency of such a heat engine can be defined as

$$\eta^{\mathrm{he}} = \frac{-W}{Q_{\mathrm{tr}}}, \tag{7.6}$$

the value of which is bounded by the Carnot efficiency $\eta_C^{\mathrm{he}} = \Delta T/T$.

Refrigeration occurs in the case that the work done by the external driving force is used to pump heat from the cold to the hot reservoir. The corresponding efficiency quantifier, often referred to as the coefficient of performance (COP), is given by

$$\eta^{\mathrm{fr}} = \frac{-Q_{\mathrm{tr}}}{W}, \tag{7.7}$$

where positive $Q_{\mathrm{tr}}$ is defined so as to describe heat flowing in the direction of the thermal gradient. This quantity is bounded by the reciprocal of the Carnot efficiency for the heat engine: $\eta_C^{\mathrm{fr}} = T/\Delta T$.

Additionally, the driven Y-junction can be used as a heat pump, even in the absence of a temperature gradient between the leads, as discussed in Chap. 6. In this case the heat can be pumped in either direction and the only source of dissipation arises from the modulation of the parameters $\{X_j\}$. As such, the efficiency of this process is defined by the unbounded quantity

$$\eta^{\mathrm{hp}} = \frac{|Q_{\mathrm{tr}}|}{W}. \tag{7.8}$$

As demonstrated in Chap. 6, in the slow driving limit the only contribution to the heat flux entering each lead is that of the driven contribution $Q_{\mathrm{tr}}$ and hence the efficiency of such a pump will continue to increase as the driving frequency $\omega \to 0$.

## 7.2 Determining the heat current using the scattering matrix formalism

In order to include the effect of thermal dissipation, and hence analyse the efficiency of the Y-junction as a thermal machine, it is necessary to include contributions of $\mathcal{O}(\omega^2)$ and hence make use of the first order expansion of the Floquet scattering matrix introduced in Eq. 3.34. In the following derivation we mostly follow the method outlined in [207]. The heat current flowing in the lead $\alpha$ is defined as

$$I_\alpha^Q = \langle \hat{I}_\alpha^{Q,\text{in}}(t) - \hat{I}_\alpha^{Q,\text{out}}(t) \rangle, \tag{7.9}$$

using the ingoing (outgoing) heat current operators $\hat{I}_\alpha^{Q,\text{in}}$ ($\hat{I}_\alpha^{Q,\text{out}}$) defined in Eq. 3.7. The heat current operators can equally be reformulated as

$$\begin{aligned} \langle \hat{I}_\alpha^{\text{in}}(t) \rangle &= \int_{-\infty}^{\infty} d\epsilon \epsilon \phi_{\alpha,\alpha}^{\text{in}}(t,\epsilon), \\ \langle \hat{I}_\alpha^{\text{out}}(t) \rangle &= \int_{-\infty}^{\infty} d\epsilon \epsilon \phi_{\alpha,\alpha}^{\text{out}}(t,\epsilon), \end{aligned} \tag{7.10}$$

with $\phi^{\text{in/out}}(t,\epsilon)$ given by the Wigner transformation of the relevant expectation values:

$$\begin{aligned} \phi_{\alpha\beta}^{\text{in}}(t,\epsilon) &= \int_{-\infty}^{\infty} d\tilde{\epsilon}\ \epsilon e^{i\tilde{\epsilon}t/h} \left\langle a_\beta^\dagger\Big(\epsilon + \frac{\tilde{\epsilon}}{2}\Big) a_\alpha\Big(\epsilon - \frac{\tilde{\epsilon}}{2}\Big) \right\rangle \\ \phi_{\alpha\beta}^{\text{out}}(t,\epsilon) &= \int_{-\infty}^{\infty} d\tilde{\epsilon}\ \epsilon e^{i\tilde{\epsilon}t/h} \left\langle b_\beta^\dagger\Big(\epsilon + \frac{\tilde{\epsilon}}{2}\Big) b_\alpha\Big(\epsilon - \frac{\tilde{\epsilon}}{2}\Big) \right\rangle. \end{aligned} \tag{7.11}$$

Using the fact that the outgoing particle operators can be expressed in terms of the two-energy dependent scattering matrix as $b^\dagger(\epsilon_1) = \int d\epsilon_2 S(\epsilon_1,\epsilon_2) a^\dagger(\epsilon_2)$ along with the

expectation values of uncorrelated ingoing channels given in Eq. 3.8, we have that

$$\langle b^{\dagger}_{\beta}(\epsilon_2) b_{\alpha}(\epsilon_1)\rangle = \sum_{\gamma} \iint d\epsilon_3 d\epsilon_4 S_{\alpha,\gamma}(\epsilon_1,\epsilon_3)\delta(\epsilon_3-\epsilon_4) f_{\gamma}(\epsilon_4) S^{\dagger}_{\gamma,\delta}(\epsilon_4,\epsilon_2). \tag{7.12}$$

In order to determine $\phi^{\text{out}}_{\alpha}(t,\epsilon)$ in terms of the scattering matrix, we note that taking the Wigner transform of a convolution of the form

$$G(\epsilon_1,\epsilon_2) = \int d\epsilon_3 C(\epsilon_1,\epsilon_3) D(\epsilon_3,\epsilon_2), \tag{7.13}$$

results in a Moyal product of Wigner transforms

$$G(\epsilon,t) = C(\epsilon,t) * D(\epsilon,t), \tag{7.14}$$

where $C(\epsilon,t) * D(\epsilon,t) = C(\epsilon,t)\exp\Big(\frac{i}{2}\big(\overleftarrow{\partial}_{\epsilon}\overrightarrow{\partial}_{t} - \overleftarrow{\partial}_{t}\overrightarrow{\partial}_{\epsilon}\big)\Big) D(\epsilon,t)$. Consequently, the Wigner transform of the expectation value in Eq. 7.12 can be expressed as

$$\phi^{\text{out}}_{\alpha\beta}(t,\epsilon) = \sum_{\gamma}\big[\mathcal{S}_{\alpha\gamma}(\epsilon,t) * f_{\gamma}(\epsilon)\big] * \mathcal{S}^{\dagger}_{\gamma\beta}(\epsilon,t), \tag{7.15}$$

with the Wigner transform of the full scattering matrix given by

$$\mathcal{S}(\epsilon,t) = \int d\tilde{\epsilon} e^{-i\tilde{\epsilon}t} S\Big(\epsilon+\frac{\tilde{\epsilon}}{2}, \epsilon-\frac{\tilde{\epsilon}}{2}\Big). \tag{7.16}$$

As in the previous chapters of this thesis, we are concerned with scattering events via some internal system modelled by the periodic Hamiltonian $H_0(t)$, with time dependence induced through the modulation of some set of internal parameters $\{X_j(t)\}$. As outlined in Sec. 3.2.1, in the event that the parameter variation is slow enough,

the Wigner transformed scattering matrix $\mathcal{S}(\epsilon, t)$ can be expanded about the frozen scattering matrix $S(\epsilon, t)$ in powers of the velocities $\dot{X}_j$, up to terms of order $\omega^2$ [207,208]:

$$\mathcal{S}(\epsilon, t) \approx S(\epsilon, t) + \sum_j \dot{X}_j A_j(\epsilon, t) + \sum_{ij} \dot{X}_i \dot{X}_j B_{ij}(\epsilon, t) + \sum_j \ddot{X}_j C_j(\epsilon, t). \tag{7.17}$$

As first introduced in Eq. 6.30, the frozen scattering matrix can be expressed in the form

$$S(\epsilon, t) = 1 + 2\pi i W^\dagger G^R(\epsilon, t) W, \tag{7.18}$$

with the frozen retarded Green's function of the internal system given by $G^R(\epsilon, t) = (H_0(t) - \epsilon - i\pi W W^\dagger)$. It can be demonstrated, by term by term comparison with the expansion of the full retarded Green's function $\mathcal{G}^R$, that the matrices $A_j$, encoding the first order corrections to the frozen scattering matrix, can be calculated as [208]

$$A_j(\epsilon, t) = \pi W^\dagger \left( \frac{\partial G^R}{\partial \epsilon} \frac{\partial H_0}{\partial X_j} G^R - G^R \frac{\partial H_0}{\partial X_j} \frac{\partial G^R}{\partial \epsilon} \right) W. \tag{7.19}$$

The matrices $B_{ij}(\epsilon, t)$ and $C_j(\epsilon, t)$ will make no contribution to the forthcoming expansion of the outgoing operator $\phi^{\text{out}}$ after accounting for the condition of unitarity imposed upon the full scattering matrix $\mathcal{S}(\epsilon, t)$, as outlined in Appendix C [207].

Using the adiabatic approximation of the scattering matrix (Eq. 7.17) to evaluate the Moyal product from Eq. 7.15, gives rise to a corresponding expansion of $\phi^{\text{out}}$ in powers of the parameter driving velocity:

$$\phi^{\text{out}} \approx \phi^{\text{out}(0)} + \phi^{\text{out}(1)} + \phi^{\text{out}(2)}. \tag{7.20}$$

In the following we examine the nature of each term in this expansion individually.

## Zeroth order

The zeroth order contribution comes from the frozen scattering matrix only:

$$\phi_{\alpha\beta}^{\mathrm{out}(0)} = \sum_{\gamma} S_{\alpha\gamma} f_{\gamma} S_{\gamma\beta}^{\dagger}. \tag{7.21}$$

The contribution to the heat current $I^Q$ arising from this zeroth order term corresponds to the heat that flows due to any temperature or chemical potential bias between the external leads. Considering terms up to second order in the temperature bias $\Delta T$ this leads to a contribution to the transported heat $Q_{\mathrm{tr}}$ of the form

$$Q_{\mathrm{tr}}^{\mathrm{grad}} = \int_0^{\mathcal{T}} dt \int_{-\infty}^{\infty} d\epsilon \epsilon^2 \frac{\Delta T}{T} \frac{\partial f(\epsilon)}{\partial \epsilon} |S_{LR}(\epsilon, t)|^2. \tag{7.22}$$

Unlike the geometric nature of the contribution to the transported heat arising directly from the driving, this contribution corresponds to the direct heat flow from the hot to the cold reservoir and acts against the efficiency of the machine as a refrigerator. Since this heat current is time-independent, it becomes particularly harmful to the efficiency in the limit of slow driving.

## First order

The first order contribution to the outgoing operator is expanded as [207]

$$\begin{aligned} \phi_{\alpha\beta}^{\mathrm{out}(1)} = \Bigg[ A\rho S^{\dagger} + S\rho A^{\dagger} + \frac{i}{2}\Big(\frac{\partial S}{\partial \epsilon}\rho\frac{\partial S^{\dagger}}{\partial t} - \frac{\partial S}{\partial t}\rho\frac{\partial S^{\dagger}}{\partial \epsilon}\Big) \\ + \frac{i}{2}\Big(S\frac{\partial \rho}{\partial \epsilon}\frac{\partial S^{\dagger}}{\partial t} - \frac{\partial S}{\partial t}\frac{\partial \rho}{\partial \epsilon}S^{\dagger}\Big)\Bigg]_{\alpha\beta}, \end{aligned} \tag{7.23}$$

with $\rho_{\alpha\beta}(\epsilon) = f_\alpha(\epsilon)\delta_{\alpha\beta}$ a diagonal matrix whose elements correspond to the distribution function of each scattering channel and $A(\epsilon, t) = \sum_j \dot{X}_j A_j(\epsilon, t)$. In the absence of a temperature difference between the leads, so that $f_\alpha(\epsilon) = f(\epsilon)\ \forall\ \alpha$, this contribution reduces to the heat current pumped between the left and right leads as investigated in Chap. 6:

$$\begin{aligned} Q_{\mathrm{tr}}^{\mathrm{pump}} &= \int_0^{\mathcal{T}} dt \int_{-\infty}^{\infty} d\epsilon \epsilon \frac{\partial f(\epsilon)}{\partial \epsilon} \sum_\beta \mathrm{Im}\left[S_{L\beta}\frac{\partial S_{L\beta}^*}{\partial t}\right] \\ &= \int_{-\infty}^{\infty} d\epsilon \epsilon \frac{\partial f(\epsilon)}{\partial \epsilon} \oint \sum_{j,\beta} dX_j\, \mathrm{Im}\left[S_{L\beta}\frac{\partial S_{L\beta}^*}{\partial X_j}\right]. \end{aligned} \tag{7.24}$$

In this form, this contribution to the transported heat is manifestly geometric in nature and hence only depends upon the path traversed in parameter space throughout the driving cycle.

The remaining component of the heat flux, arising from the first order term of the outgoing operator $\phi^{\mathrm{out}(1)}$, contributes to the work done by the driving forces through the cycle. This contribution to the work is also geometric and up to second order in the small parameters $X_j$ and $\Delta T$ can be expressed as

$$\begin{aligned} W^{\mathrm{geom}} &= \sum_j \int_{-\infty}^{\infty} d\epsilon \oint dX_j \Lambda_j \frac{\Delta T}{T}, \\ \text{with}\quad \Lambda_j &= \frac{\partial f(\epsilon)}{\partial \epsilon}\Big(2\epsilon^2\,\mathrm{Re}[A_j\sigma_z S^\dagger] + \epsilon^2\,\mathrm{Im}\Big[\frac{\partial S}{\partial \epsilon}\sigma_z\frac{\partial S^\dagger}{\partial X_j}\Big] + \epsilon\,\mathrm{Im}\Big[S\sigma_z\frac{\partial S^\dagger}{\partial X_j}\Big]\Big) \\ &\quad + \epsilon^2\frac{\partial^2 f(\epsilon)}{\partial \epsilon^2}\,\mathrm{Im}\Big[S\sigma_z\frac{\partial S^\dagger}{\partial X_j}\Big]. \end{aligned} \tag{7.25}$$

Here $\sigma_z$ is the Pauli z-matrix acting in the basis of the left and right leads. This geometric contribution corresponds exactly to work required to overcome the thermal bias and pump the heat $Q_{\mathrm{tr}}^{\mathrm{pump}}$ from the cold to the hot reservoir.

### Second order

Since we are interested in studying systems for which the temperature gradient between the leads is small, we only include the terms that are second order in the parameter velocity that arise in the absence of a temperature difference between the external leads. Using Eq. C.6 in Appendix C, this contribution then simplifies to [207]

$$\phi_{\alpha\beta}^{\mathrm{out}(2)} = \frac{1}{2}\frac{\partial^2 f}{\partial \epsilon^2}\left[\frac{\partial S}{\partial t}\frac{\partial S^\dagger}{\partial t}\right]_{\alpha\beta} + \frac{i}{2}\frac{\partial f}{\partial \epsilon}\left[A\frac{\partial S^\dagger}{\partial t} + S\frac{\partial A^\dagger}{\partial t} + \frac{i}{2}\left(\frac{\partial^2 S}{\partial t^2}\frac{\partial S^\dagger}{\partial \epsilon} + \frac{\partial S}{\partial \epsilon}\frac{\partial^2 S^\dagger}{\partial t^2} - \frac{\partial^2 S}{\partial \epsilon \partial t}\frac{\partial S^\dagger}{\partial t} - \frac{\partial S}{\partial t}\frac{\partial^2 S^\dagger}{\partial \epsilon \partial t}\right)\right]_{\alpha\beta}. \tag{7.26}$$

This contribution results in a strictly positive heat flux flowing from the driven scatterer into each of the external leads and hence constitutes a dissipative component of the total work done by the driving forces $W$. This term is not geometric in nature and increases with the driving frequency $\omega$, as will be demonstrated numerically in the results that follow.

The expressions derived in this section allow for the determination of the heat current $I_\alpha^Q(t)$ flowing in the lead $\alpha$, up to second order in the velocity of the driven Hamiltonian parameters $X_j(t)$. These will now be utilized to analyse the efficiency of driven Majorana Y-junction as a quantum thermal machine.

## 7.3 Results

We start by considering the scenario for which the braiding process pumps heat in the absence of a temperature gradient between the external reservoirs. In Fig. 7.2(a) we plot both the purely geometric pumped heat $Q_{\mathrm{tr}}$, alongside the work performed by the

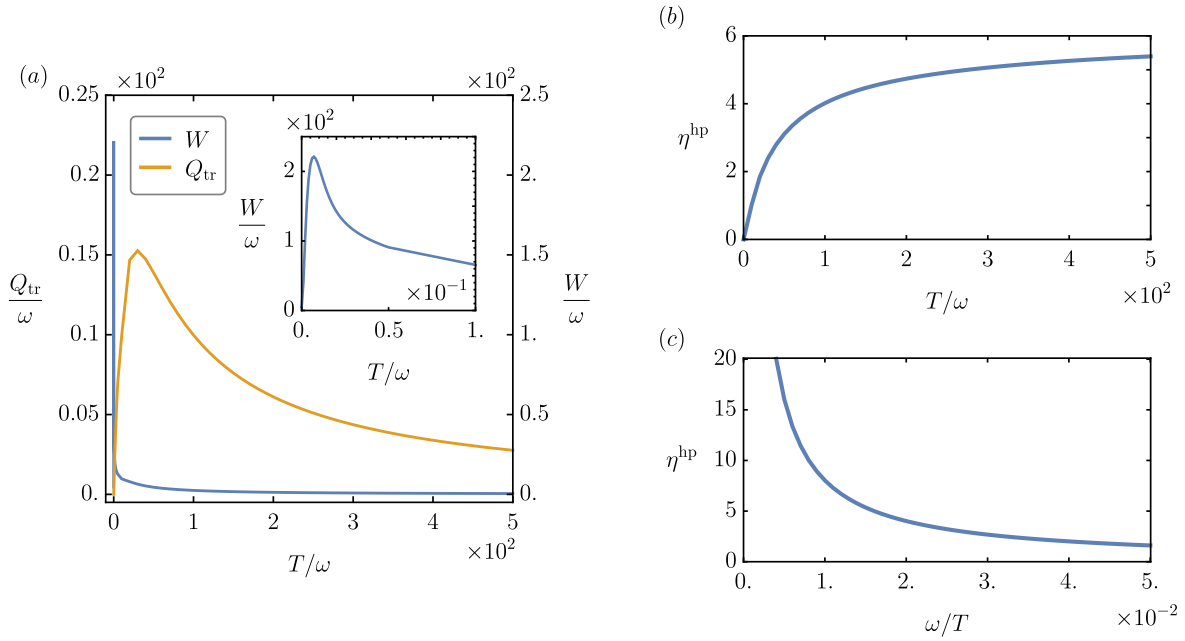


Figure 7.2: (a) Pumped heat $Q_{\mathrm{tr}}$ and work done by the driving $W$ as a function of lead temperature for a Majorana braiding exchange in the absence of a temperature gradient, $\Delta T = 0$. The inset gives a closer view of the behaviour of $W$ at low temperatures. We used a coupling strength to the external leads of $\Gamma_L = \Gamma_R = 0.01T$ and a driving frequency of $\omega = 0.02T$. (b) Using the same system parameters, we plot the behaviour of the coefficient of performance $\eta^{\mathrm{hp}}$ versus $T$. (c) The coefficient of performance is plotted as a function of driving frequency. The COP is unbounded in the slow driving limit as the heat dissipated by the driving tends to zero and the geometric pumped heat remains unchanged.

driving $W$ as a function of the lead temperature $T$. We see that, for all temperatures, $Q_{\mathrm{tr}}$ is positive, indicating that heat is pumped from the left to the right reservoirs, although this directional flow would be flipped if the driving protocol was executed in reverse. This pumped heat exhibits a maximum where $T$ becomes comparable with the energy scale associated with the coupling strength to the external leads. This is a consequence of the energy window, within which scattering events can occur, exceeding the width of the resonance in the energy dependence of the scattering matrix, which is set by the coupling strength. Similarly, the dissipated heat $W$ is positive at all temperatures and

exhibits a maximum value at a much smaller temperature in comparison to that of the pumped heat (see inset).

The values of pumped heat and work can subsequently be used to calculate the coefficient of performance $\eta^{\text{hp}}$ of this Majorana heat pump, the behaviour of which is illustrated in Fig. 7.2(b). We see that the COP increases linearly with T in the low temperature regime, within which the pumped heat is increasing and the heat dissipated by the driving is falling. Beyond this regime, as the pumped heat drops below its optimum value, the rate of COP increase slows down. Fig. 7.2(c) demonstrates how the COP varies as a function of driving frequency. As expected, we see that the COP diverges in the adiabatic limit due to the constant nature of the geometric pumped heat $Q_{\text{tr}}$ and the suppression of the heat dissipated by the driving, which varies linearly with the driving frequency. The detrimental effect of this dissipation leads the COP to fall monotonically as the frequency is increased.

Next we assess the performance of the braiding operation as a refrigerator by applying a temperature gradient between the external leads. In Fig. 7.3(a) we again illustrate the behaviour of $Q_{\text{tr}}$ and $W$, this time as a function of $\Delta T$. The addition of the temperature bias means that the heat driven from the cold to the hot reservoir is now in constant competition with the heat flowing in the opposite direction due to the gradient $Q_{\text{tr}}^{\text{grad}}$. Eq. 7.22 indicates that this contribution varies linearly with $\Delta T$ and hence results in the decreasing linear dependence of the total transported heat seen in Fig. 7.3(a). The work $W$ performed by the driving also consists of a combination of two distinct contributions in the presence of a temperature bias. The addition of the geometric contribution from Eq. 7.25, corresponding to the energy input required to drive the pumped heat against the increasing temperature gradient, results in the weak

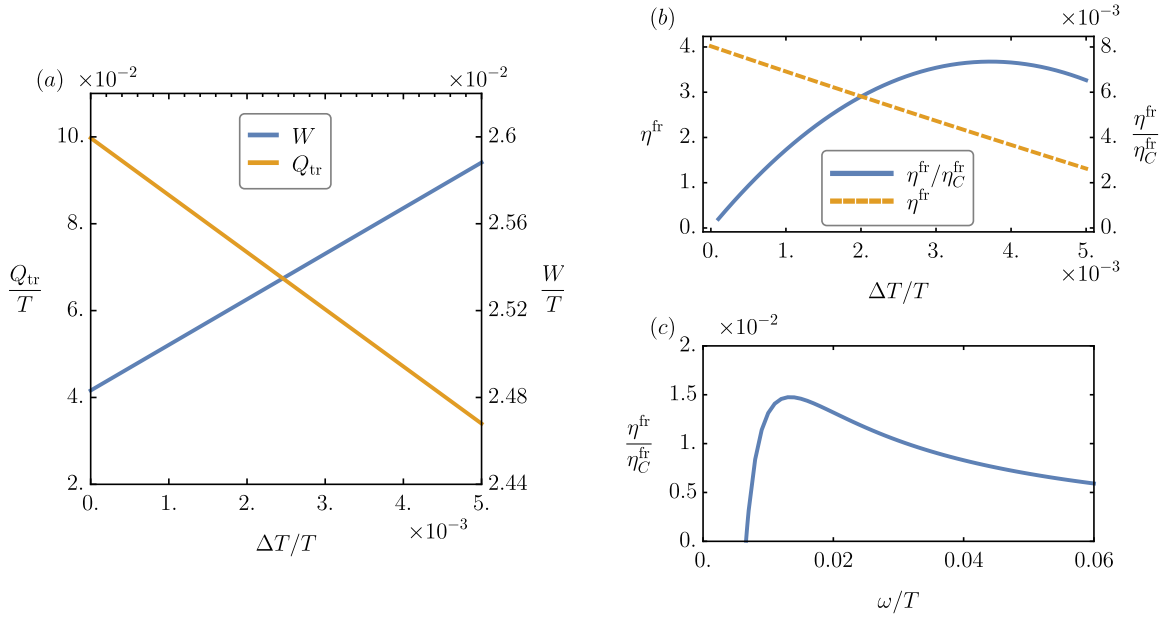


Figure 7.3: (a) Transported heat $Q_{\rm tr}$ and work done by the driving $W$ as a function of the temperature gradient between the hot and cold leads for a Majorana braiding exchange. We used a coupling strength to the external leads of $\Gamma_L = \Gamma_R = 0.01T$ and a driving frequency of $\omega = 0.02T$. In this regime the braiding operation results in a refrigeration effect, pumping heat from the cold to the hot bath. (b) Using the same system parameters, we plot the behaviour of the coefficient of performance $\eta^{\rm fr}$ versus $\Delta T$. We plot the COP normalized by the maximum Carnot value in addition to the raw value. (c) The normalized coefficient of performance is plotted as a function of driving frequency $\omega$ for $\Delta T/T = 0.0025$. The COP becomes negative for lower frequencies, where the static heat flow due to the temperature gradient dominates and the system no longer operates as a refrigerator.

linear dependence upon the temperature gradient.

Measurement of the transported heat and work by use of quantum calorimetric techniques [191–193], introduced at the end of Sec. 6.3.3, would again require extremely high sensitivity given that the quantities of interest are small relative to the temperature of the leads, as seen in Fig. 7.3(a). Ensuring that transport is restricted to the degenerate ground-space of the Majorana Y-junction requires that $T \ll \Delta_{\rm sc} \sim 0.2$meV [32, 57]. Consequently, the values of $Q_{\rm tr}$ and $W$ plotted in Fig. 7.3 would be beyond

the current best estimates of achievable sensitivity, corresponding to the detection of heat pulses of $\sim 100\mu$eV [193].

Fig. 7.3(b) illustrates the performance of the Majorana Y-junction as a refrigerator. The dotted line plots the COP $\eta^{\mathrm{fr}}$ and demonstrates that this decreases linearly with the temperature bias. This feature is again a result of the increasing heat flow due to the temperature difference, that acts to reduce the net heat pumped in the direction desirable for refrigeration and hence also decreases the overall efficiency. Conversely, taking the ratio of the raw COP and its maximum Carnot efficiency, $\eta^{\mathrm{fr}}/\eta_C^{\mathrm{fr}}$, results in a bell shaped curve with an optimal value of $\Delta T$. This can be explained by the fact that the Carnot COP for refrigeration is given by $\eta_C^{\mathrm{tr}} = T/\Delta T$. As a consequence, for small $\Delta T$ we would expect the ratio to vary linearly with $\Delta T$, before the increase in temperature gradient reduces the desired heat flux and forces the efficiency back towards zero.

Fig. 7.3(c) also indicates the existence of a optimal driving frequency that maximises the normalized COP. In the slow driving limit the static heat flow $Q_{\mathrm{tr}}^{\mathrm{grad}}$, which is directly proportional to the driving period, dominates and eventually eliminates the refrigeration effect entirely, indicated by the frequency at which the COP reaches zero. Driving at higher frequencies favours the pumped component of the heat transport $Q_{\mathrm{tr}}^{\mathrm{pump}}$ and thus results in an increasing COP. However, this increase is halted by the increasing dissipative component of the work exerted on the system by the external driving forces.

## 7.4 Discussion

We have utilized the heat pumping effect induced by the slow manipulation of Majorana zero modes within a Y-junction of superconducting nanowires in order to analyse the system's performance as a thermal machine. Such a machine is interesting in the sense that its operation relies only upon the manipulation of the internal system's degenerate ground state, without modulating its energy or the properties of the external leads.

By analysing the refrigeration performance of a Majorana exchange, we determined that it is the geometric contributions to both the heat transport $Q_{\mathrm{tr}}$ and the work done by the external driving $W$ that result in useful heat-work conversion, boosting the coefficient of performance. This observation is in agreement with a recent study by B. Bhandari *et al.* [63], in which they show that a machine operating purely geometrically would achieve the Carnot efficiency $\eta_C$ [63,69]. Additionally, for a machine based upon a Majorana exchange operating in this geometric limit, the efficiency would only depend upon the shape of the contour in parameter space associated with the driving and hence would share the topological protection against fluctuations to both the internal system and to the driving mechanism itself, as outlined in Sec. 6.2. This potential for a robust driven heat current represents a clear advantage of utilizing such a topologically protected operation as a thermal machine, however this should be offset by the low efficiencies, relative to the Carnot limit, found when using the parameters studied here.

However, the non-geometric contributions to both $Q_{\mathrm{tr}}$ and $W$ act as a source of entropy production and are hence detrimental to the efficiency of the pumping process. In terms of heat transport this non-geometric contribution is the steady-state heat flow from the hot to the cold bath that varies linearly with both the temperature gradient and driving period. With regards to the work, non-geometric terms arise in the form of heat

dissipated into the leads due to frictional effects of the driving, which are proportional to the driving frequency. These terms result in the emergence of optimal values of driving frequency and temperature gradient that maximize coefficient of performance.

This analysis could be further extended by considering the performance of the driven Y-junction as a heat engine, for which the heat flow is used to perform useful work. One should also, in addition to efficiency, consider the parameters for which the machine operates at maximum power, defined by the useful work performed for a heat engine and the heat removed from the cold bath in the refrigeration regime. Besides the lead temperature and driving frequency, it would also be of interest to analyse how driving along alternative contours in the parameter space of the Y-junction influences the performance.

Investigation of this system could be further extended by making use of the full counting statistics derived in Chap. 6 to analyse the nature of thermodynamic uncertainty relations in the context of this model. Such relations provide limits upon the precision of non-equilibrium currents in terms of the entropy production of the system [209]. They can further be used to provide tighter bounds upon the efficiency of thermal machines and their extension to periodically driven systems, for which geometric contributions to the transport become significant, is a subject of recent interest [210–212].

# Chapter 8

# Conclusions

In this thesis we have explored the impact of periodic driving upon the transport properties of mesoscopic systems hosting topologically protected excitations, with a particular focus upon Majorana zero modes. Firstly, in Chap. 5, we considered a system for which periodic driving results in the fabrication of additional topological phases compared to the system's static counterpart. It is known that such phases can be identified by the value of topological invariants obtained from a stroboscopic scattering matrix for pulsed coupling to the external leads. Although the experimentally accessible DC conductance is known to exhibit quantized peaks, corresponding to the existence of Majorana modes, when summed over Floquet sidebands, the exact relationship between the stroboscopic scattering matrix and the transport properties was yet to be fully understood.

We have attempted to shed further light on this relationship by comparing the DC conductance summed over Floquet sidebands with the period-averaged stroboscopic conductance for two distinct driving protocols of a 1D superconducting nanowire. We demonstrated that, in the limit of weak coupling to the external leads, the discrepancy

between the two quantities is captured by the difference in the widths of the resonant conductance peaks. In particular, it is the dependence of the resonance widths upon the offset time between the external driving and the pulsed coupling period that controls the discrepancy between the conductance quantities, with the difference larger when the weight of the Majorana mode upon the endmost sites depends strongly upon this offset time. This study provides a platform from which to explore signatures of Floquet topological phases in transport properties, building upon the relationships between scattering matrix invariants and topological phase classification established for non-driven systems.

In Chap. 6, we instead focus upon the effect of driving in terms of the slow manipulation of topologically protected zero modes, in the guise of a Majorana braiding protocol. We showed that the periodic nature of the system manipulation results in a geometric contribution to the full counting statistics of the transport, in addition to the dynamical part. In contrast to previous studies, this additional contribution was found to be present after only the manipulation of the degenerate ground state, as opposed to the properties of the external leads or the energy levels of the internal system. As a result, the parameters relevant for calculating these geometric contributions, defining the rotation of the zero energy modes in the space of the Majoranas physically coupled to the leads, do not correspond to the parameters of the system that would be driven in practice to initiate the braiding. The contour in this parameter space traced out throughout the protocol, which completely determines any geometric transport properties, is therefore independent of fluctuations in the driving mechanism. Furthermore, the degeneracy of the ground state, via which scattering events take place in the low temperature limit, is also protected by the topology of the

system.

We saw that the geometric contribution to the FCS leads to the braiding driving a finite heat current when connected to external free fermion reservoirs and that, since purely geometric in nature, this pumped heat shares the topological protection of the braiding operation itself. This robust heat current could potentially provide a signature of Majorana exchange for the next generation of experiments concerning the manipulation of topological superconducting systems.

Furthermore, we have explored the influence of the MZMs upon the temperature and frequency dependence of the heat and charge current noise, in addition to the consequences of the geometric contribution on the probability generating function in regards to exchange fluctuation theorems. We see that the presence of such a term results in a deviation from the standard form of the steady-state fluctuation theorems for heat exchange and arises due to the additional consideration of the energy exchange between the system and the external driving mechanism. In contrast to other works in which this geometric correction term is discussed, here we demonstrate its emergence after only driving a rotation of the degenerate ground-space of the internal system. Furthermore, in the case of the Majorana exchange, the geometric nature of this correction term means that it too shares the robust protection associated with the operation.

Finally, we have delved further into the thermodynamic properties of the Majorana braiding by examining its performance as a quantum thermal machine, for which the work performed by the external driving can be utilized to pump heat against a thermal gradient. The topologically protected nature of this pumped heat makes the driven Y-junction a particularly interesting candidate to study in this regard.

We see that non-geometric contributions to the heat transport and work exerted by the driving result in a competition between the desired heat pumping effect and the heat current flowing in response to the temperature bias across the device, as well as the frictional losses arising from the operation of the driving mechanism itself. These factors result in the suppression of the coefficient of performance, characterizing the Majorana exchange's capabilities as a refrigeration device, and hence allow for the identification of optimal temperature biases and driving frequencies that maximize efficiency.

# Appendix A

# Relationship between the Floquet and stroboscopic scattering matrices

Here we derive Eq. 5.24 of the main text, which gives the relationship between the stroboscopically defined scattering matrix which maintains a constant coupling to the external leads $\tilde{S}_t(E)$ and the full Floquet scattering matrix $S(E, E')$. We start by considering the form taken by the outgoing annihilation operators in the case that only scattering events separated by integer multiples of the driving period $T$, starting at some time $t$, are taken into account:

$$\begin{aligned} b_\alpha(t + nT) &= \sum_{\beta,m} \int dt' S(t + nT, t')_{\alpha\beta} a_\beta(t') \delta(t' - (t + mT)) \\ &= \sum_{\beta,m} S_{\alpha,\beta}(t + nT, t + mT) a_\beta(t + mT). \end{aligned} \tag{A.1}$$

Using the Fourier transform for this stroboscopic scenario, we have that

$$\begin{aligned} b_\alpha(E) &= \sum_n e^{iE(t+nT)} b_\alpha(t+nT) \\ &= \sum_{\beta,n,m} S_{\alpha\beta}(t+nT, t+mT) \int dE' a_\beta(E') e^{iE(t+nT)-iE'(t+mT)}. \end{aligned} \tag{A.2}$$

This operator is equivalent to that defined in terms of our stroboscopic scattering matrix with constant coupling, so that

$$b_\alpha(E) = \tilde{S}_{t,\alpha\beta}(E) a_\beta(E). \tag{A.3}$$

From this, we can determine a relationship between the two scattering matrices:

$$\begin{aligned} \sum_{nm} S_{\alpha\beta}(t+nT, t+mT) e^{iE(t+nT)-iE'(t+mT)} &= \tilde{S}_{t,\alpha\beta}(E)\delta(E-E'), \\ \implies S_{\alpha\beta}(t+nT, t+mT) &= \int dE e^{-iE(n-m)T} \tilde{S}_{t,\alpha\beta}(E). \end{aligned} \tag{A.4}$$

The two-time Floquet scattering matrix can also be expressed in terms of scattering between energies $E$ and $E_n = E + n\omega$ as

$$S(t,t') = \sum_n \int dE e^{-iE(t-t')+in\omega t'} S(E, E_n). \tag{A.5}$$

In the case that the two times are separated by an integer multiple of the driving frequency, we have that

$$\begin{aligned} S(t+nT, t+mT) &= \sum_l \int dE e^{-iE(nT-mT)+il\omega t} S(E, E_l) \\ &= \sum_{l,p} \int dE e^{-i(E+p\omega)(nT-mT)+il\omega t} S(E_p, E_{p+l}) \\ &= \int dE e^{-iE(n-m)T} \Big\{ \sum_{lp} e^{il\omega t} S(E_p, E_{p+l}) \Big\}. \end{aligned} \tag{A.6}$$

By comparison of this expression with that in Eq. A.4, we can determine the relationship between the scattering matrices introduced in Eq. 5.24 of the main text:

$$\tilde{S}_t(E) = \sum_{nm} e^{in\omega t} S(E_m, E_{m+n}). \tag{A.7}$$

# Appendix B

# Projective nature of the number operator matrices

Here we will show how products of number operators, defined in Sec. 6.1.1, which act at the same or different energies can be simplified in order to demonstrate their projective nature. In order to do this we must first consider several relationships that can be obtained from the unitarity of the scattering matrix. Treating the discretized particle energy levels as ingoing and outgoing propagation channels, we can write the scattering matrix in block form,

$$\hat{S} = \begin{pmatrix} \ddots & & & & & 0 \\ & S^{\alpha\beta}_{\omega}(\epsilon_i) & S^{\alpha\beta}(\epsilon_i) & S^{\alpha\beta}_{-\omega}(\epsilon_i) & & \\ & & S^{\alpha\beta}_{\omega}(\epsilon_{i+1}) & S^{\alpha\beta}(\epsilon_{i+1}) & S^{\alpha\beta}_{-\omega}(\epsilon_{i+1}) & \\ & & & S^{\alpha\beta}_{\omega}(\epsilon_{i+2}) & S^{\alpha\beta}(\epsilon_{i+2}) & S^{\alpha\beta}_{-\omega}(\epsilon_{i+2}) \\ & 0 & & & & \ddots \end{pmatrix}. \tag{B.1}$$

By writing the scattering matrix in this form we can immediately see that its unitarity gives us the following useful relations:

$$|S^{\alpha\beta}(\epsilon_i)|^2 + |S^{\alpha\beta}_{\omega}(\epsilon_i)|^2 + |S^{\alpha\beta}_{-\omega}(\epsilon_i)|^2 = \mathcal{I}, \tag{B.2a}$$

$$S^{\alpha\beta}(\epsilon_i)S^{\beta\gamma}_{\omega}(\epsilon_{i+1})^{\dagger} + S^{\alpha\beta}_{-\omega}(\epsilon_i)S^{\beta\gamma}(\epsilon_{i+1})^{\dagger} = 0, \tag{B.2b}$$

$$S^{\alpha\beta}_{-\omega}(\epsilon_i)S^{\beta\gamma}_{\omega}(\epsilon_{i+2})^{\dagger} = 0. \tag{B.2c}$$

These relationships can be further simplified by considering the symmetric nature of each of the blocks, so that $S^{\alpha\beta}(\epsilon_i)^{\dagger} = S^{\alpha\beta}(\epsilon_i)^{*}$ and $S^{\alpha\beta}_{\pm\omega}(\epsilon_i)^{\dagger} = S^{\alpha\beta}_{\pm\omega}(\epsilon_i)^{*}$.

Now let us consider, for example, the square of the outgoing number operator matrix at energy $\epsilon_i$:

$$P^2_{\epsilon_i\leftarrow} = (P^e_{\epsilon_i\leftarrow} + P^h_{\epsilon_i\leftarrow})^2 = (P^e_{\epsilon_i\leftarrow})^2 + (P^h_{\epsilon_i\leftarrow})^2 + P^e_{\epsilon_i\leftarrow}P^h_{\epsilon_i\leftarrow} + P^h_{\epsilon_i\leftarrow}P^e_{\epsilon_i\leftarrow}.$$

First considering the top left non-zero element of the matrix for the squared electron term, we have that

$$\begin{aligned}
\{(P^e_{\epsilon_i\leftarrow})^2\}_{ii} =& S^{\alpha 1}_{\omega}(\epsilon_i)^* S^{1\beta}_{\omega}(\epsilon_i) S^{\beta 1}_{\omega}(\epsilon_i)^* S^{1\gamma}_{\omega}(\epsilon_i) + S^{\alpha 1}_{\omega}(\epsilon_i)^* S^{1\beta}(\epsilon_i) S^{\beta 1}(\epsilon_i)^* S^{1\gamma}_{\omega}(\epsilon_i) \\
&+ S^{\alpha 1}_{\omega}(\epsilon_i)^* S^{1\beta}_{-\omega}(\epsilon_i) S^{\beta 1}_{-\omega}(\epsilon_i)^* S^{1\gamma}_{\omega}(\epsilon_i) \\
=& S^{\alpha 1}_{\omega}(\epsilon_i)^* \Big( S^{1\beta}_{\omega}(\epsilon_i) S^{\beta 1}_{\omega}(\epsilon_i)^* + S^{1\beta}(\epsilon_i) S^{\beta 1}(\epsilon_i)^* + S^{1\beta}_{-\omega}(\epsilon_i) S^{\beta 1}_{-\omega}(\epsilon_i)^* \Big) S^{1\gamma}_{\omega}(\epsilon_i) \\
=& S^{\alpha 1}_{\omega}(\epsilon_i)^* S^{1\gamma}_{\omega}(\epsilon_i) = \{P^e_{\epsilon_i\leftarrow}\}_{ii},
\end{aligned} \tag{B.3}$$

where in the final step we have made use of the unitarity relation given in Eq. B.2a. The same reasoning can be applied to the other components of the matrix and in the case of the outgoing number operator for holes. Hence we can conclude that $(P^e_{\epsilon_i\leftarrow})^2 = P^e_{\epsilon_i\leftarrow}$

and $(P^h_{\epsilon_i\leftarrow})^2 = P^h_{\epsilon_i\leftarrow}$. Next considering the cross-terms in the expansion we see that,

$$\begin{aligned}\{P^e_{\epsilon_i\leftarrow}P^h_{\epsilon_i\leftarrow}\}_{ii} =& S^{\alpha 1}_{\omega}(\epsilon_i)^* S^{1\beta}_{\omega}(\epsilon_i) S^{\beta 2}_{\omega}(\epsilon_i)^* S^{2\gamma}_{\omega}(\epsilon_i) + S^{\alpha 1}_{\omega}(\epsilon_i)^* S^{1\beta}(\epsilon_i) S^{\beta 2}(\epsilon_i)^* S^{2\gamma}_{\omega}(\epsilon_i) \\ &+ S^{\alpha 1}_{\omega}(\epsilon_i)^* S^{1\beta}_{-\omega}(\epsilon_i) S^{\beta 2}_{-\omega}(\epsilon_i)^* S^{2\gamma}_{\omega}(\epsilon_i) \\ =& S^{\alpha 1}_{\omega}(\epsilon_i)^* \Big( S^{1\beta}_{\omega}(\epsilon_i) S^{\beta 2}_{\omega}(\epsilon_i)^* + S^{1\beta}(\epsilon_i) S^{\beta 2}(\epsilon_i)^* + S^{1\beta}_{-\omega}(\epsilon_i) S^{\beta 2}_{-\omega}(\epsilon_i)^* \Big) S^{2\gamma}_{\omega}(\epsilon_i) \\ =& 0,\end{aligned} \tag{B.4}$$

where once again we have used Eq. B.2a. This results hold for all elements of the matrices $P^e_{\epsilon_i\leftarrow}P^h_{\epsilon_i\leftarrow}$ and $P^h_{\epsilon_i\leftarrow}P^e_{\epsilon_i\leftarrow}$ and hence we have demonstrated the projective nature of the outgoing number operator matrices at each energy: $P^2_{\epsilon_i\leftarrow} = P_{\epsilon_i\leftarrow}$.

Next we will show that, in addition to this result, the sum of the matrices $P_{\epsilon_i\leftarrow}$ over all energies is also itself a projector. In order to do this we will evaluate the product

$$\Big( \sum_i P^e_{\epsilon_i\leftarrow} + P^h_{\epsilon_i\leftarrow} \Big)^2.$$

Due to the shape of the $P$ matrices given in Eq. 6.11, we find that the only non-zero contributions to this product take the form:

$$\Big( P^e_{\epsilon_i\leftarrow} + P^h_{\epsilon_i\leftarrow} \Big) \Big( P^e_{\epsilon_j\leftarrow} + P^h_{\epsilon_j\leftarrow} \Big) \text{ where } |i-j| \leq 2. \tag{B.5}$$

For the case in which $i = j$ we have already shown that these matrices are projectors. Next considering the case $|i-j| = 1$, we will first consider the elements of the matrix $P^e_{\epsilon_i\leftarrow}P^e_{\epsilon_{i\pm 1}\leftarrow}$. In particular the top left non-zero element of this matrix will be of the

form

$$\begin{aligned}
\{P^e_{\epsilon_i\leftarrow}P^e_{\epsilon_{i+1}\leftarrow}\}_{i-1i} =& S^{\alpha 1}_{\omega}(\epsilon_i)^* S^{1\beta}(\epsilon_i) S^{\beta 1}_{\omega}(\epsilon_{i+1})^* S^{1\gamma}_{\omega}(\epsilon_{i+1}) + S^{\alpha 1}_{\omega}(\epsilon_i)^* S^{1\beta}_{-\omega}(\epsilon_i) S^{\beta 1}(\epsilon_{i+1})^* S^{1\gamma}_{\omega}(\epsilon_{i+1}) \\
=& S^{\alpha 1}(\epsilon_i)^* \Big( S^{1\beta}(\epsilon_i) S^{\beta 1}_{\omega}(\epsilon_{i+1})^* + S^{1\beta}_{-\omega}(\epsilon_i) S^{\beta 1}(\epsilon_{i+1})^* \Big) S^{1\gamma}_{\omega}(\epsilon_{i+1}) \\
=& 0. \\
\{P^e_{\epsilon_i\leftarrow}P^e_{\epsilon_{i-1}\leftarrow}\}_{i-1i} =& S^{\alpha 1}_{\omega}(\epsilon_i)^* S^{1\beta}_{\omega}(\epsilon_i) S^{\beta 1}(\epsilon_{i-1})^* S^{1\gamma}_{\omega}(\epsilon_{i-1}) + S^{\alpha 1}_{\omega}(\epsilon_i)^* S^{1\beta}(\epsilon_i) S^{\beta 1}_{-\omega}(\epsilon_{i-1})^* S^{1\gamma}_{\omega}(\epsilon_{i-1}) \\
=& S^{\alpha 1}_{\omega}(\epsilon_i)^* \Big( S^{1\beta}_{\omega}(\epsilon_i) S^{\beta 1}(\epsilon_{i-1})^* + S^{1\beta}(\epsilon_i) S^{\beta 1}_{-\omega}(\epsilon_{i-1})^* \Big) S^{1\gamma}_{\omega}(\epsilon_{i-1}) \\
=& 0.
\end{aligned} \tag{B.6}$$

Here we have used the relation given in Eq. B.2b and this relationship can be shown to hold true for every element of this matrix. In the case of holes, we also have that,

$$\begin{aligned}
\{P^h_{\epsilon_i\leftarrow}P^h_{\epsilon_{i+1}\leftarrow}\}_{i-1i} =& S^{\alpha 1}_{\omega}(\epsilon_i)^* S^{1\beta}(\epsilon_i) S^{\beta 1}_{\omega}(\epsilon_{i+1})^* S^{1\gamma}_{\omega}(\epsilon_{i+1}) + S^{\alpha 1}_{\omega}(\epsilon_i)^* S^{1\beta}_{-\omega}(\epsilon_i) S^{\beta 1}(\epsilon_{i+1})^* S^{1\gamma}_{\omega}(\epsilon_{i+1}) \\
=& S^{\beta 1}(\epsilon_i)^* S^{1\gamma}_{\omega}(\epsilon_i) \Big( S^{1\beta}(\epsilon_i) S^{\beta 1}_{\omega}(\epsilon_{i+1})^* + S^{1\beta}_{-\omega}(\epsilon_i) S^{\beta 1}(\epsilon_{i+1})^* \Big) S^{1\gamma}_{\omega}(\epsilon_{i+1}) \\
=& 0.
\end{aligned} \tag{B.7}$$

In the same way, it can be shown that the product terms between electrons and holes are also zero, so that $\Big(P^e_{\epsilon_i\leftarrow} + P^h_{\epsilon_i\leftarrow}\Big)\Big(P^e_{\epsilon_j\leftarrow} + P^h_{\epsilon_j\leftarrow}\Big) = 0$ when $|i-j| = 1$. Finally for the case of $|i-j| = 2$, we will again consider as an example the top left non-zero element of the relevant matrix:

$$\begin{aligned}
\{P^e_{\epsilon_i\leftarrow}P^e_{\epsilon_{i+1}\leftarrow}\}_{i-1i+1} =& S^{\alpha 1}_{\omega}(\epsilon_i)^* S^{1\beta}_{-\omega}(\epsilon_i) S^{\beta 1}_{\omega}(\epsilon_{i+2})^* S^{1\gamma}_{\omega}(\epsilon_{i+2}) \\
=& 0,
\end{aligned} \tag{B.8}$$

by Eq. B.2c. We have hence demonstrated the projective nature of the sum of the

number operator matrices,

$$\Big(\sum_i P^e_{\epsilon_i\leftarrow} + P^h_{\epsilon_i\leftarrow}\Big)^2 = \sum_i {P^e_{\epsilon_i\leftarrow}}^2 + {P^h_{\epsilon_i\leftarrow}}^2 = \sum_i P^e_{\epsilon_i\leftarrow} + P^h_{\epsilon_i\leftarrow}. \tag{B.9}$$

# Appendix C

# Unitarity condition of the scattering matrix

Here we will demonstrate how the unitarity of the full Floquet scattering matrix,

$$\sum_n \int d\epsilon S_{mn}(\epsilon', \epsilon) S^\dagger_{nk}(\epsilon, \epsilon'') = \delta(\epsilon' - \epsilon'')\delta_{mk}, \tag{C.1}$$

results in different constraints upon the matrices appearing in the slow driving expansion introduced in Eq. 7.17 from Chap. 7. Taking the Wigner transform of this expansion results in the requirement that

$$\sum_n \mathcal{S}_{mn}(\epsilon, t) * \mathcal{S}^\dagger_{nk}(\epsilon, t) = \delta_{mk}. \tag{C.2}$$

In the following we insert the expansion of the Wigner transformed scattering matrix into this expression and collect terms of the same order in the driving frequency.

## Zeroth order

To zeroth order in the frequency we have the unitarity condition of the frozen scattering matrix:

$$\sum_n S_{mn} S^\dagger_{nk} = \delta_{mk}. \tag{C.3}$$

## First order

Up to first order in the frequency the unitary condition can be expressed as

$$\sum_n \left[ S_{mn} S^\dagger_{nk} + A_{mn} S^\dagger_{nk} + S_{mn} A^\dagger_{nk} + \frac{i}{2}\left( \frac{\partial S_{mn}}{\partial \epsilon}\frac{\partial S^\dagger_{nk}}{\partial t} - \frac{\partial S_{mn}}{\partial t}\frac{\partial S^\dagger_{nk}}{\partial \epsilon} \right) \right] = \delta_{mk}, \tag{C.4}$$

with $A(\epsilon, t) = \sum_i \dot{X}_i A_i(\epsilon, t)$. Using the zeroth order condition this leads to the following constraint:

$$\sum_n \left[ A_{mn} S^\dagger_{nk} + S_{mn} A^\dagger_{nk} \right] = -\sum_n \frac{i}{2}\left( \frac{\partial S_{mn}}{\partial \epsilon}\frac{\partial S^\dagger_{nk}}{\partial t} - \frac{\partial S_{mn}}{\partial t}\frac{\partial S^\dagger_{nk}}{\partial \epsilon} \right). \tag{C.5}$$

## Second order

Expanding up to second order in frequency and using the relationships given in Eq. C.3 and C.5 gives

$$\begin{aligned} 0 = \sum_n \Bigg[ & A_{mn} A^\dagger_{nk} + S_{mn}(B^\dagger_{nk} + C^\dagger_{nk}) + (B_{mn} + C_{mn}) S^\dagger_{nk} \\ & + \frac{i}{2}\left( \frac{\partial A_{mn}}{\partial \epsilon}\frac{\partial S^\dagger_{nk}}{\partial t} - \frac{\partial A_{mn}}{\partial t}\frac{\partial S^\dagger_{nk}}{\partial \epsilon} \right) + \frac{i}{2}\left( \frac{\partial S_{mn}}{\partial \epsilon}\frac{\partial A^\dagger_{nk}}{\partial t} - \frac{\partial S_{mn}}{\partial t}\frac{\partial A^\dagger_{nk}}{\partial \epsilon} \right) \\ & - \frac{1}{8}\left( \frac{\partial^2 S_{mn}}{\partial \epsilon^2}\frac{\partial^2 S^\dagger_{nk}}{\partial t^2} + \frac{\partial^2 S_{mn}}{\partial t^2}\frac{\partial^2 S^\dagger_{nk}}{\partial \epsilon^2} - 2\frac{\partial^2 S_{mn}}{\partial \epsilon \partial t}\frac{\partial^2 S^\dagger_{nk}}{\partial t \partial \epsilon} \right) \Bigg], \end{aligned} \tag{C.6}$$

with $B(\epsilon,t) = \sum_{ij} \dot{X}_i \dot{X}_j B_{ij}(\epsilon,t)$ and $C(\epsilon,t) = \sum_i \ddot{X}_i C_i(\epsilon,t)$. This relationship is used to show that the matrices $B(\epsilon,t)$ and $C(\epsilon,t)$ do not contribute to the expansion of the outgoing operator $\phi_{\text{out}}$ in the limit of small temperature bias.

# Bibliography


[1] L. D. Landau, "On the theory of phase transitions. I.," *Zh. Eksp. Teor. Fiz.*, vol. 11, p. 19, 1937.

[2] L. D. Landau and V. L. Ginzburg, "On the theory of superconductivity," *Zh. Eksp. Teor. Fiz.*, vol. 20, p. 1064, 1950.

[3] L. Landau and E. Lifshitz, *Statistical Physics: Volume 5*. No. v. 5, Elsevier Science, 2013.

[4] K. v. Klitzing, G. Dorda, and M. Pepper, "New Method for High-Accuracy Determination of the Fine-Structure Constant Based on Quantized Hall Resistance," *Phys. Rev. Lett.*, vol. 45, pp. 494–497, aug 1980.

[5] R. B. Laughlin, "Quantized Hall conductivity in two dimensions," *Phys. Rev. B*, vol. 23, pp. 5632–5633, may 1981.

[6] D. J. Thouless, M. Kohmoto, M. P. Nightingale, and M. den Nijs, "Quantized Hall Conductance in a Two-Dimensional Periodic Potential," *Phys. Rev. Lett.*, vol. 49, pp. 405–408, aug 1982.

[7] X.-G. Wen, "Topological orders and edge excitations in fractional quantum Hall states," *Adv. Phys.*, vol. 44, pp. 405–473, oct 1995.

[8] M. Sato and Y. Ando, "Topological superconductors: A review," *Reports Prog. Phys.*, vol. 80, no. 7, pp. 1–45, 2017.

[9] M. Z. Hasan and C. L. Kane, "*Colloquium*: Topological insulators," *Rev. Mod. Phys.*, vol. 82, pp. 3045–3067, nov 2010.

[10] X.-G. Wen, "*Colloquium*: Zoo of quantum-topological phases of matter," *Rev. Mod. Phys.*, vol. 89, p. 041004, dec 2017.

[11] B. A. Bernevig and T. L. Hughes, *Topological insulators and topological superconductors*.

[12] J. Moore, "The next generation," *Nat. Phys.*, vol. 5, pp. 378–380, jun 2009.

[13] X.-L. Qi and S.-C. Zhang, "Topological insulators and superconductors," *Rev. Mod. Phys.*, vol. 83, pp. 1057–1110, oct 2011.

[14] B. I. Halperin, "Quantized Hall conductance, current-carrying edge states, and the existence of extended states in a two-dimensional disordered potential," *Phys. Rev. B*, vol. 25, pp. 2185–2190, feb 1982.

[15] A. P. Schnyder, S. Ryu, A. Furusaki, and A. W. W. Ludwig, "Classification of topological insulators and superconductors in three spatial dimensions," *Phys. Rev. B*, vol. 78, p. 195125, nov 2008.

[16] A. Kitaev, V. Lebedev, and M. Feigel'man, "Periodic table for topological insulators and superconductors," in *AIP Conf. Proc.*, vol. 1134, pp. 22–30, AIP, may 2009.

[17] N. Read and D. Green, "Paired states of fermions in two dimensions with breaking of parity and time-reversal symmetries and the fractional quantum Hall effect," *Phys. Rev. B*, vol. 61, pp. 10267–10297, apr 2000.

[18] A. Y. Kitaev, "Unpaired Majorana fermions in quantum wires," *Physics-Uspekhi*, vol. 44, pp. 131–136, oct 2001.

[19] F. Wilczek, "Majorana returns," *Nat. Phys.*, vol. 5, no. 9, pp. 614–618, 2009.

[20] J. Alicea, "New directions in the pursuit of Majorana fermions in solid state systems," *Reports Prog. Phys.*, vol. 75, p. 076501, jul 2012.

[21] T. D. Stanescu and S. Tewari, "Majorana fermions in semiconductor nanowires: fundamentals, modeling, and experiment," *J. Phys. Condens. Matter*, vol. 25, p. 233201, jun 2013.

[22] M. Sato and S. Fujimoto, "Majorana Fermions and Topology in Superconductors," *J. Phys. Soc. Japan*, vol. 85, p. 072001, jul 2016.

[23] D. A. Ivanov, "Non-Abelian Statistics of Half-Quantum Vortices in p -Wave Superconductors," *Phys. Rev. Lett.*, vol. 86, pp. 268–271, jan 2001.

[24] C. Nayak, S. H. Simon, A. Stern, M. Freedman, and S. Das Sarma, "Non-Abelian anyons and topological quantum computation," *Rev. Mod. Phys.*, vol. 80, pp. 1083–1159, sep 2008.

[25] S. D. Sarma, M. Freedman, and C. Nayak, "Majorana zero modes and topological quantum computation," *npj Quantum Inf.*, vol. 1, p. 15001, dec 2015.

[26] D. Aasen, M. Hell, R. V. Mishmash, A. Higginbotham, J. Danon, M. Leijnse, T. S. Jespersen, J. A. Folk, C. M. Marcus, K. Flensberg, and J. Alicea, "Milestones Toward Majorana-Based Quantum Computing," *Phys. Rev. X*, vol. 6, p. 031016, aug 2016.

[27] S. Plugge, L. A. Landau, E. Sela, A. Altland, K. Flensberg, and R. Egger, "Roadmap to Majorana surface codes," *Phys. Rev. B*, vol. 94, p. 174514, nov 2016.

[28] T. Karzig, C. Knapp, R. M. Lutchyn, P. Bonderson, M. B. Hastings, C. Nayak, J. Alicea, K. Flensberg, S. Plugge, Y. Oreg, C. M. Marcus, and M. H. Freedman, "Scalable designs for quasiparticle-poisoning-protected topological quantum computation with Majorana zero modes," *Phys. Rev. B*, vol. 95, p. 235305, jun 2017.

[29] F. Wilczek, *Fractional Statistics and Anyon Superconductivity.* International journal of modern physics, World Scientific, 1990.

[30] C. Beenakker, "Search for Majorana Fermions in Superconductors," *Annu. Rev. Condens. Matter Phys.*, vol. 4, pp. 113–136, apr 2013.

[31] R. M. Lutchyn, E. P. A. M. Bakkers, L. P. Kouwenhoven, P. Krogstrup, C. M. Marcus, and Y. Oreg, "Majorana zero modes in superconductor–semiconductor heterostructures," *Nat. Rev. Mater.*, vol. 3, pp. 52–68, may 2018.

[32] V. Mourik, K. Zuo, S. M. Frolov, S. R. Plissard, E. P. A. M. Bakkers, and L. P. Kouwenhoven, "Signatures of Majorana fermions in hybrid superconductor-semiconductor nanowire devices.," *Science*, vol. 336, pp. 1003–7, may 2012.

[33] M. T. Deng, S. Vaitiekėnas, E. B. Hansen, J. Danon, M. Leijnse, K. Flensberg, J. Nygård, P. Krogstrup, and C. M. Marcus, "Majorana bound state in a coupled quantum-dot hybrid-nanowire system," *Science (80-. ).*, vol. 354, pp. 1557–1562, dec 2016.

[34] S. M. Albrecht, A. P. Higginbotham, M. Madsen, F. Kuemmeth, T. S. Jespersen, J. Nygård, P. Krogstrup, and C. M. Marcus, "Exponential protection of zero modes in Majorana islands," *Nature*, vol. 531, pp. 206–209, mar 2016.

[35] C. J. Bolech and E. Demler, "Observing Majorana bound States in p -Wave Superconductors Using Noise Measurements in Tunneling Experiments," *Phys. Rev. Lett.*, vol. 98, p. 237002, jun 2007.

[36] K. T. Law, P. A. Lee, and T. K. Ng, "Majorana Fermion Induced Resonant Andreev Reflection," *Phys. Rev. Lett.*, vol. 103, p. 237001, dec 2009.

[37] C.-X. Liu, J. D. Sau, T. D. Stanescu, and S. Das Sarma, "Andreev bound states versus Majorana bound states in quantum dot-nanowire-superconductor hybrid structures: Trivial versus topological zero-bias conductance peaks," *Phys. Rev. B*, vol. 96, p. 075161, aug 2017.

[38] C. Moore, C. Zeng, T. D. Stanescu, and S. Tewari, "Quantized zero-bias conductance plateau in semiconductor-superconductor heterostructures without topological Majorana zero modes," *Phys. Rev. B*, vol. 98, p. 155314, oct 2018.

[39] B. van Heck, A. R. Akhmerov, F. Hassler, M. Burrello, and C. W. J. Beenakker, "Coulomb-assisted braiding of Majorana fermions in a Josephson junction array," *New J. Phys.*, vol. 14, p. 035019, mar 2012.

[40] S. Vijay and L. Fu, "Teleportation-based quantum information processing with Majorana zero modes," *Phys. Rev. B*, vol. 94, p. 235446, dec 2016.

[41] I. C. Fulga, F. Hassler, A. R. Akhmerov, and C. W. Beenakker, "Scattering formula for the topological quantum number of a disordered multimode wire," *Phys. Rev. B - Condens. Matter Mater. Phys.*, vol. 83, no. 15, pp. 1–8, 2011.

[42] I. C. Fulga, F. Hassler, and A. R. Akhmerov, "Scattering theory of topological insulators and superconductors," *Phys. Rev. B*, vol. 85, p. 165409, apr 2012.

[43] D. Meidan, A. Romito, and P. W. Brouwer, "Scattering matrix formulation of the topological index of interacting fermions in one-dimensional superconductors," *Phys. Rev. Lett.*, vol. 113, no. 5, pp. 1–5, 2014.

[44] A. Altland and M. R. Zirnbauer, "Nonstandard symmetry classes in mesoscopic normal-superconducting hybrid structures," *Phys. Rev. B*, vol. 55, pp. 1142–1161, jan 1997.

[45] T. Kitagawa, E. Berg, M. Rudner, and E. Demler, "Topological characterization of periodically driven quantum systems," *Phys. Rev. B*, vol. 82, p. 235114, dec 2010.

[46] A. Kundu and B. Seradjeh, "Transport Signatures of Floquet Majorana Fermions in Driven Topological Superconductors," *Phys. Rev. Lett.*, vol. 111, p. 136402, sep 2013.

[47] M. S. Rudner, N. H. Lindner, E. Berg, and M. Levin, "Anomalous Edge States and the Bulk-Edge Correspondence for Periodically Driven Two-Dimensional Systems," *Phys. Rev. X*, vol. 3, p. 031005, jul 2013.

[48] C. W. von Keyserlingk and S. L. Sondhi, "Phase structure of one-dimensional interacting Floquet systems. I. Abelian symmetry-protected topological phases," *Phys. Rev. B*, vol. 93, p. 245145, jun 2016.

[49] A. C. Potter, T. Morimoto, and A. Vishwanath, "Classification of Interacting Topological Floquet Phases in One Dimension," *Phys. Rev. X*, vol. 6, p. 041001, oct 2016.

[50] D. V. Else and C. Nayak, "Classification of topological phases in periodically driven interacting systems," *Phys. Rev. B*, vol. 93, p. 201103, may 2016.

[51] M. Thakurathi, D. Loss, and J. Klinovaja, "Floquet Majorana fermions and parafermions in driven Rashba nanowires," *Phys. Rev. B*, vol. 95, p. 155407, apr 2017.

[52] F. Nathan and M. S. Rudner, "Topological singularities and the general classification of Floquet–Bloch systems," *New J. Phys.*, vol. 17, p. 125014, dec 2015.

[53] I. C. Fulga and M. Maksymenko, "Scattering matrix invariants of Floquet topological insulators," *Phys. Rev. B*, vol. 93, p. 75405, 2016.

[54] P. W. Brouwer, "Scattering approach to parametric pumping," *Phys. Rev. B*, vol. 58, pp. R10135–R10138, oct 1998.

[55] T. A. Shutenko, I. L. Aleiner, and B. L. Altshuler, "Mesoscopic fluctuations of adiabatic charge pumping in quantum dots," *Phys. Rev. B*, vol. 61, pp. 10366–10375, apr 2000.

[56] E. Cohen, H. Larocque, F. Bouchard, F. Nejadsattari, Y. Gefen, and E. Karimi, "Geometric phase from Aharonov–Bohm to Pancharatnam–Berry and beyond," *Nat. Rev. Phys.*, vol. 1, pp. 437–449, jul 2019.

[57] D. Meidan, T. Gur, and A. Romito, "Heat pumping from braiding Majorana zero modes," *Phys. Rev. B*, vol. 99, p. 205101, may 2019.

[58] J. Ren, P. Hänggi, and B. Li, "Berry-Phase-Induced Heat Pumping and Its Impact on the Fluctuation Theorem," *Phys. Rev. Lett.*, vol. 104, p. 170601, apr 2010.

[59] K. L. Watanabe and H. Hayakawa, "Geometric fluctuation theorem for a spin-boson system," *Phys. Rev. E*, vol. 96, p. 022118, aug 2017.

[60] Y. Hino and H. Hayakawa, "Fluctuation relations for adiabatic pumping," *Phys. Rev. E*, vol. 102, p. 012115, jul 2020.

[61] R.-P. Riwar and J. Splettstoesser, "Transport fluctuation relations in interacting quantum pumps," *New J. Phys.*, vol. 23, p. 013010, jan 2021.

[62] H. P. Goswami, B. K. Agarwalla, and U. Harbola, "Geometric effects in nonequilibrium electron transfer statistics in adiabatically driven quantum junctions," *Phys. Rev. B*, vol. 93, p. 195441, may 2016.

[63] B. Bhandari, P. T. Alonso, F. Taddei, F. von Oppen, R. Fazio, and L. Arrachea, "Geometric properties of adiabatic quantum thermal machines," *Phys. Rev. B*, vol. 102, p. 155407, oct 2020.

[64] K. Brandner and K. Saito, "Thermodynamic Geometry of Microscopic Heat Engines," *Phys. Rev. Lett.*, vol. 124, p. 040602, jan 2020.

[65] Y. Hino and H. Hayakawa, "Geometrical formulation of adiabatic pumping as a heat engine," *Phys. Rev. Res.*, vol. 3, p. 013187, feb 2021.

[66] E. Potanina, C. Flindt, M. Moskalets, and K. Brandner, "Thermodynamic bounds on coherent transport in periodically driven conductors," *Phys. Rev. X*, vol. 11, p. 021013, apr 2021.

[67] H. Pothier, P. Lafarge, C. Urbina, D. Esteve, and M. H. Devoret, "Single-Electron Pump Based on Charging Effects," *Europhys. Lett.*, vol. 17, pp. 249–254, jan 1992.

[68] N. Li, J. Ren, L. Wang, G. Zhang, P. Hänggi, and B. Li, "*Colloquium*: Phononics: Manipulating heat flow with electronic analogs and beyond," *Rev. Mod. Phys.*, vol. 84, pp. 1045–1066, jul 2012.

[69] S. Juergens, F. Haupt, M. Moskalets, and J. Splettstoesser, "Thermoelectric performance of a driven double quantum dot," *Phys. Rev. B*, vol. 87, p. 245423, jun 2013.

[70] B. Roche, R.-P. Riwar, B. Voisin, E. Dupont-Ferrier, R. Wacquez, M. Vinet, M. Sanquer, J. Splettstoesser, and X. Jehl, "A two-atom electron pump," *Nat. Commun.*, vol. 4, p. 1581, jun 2013.

[71] J. P. Peterson, T. B. Batalhão, M. Herrera, A. M. Souza, R. S. Sarthour, I. S. Oliveira, and R. M. Serra, "Experimental Characterization of a Spin Quantum Heat Engine," *Phys. Rev. Lett.*, vol. 123, p. 240601, dec 2019.

[72] T. W. Gamelin and R. E. Greene, *Introduction to topology*. Dover Publications, 1999.

[73] M. Nakahara, *Geometry, Topology and Physics, Second Edition*. Graduate student series in physics, Taylor & Francis, 2003.

[74] F. Bloch, "Über die Quantenmechanik der Elektronen in Kristallgittern," *Zeitschrift für Phys.*, vol. 52, pp. 555–600, jul 1929.

[75] M. V. Berry, "Quantal Phase Factors Accompanying Adiabatic Changes," *Proc. R. Soc. A*, vol. 392, pp. 45–57, mar 1984.

[76] D. Xiao, M.-C. Chang, and Q. Niu, "Berry phase effects on electronic properties," *Rev. Mod. Phys.*, vol. 82, pp. 1959–2007, jul 2010.

[77] J. Asbóth, L. Oroszlány, and A. Pályi, *A Short Course on Topological Insulators: Band Structure and Edge States in One and Two Dimensions*. Lecture Notes in Physics, Springer International Publishing, 2016.

[78] C. L. Kane and E. J. Mele, "Quantum Spin Hall Effect in Graphene," *Phys. Rev. Lett.*, vol. 95, p. 226801, nov 2005.

[79] C. L. Kane and E. J. Mele, "$Z_2$ Topological Order and the Quantum Spin Hall Effect," *Phys. Rev. Lett.*, vol. 95, p. 146802, sep 2005.

[80] P. Jacquod, R. S. Whitney, J. Meair, and M. Büttiker, "Onsager relations in coupled electric, thermoelectric, and spin transport: The tenfold way," *Phys. Rev. B*, vol. 86, p. 155118, oct 2012.

[81] M. Leijnse and K. Flensberg, "Introduction to topological superconductivity and Majorana fermions," *Semicond. Sci. Technol.*, vol. 27, p. 124003, dec 2012.

[82] R. Jackiw and C. Rebbi, "Solitons with fermion number 1/2," *Phys. Rev. D*, vol. 13, pp. 3398–3409, jun 1976.

[83] J. C. Y. Teo and C. L. Kane, "Topological defects and gapless modes in insulators and superconductors," *Phys. Rev. B*, vol. 82, p. 115120, sep 2010.

[84] G. E. Volovik, "Fermion zero modes on vortices in chiral superconductors," *J. Exp. Theor. Phys. Lett.*, vol. 70, pp. 609–614, nov 1999.

[85] Y. Maeno, S. Kittaka, T. Nomura, S. Yonezawa, and K. Ishida, "Evaluation of Spin-Triplet Superconductivity in $Sr_2RuO_4$," *J. Phys. Soc. Japan*, vol. 81, p. 011009, jan 2012.

[86] C. Kallin and J. Berlinsky, "Chiral superconductors," *Reports Prog. Phys.*, vol. 79, p. 054502, may 2016.

[87] L. Fu and E. Berg, "Odd-Parity Topological Superconductors: Theory and Application to $Cu_xBi_2Se_3$," *Phys. Rev. Lett.*, vol. 105, p. 097001, aug 2010.

[88] T. H. Hsieh and L. Fu, "Majorana Fermions and Exotic Surface Andreev Bound States in Topological Superconductors: Application to $Cu_xBi_2Se_3$," *Phys. Rev. Lett.*, vol. 108, p. 107005, mar 2012.

[89] L. Fu and C. L. Kane, "Superconducting Proximity Effect and Majorana Fermions at the Surface of a Topological Insulator," *Phys. Rev. Lett.*, vol. 100, p. 096407, mar 2008.

[90] J. D. Sau, R. M. Lutchyn, S. Tewari, and S. Das Sarma, "Robustness of Majorana fermions in proximity-induced superconductors," *Phys. Rev. B*, vol. 82, p. 094522, sep 2010.

[91] J. Alicea, Y. Oreg, G. Refael, F. von Oppen, and M. P. A. Fisher, "Non-Abelian statistics and topological quantum information processing in 1D wire networks," *Nat. Phys.*, vol. 7, pp. 412–417, may 2011.

[92] Y. Oreg, G. Refael, and F. von Oppen, "Helical Liquids and Majorana Bound States in Quantum Wires," *Phys. Rev. Lett.*, vol. 105, p. 177002, oct 2010.

[93] R. M. Lutchyn, J. D. Sau, and S. Das Sarma, "Majorana Fermions and a Topological Phase Transition in Semiconductor-Superconductor Heterostructures," *Phys. Rev. Lett.*, vol. 105, p. 077001, aug 2010.

[94] P. Boykin, T. Mor, M. Pulver, V. Roychowdhury, and F. Vatan, "A new universal and fault-tolerant quantum basis," *Inf. Process. Lett.*, vol. 75, pp. 101–107, aug 2000.

[95] O. Zilberberg, B. Braunecker, and D. Loss, "Controlled-NOT gate for multiparticle qubits and topological quantum computation based on parity measurements," *Phys. Rev. A*, vol. 77, p. 012327, jan 2008.

[96] S. Hoffman, C. Schrade, J. Klinovaja, and D. Loss, "Universal quantum computation with hybrid spin-Majorana qubits," *Phys. Rev. B*, vol. 94, p. 045316, jul 2016.

[97] J. C. Budich, S. Walter, and B. Trauzettel, "Failure of protection of Majorana based qubits against decoherence," *Phys. Rev. B*, vol. 85, p. 121405, mar 2012.

[98] D. Rainis and D. Loss, "Majorana qubit decoherence by quasiparticle poisoning," *Phys. Rev. B*, vol. 85, p. 174533, may 2012.

[99] G. C. Ménard, F. K. Malinowski, D. Puglia, D. I. Pikulin, T. Karzig, B. Bauer, P. Krogstrup, and C. M. Marcus, "Suppressing quasiparticle poisoning with a voltage-controlled filter," *Phys. Rev. B*, vol. 100, p. 165307, oct 2019.

[100] T. Karzig, W. S. Cole, and D. I. Pikulin, "Quasiparticle Poisoning of Majorana Qubits," *Phys. Rev. Lett.*, vol. 126, p. 057702, feb 2021.

[101] S. Vijay, T. H. Hsieh, and L. Fu, "Majorana Fermion Surface Code for Universal Quantum Computation," *Phys. Rev. X*, vol. 5, p. 041038, dec 2015.

[102] L. Landau, S. Plugge, E. Sela, A. Altland, S. Albrecht, and R. Egger, "Towards Realistic Implementations of a Majorana Surface Code," *Phys. Rev. Lett.*, vol. 116, p. 050501, feb 2016.

[103] D. Litinski and F. von Oppen, "Quantum computing with Majorana fermion codes," *Phys. Rev. B*, vol. 97, p. 205404, may 2018.

[104] T. D. Stanescu, J. D. Sau, R. M. Lutchyn, and S. Das Sarma, "Proximity effect at the superconductor–topological insulator interface," *Phys. Rev. B*, vol. 81, p. 241310, jun 2010.

[105] M. T. Deng, C. L. Yu, G. Y. Huang, M. Larsson, P. Caroff, and H. Q. Xu, "Anomalous zero-bias conductance peak in a Nb-InSb nanowire-Nb hybrid device.," *Nano Lett.*, vol. 12, pp. 6414–9, dec 2012.

[106] A. Das, Y. Ronen, Y. Most, Y. Oreg, M. Heiblum, and H. Shtrikman, "Zero-bias peaks and splitting in an Al–InAs nanowire topological superconductor as a signature of Majorana fermions," *Nat. Phys.*, vol. 8, pp. 887–895, dec 2012.

[107] L. P. Rokhinson, X. Liu, and J. K. Furdyna, "The fractional a.c. Josephson effect in a semiconductor–superconductor nanowire as a signature of Majorana particles," *Nat. Phys.*, vol. 8, pp. 795–799, nov 2012.

[108] S. M. Frolov, M. J. Manfra, and J. D. Sau, "Topological superconductivity in hybrid devices," *Nat. Phys.*, vol. 16, pp. 718–724, jul 2020.

[109] E. Prada, P. San-Jose, and R. Aguado, "Transport spectroscopy of N S nanowire junctions with Majorana fermions," *Phys. Rev. B*, vol. 86, p. 180503, nov 2012.

[110] E. J. H. Lee, X. Jiang, M. Houzet, R. Aguado, C. M. Lieber, and S. De Franceschi, "Spin-resolved Andreev levels and parity crossings in hybrid superconductor–semiconductor nanostructures," *Nat. Nanotechnol.*, vol. 9, pp. 79–84, jan 2014.

[111] O. A. Awoga, J. Cayao, and A. M. Black-Schaffer, "Supercurrent Detection of Topologically Trivial Zero-Energy States in Nanowire Junctions," *Phys. Rev. Lett.*, vol. 123, p. 117001, sep 2019.

[112] E. Prada, P. San-Jose, M. W. A. de Moor, A. Geresdi, E. J. H. Lee, J. Klinovaja, D. Loss, J. Nygård, R. Aguado, and L. P. Kouwenhoven, "From Andreev to Majorana bound states in hybrid superconductor–semiconductor nanowires," *Nat. Rev. Phys.*, vol. 2, pp. 575–594, oct 2020.

[113] S. Das Sarma and H. Pan, "Disorder-induced zero-bias peaks in Majorana nanowires," *Phys. Rev. B*, vol. 103, p. 195158, may 2021.

[114] S. D. Escribano, A. L. Yeyati, and E. Prada, "Interaction-induced zero-energy pinning and quantum dot formation in Majorana nanowires," *Beilstein J. Nanotechnol.*, vol. 9, pp. 2171–2180, aug 2018.

[115] A. Grivnin, E. Bor, M. Heiblum, Y. Oreg, and H. Shtrikman, "Concomitant opening of a bulk-gap with an emerging possible Majorana zero mode," *Nat. Commun.*, vol. 10, p. 1940, dec 2019.

[116] G. Ménard, G. Anselmetti, E. Martinez, D. Puglia, F. Malinowski, J. Lee, S. Choi, M. Pendharkar, C. Palmstrøm, K. Flensberg, C. Marcus, L. Casparis, and A. Higginbotham, "Conductance-Matrix Symmetries of a Three-Terminal Hybrid Device," *Phys. Rev. Lett.*, vol. 124, p. 036802, jan 2020.

[117] D. Puglia, E. A. Martinez, G. C. Ménard, A. Pöschl, S. Gronin, G. C. Gardner, R. Kallaher, M. J. Manfra, C. M. Marcus, A. P. Higginbotham, and L. Casparis, "Closing of the induced gap in a hybrid superconductor-semiconductor nanowire," *Phys. Rev. B*, vol. 103, p. 235201, jun 2021.

[118] A. R. Akhmerov, J. P. Dahlhaus, F. Hassler, M. Wimmer, and C. W. J. Beenakker, "Quantized Conductance at the Majorana Phase Transition in a Disordered Superconducting Wire," *Phys. Rev. Lett.*, vol. 106, p. 057001, jan 2011.

[119] D. Chevallier, P. Szumniak, S. Hoffman, D. Loss, and J. Klinovaja, "Topological phase detection in Rashba nanowires with a quantum dot," *Phys. Rev. B*, vol. 97, p. 045404, jan 2018.

[120] T. Ö. Rosdahl, A. Vuik, M. Kjaergaard, and A. R. Akhmerov, "Andreev rectifier: A nonlocal conductance signature of topological phase transitions," *Phys. Rev. B*, vol. 97, p. 045421, jan 2018.

[121] K. Flensberg, F. von Oppen, and A. Stern, "Engineered platforms for topological superconductivity and Majorana zero modes," *Nat. Rev. Mater.*, vol. 6, pp. 944–958, oct 2021.

[122] H. Ren, F. Pientka, S. Hart, A. T. Pierce, M. Kosowsky, L. Lunczer, R. Schlereth, B. Scharf, E. M. Hankiewicz, L. W. Molenkamp, B. I. Halperin, and A. Yacoby, "Topological superconductivity in a phase-controlled Josephson junction," *Nature*, vol. 569, pp. 93–98, may 2019.

[123] B. Jäck, Y. Xie, J. Li, S. Jeon, B. A. Bernevig, and A. Yazdani, "Observation of a Majorana zero mode in a topologically protected edge channel," *Science (80-. ).*, vol. 364, pp. 1255–1259, jun 2019.

[124] H. Zhang, D. E. Liu, M. Wimmer, and L. P. Kouwenhoven, "Next steps of quantum transport in Majorana nanowire devices," *Nat. Commun.*, vol. 10, p. 5128, dec 2019.

[125] R. Landauer, "Spatial Variation of Currents and Fields Due to Localized Scatterers in Metallic Conduction," *IBM J. Res. Dev.*, vol. 1, pp. 223–231, jul 1957.

[126] R. Landauer, "Electrical resistance of disordered one-dimensional lattices," *Philos. Mag.*, vol. 21, pp. 863–867, apr 1970.

[127] M. Büttiker, "Four-Terminal Phase-Coherent Conductance," *Phys. Rev. Lett.*, vol. 57, pp. 1761–1764, oct 1986.

[128] M. Büttiker, "Scattering theory of thermal and excess noise in open conductors," *Phys. Rev. Lett.*, vol. 65, pp. 2901–2904, dec 1990.

[129] S. Datta, *Electronic Transport in Mesoscopic Systems*. Cambridge Studies in Semiconductor Physics and Microelectronic Engineering, Cambridge University Press, 1997.

[130] M. Moskalets, *Scattering Matrix Approach to Non-stationary Quantum Transport*. Imperial College Press, 2012.

[131] M. Büttiker, "Scattering theory of current and intensity noise correlations in conductors and wave guides," *Phys. Rev. B*, vol. 46, pp. 12485–12507, nov 1992.

[132] Y. Blanter and M. Büttiker, "Shot noise in mesoscopic conductors," *Phys. Rep.*, vol. 336, pp. 1–166, sep 2000.

[133] G. B. Lesovik and I. A. Sadovskyy, "Scattering matrix approach to the description of quantum electron transport," *Physics-Uspekhi*, vol. 54, pp. 1007–1059, oct 2011.

[134] D. S. Fisher and P. A. Lee, "Relation between conductivity and transmission matrix," *Phys. Rev. B*, vol. 23, pp. 6851–6854, jun 1981.

[135] G. E. Blonder, M. Tinkham, and T. M. Klapwijk, "Transition from metallic to tunneling regimes in superconducting microconstrictions: Excess current, charge imbalance, and supercurrent conversion," *Phys. Rev. B*, vol. 25, pp. 4515–4532, apr 1982.

[136] C. J. Lambert, "Generalized Landauer formulae for quasi-particle transport in disordered superconductors," *J. Phys. Condens. Matter*, vol. 3, pp. 6579–6587, aug 1991.

[137] C. J. Lambert, V. C. Hui, and S. J. Robinson, "Multi-probe conductance formulae for mesoscopic superconductors," *J. Phys. Condens. Matter*, vol. 5, pp. 4187–4206, jun 1993.

[138] C. W. J. Beenakker, "Random-matrix theory of quantum transport," *Rev. Mod. Phys.*, vol. 69, pp. 731–808, jul 1997.

[139] C. J. Lambert and R. Raimondi, "Phase-coherent transport in hybrid superconducting nanostructures," *J. Phys. Condens. Matter*, vol. 10, pp. 901–941, feb 1998.

[140] A. F. Andreev, "Thermal conductivity of the intermediate state of superconductors," *Zh. Eksperim. i Teor. Fiz.*, vol. Vol: 46, may 1964.

[141] M. Moskalets and M. Büttiker, "Floquet scattering theory of quantum pumps," *Phys. Rev. B*, vol. 66, p. 205320, nov 2002.

[142] M. Moskalets and M. Büttiker, "Floquet scattering theory for current and heat noise in large amplitude adiabatic pumps," *Phys. Rev. B*, vol. 70, p. 245305, dec 2004.

[143] M. Moskalets, "Floquet Scattering Matrix Theory of Heat Fluctuations in Dynamical Quantum Conductors," *Phys. Rev. Lett.*, vol. 112, p. 206801, may 2014.

[144] V. Khemani, A. Lazarides, R. Moessner, and S. Sondhi, "Phase Structure of Driven Quantum Systems," *Phys. Rev. Lett.*, vol. 116, p. 250401, jun 2016.

[145] N. Yao, A. Potter, I.-D. Potirniche, and A. Vishwanath, "Discrete Time Crystals: Rigidity, Criticality, and Realizations," *Phys. Rev. Lett.*, vol. 118, p. 030401, jan 2017.

[146] J. Zhang, P. W. Hess, A. Kyprianidis, P. Becker, A. Lee, J. Smith, G. Pagano, I.-D. Potirniche, A. C. Potter, A. Vishwanath, N. Y. Yao, and C. Monroe, "Observation of a discrete time crystal," *Nature*, vol. 543, pp. 217–220, mar 2017.

[147] M. Moskalets and M. Büttiker, "Magnetic-field symmetry of pump currents of adiabatically driven mesoscopic structures," *Phys. Rev. B*, vol. 72, p. 035324, jul 2005.

[148] H. B. Callen and T. A. Welton, "Irreversibility and Generalized Noise," *Phys. Rev.*, vol. 83, pp. 34–40, jul 1951.

[149] R. Kubo, "Statistical-Mechanical Theory of Irreversible Processes. I. General Theory and Simple Applications to Magnetic and Conduction Problems," *J. Phys. Soc. Japan*, vol. 12, pp. 570–586, jun 1957.

[150] M. Toda, R. Kubo, R. Kubo, M. Toda, N. Saito, N. Hashitsume, and N. Hashitsume, *Statistical Physics II: Nonequilibrium Statistical Mechanics*. Springer Series in Solid-State Sciences, Springer Berlin Heidelberg, 2012.

[151] M. Campisi, P. Hänggi, and P. Talkner, "*Colloquium*: Quantum fluctuation relations: Foundations and applications," *Rev. Mod. Phys.*, vol. 83, pp. 771–791, jul 2011.

[152] G. N. Bochkov and I. E. Kuzovlev, "General theory of thermal fluctuations in nonlinear systems," *Zhurnal Eksperimentalnoi i Teoreticheskoi Fiziki*, vol. 72, pp. 238–247, Jan. 1977.

[153] M. Esposito, U. Harbola, and S. Mukamel, "Nonequilibrium fluctuations, fluctuation theorems, and counting statistics in quantum systems," *Rev. Mod. Phys.*, vol. 81, pp. 1665–1702, dec 2009.

[154] C. Jarzynski, "Nonequilibrium Equality for Free Energy Differences," *Phys. Rev. Lett.*, vol. 78, pp. 2690–2693, apr 1997.

[155] C. Jarzynski, "Equalities and Inequalities: Irreversibility and the Second Law of Thermodynamics at the Nanoscale," *Annu. Rev. Condens. Matter Phys.*, vol. 2, pp. 329–351, mar 2011.

[156] G. E. Crooks, "Entropy production fluctuation theorem and the nonequilibrium work relation for free energy differences," *Phys. Rev. E*, vol. 60, pp. 2721–2726, sep 1999.

[157] D. J. Evans, E. G. D. Cohen, and G. P. Morriss, "Probability of second law violations in shearing steady states," *Phys. Rev. Lett.*, vol. 71, pp. 2401–2404, oct 1993.

[158] G. Gallavotti and E. G. D. Cohen, "Dynamical Ensembles in Nonequilibrium Statistical Mechanics," *Phys. Rev. Lett.*, vol. 74, pp. 2694–2697, apr 1995.

[159] C. Jarzynski and D. K. Wójcik, "Classical and Quantum Fluctuation Theorems for Heat Exchange," *Phys. Rev. Lett.*, vol. 92, p. 230602, jun 2004.

[160] K. Saito and Y. Utsumi, "Symmetry in full counting statistics, fluctuation theorem, and relations among nonlinear transport coefficients in the presence of a magnetic field," *Phys. Rev. B*, vol. 78, p. 115429, sep 2008.

[161] D. Andrieux, P. Gaspard, T. Monnai, and S. Tasaki, "The fluctuation theorem for currents in open quantum systems," *New J. Phys.*, vol. 11, p. 043014, apr 2009.

[162] Y. Li, A. Kundu, F. Zhong, and B. Seradjeh, "Tunable Floquet Majorana fermions in driven coupled quantum dots," *Phys. Rev. B*, vol. 90, p. 121401, sep 2014.

[163] B. Bauer, T. Pereg-Barnea, T. Karzig, M.-T. Rieder, G. Refael, E. Berg, and Y. Oreg, "Topologically protected braiding in a single wire using Floquet Majorana modes," *Phys. Rev. B*, vol. 100, p. 041102, jul 2019.

[164] D. T. Liu, J. Shabani, and A. Mitra, "Floquet Majorana zero and $\pi$ modes in planar Josephson junctions," *Phys. Rev. B*, vol. 99, p. 094303, mar 2019.

[165] L. Jiang, T. Kitagawa, J. Alicea, A. R. Akhmerov, D. Pekker, G. Refael, J. I. Cirac, E. Demler, M. D. Lukin, and P. Zoller, "Majorana Fermions in Equilibrium and in Driven Cold-Atom Quantum Wires," *Phys. Rev. Lett.*, vol. 106, p. 220402, jun 2011.

[166] A. A. Reynoso and D. Frustaglia, "Unpaired Floquet Majorana fermions without magnetic fields," *Phys. Rev. B*, vol. 87, p. 115420, mar 2013.

[167] M. Thakurathi, A. A. Patel, D. Sen, and A. Dutta, "Floquet generation of Majorana end modes and topological invariants," *Phys. Rev. B*, vol. 88, p. 155133, oct 2013.

[168] A. Farrell and T. Pereg-Barnea, "Photon-Inhibited Topological Transport in Quantum Well Heterostructures," *Phys. Rev. Lett.*, vol. 115, p. 106403, sep 2015.

[169] A. Farrell and T. Pereg-Barnea, "Edge-state transport in Floquet topological insulators," *Phys. Rev. B*, vol. 93, p. 045121, jan 2016.

[170] C. Peng, A. Haim, T. Karzig, Y. Peng, and G. Refael, "Floquet Majorana bound states in voltage-biased planar Josephson junctions," *Phys. Rev. Res.*, vol. 3, p. 023108, may 2021.

[171] I. Martin, G. Refael, and B. Halperin, "Topological Frequency Conversion in Strongly Driven Quantum Systems," *Phys. Rev. X*, vol. 7, p. 041008, oct 2017.

[172] Y. Peng and G. Refael, "Time-quasiperiodic topological superconductors with Majorana multiplexing," *Phys. Rev. B*, vol. 98, p. 220509, dec 2018.

[173] T. Ozawa, H. M. Price, N. Goldman, O. Zilberberg, and I. Carusotto, "Synthetic dimensions in integrated photonics: From optical isolation to four-dimensional quantum Hall physics," *Phys. Rev. A*, vol. 93, p. 043827, apr 2016.

[174] R. W. Bomantara and J. Gong, "Quantum computation via Floquet topological edge modes," *Phys. Rev. B*, vol. 98, p. 165421, oct 2018.

[175] D. A. Abanin, W. De Roeck, and F. Huveneers, "Exponentially Slow Heating in Periodically Driven Many-Body Systems," *Phys. Rev. Lett.*, vol. 115, p. 256803, dec 2015.

[176] P. Ponte, A. Chandran, Z. Papić, and D. A. Abanin, "Periodically driven ergodic and many-body localized quantum systems," *Ann. Phys. (N. Y).*, vol. 353, pp. 196–204, feb 2015.

[177] A. Matthies, J. Park, E. Berg, and A. Rosch, "Stability of Floquet Majorana Box Qubits," *Phys. Rev. Lett.*, vol. 128, p. 127702, mar 2022.

[178] Z. Yang, Q. Yang, J. Hu, and D. E. Liu, "Dissipative Floquet Majorana Modes in Proximity-Induced Topological Superconductors," *Phys. Rev. Lett.*, vol. 126, p. 086801, feb 2021.

[179] M. Fruchart, P. Delplace, J. Weston, X. Waintal, and D. Carpentier, "Probing (topological) Floquet states through DC transport," *Phys. E Low-dimensional Syst. Nanostructures*, vol. 75, pp. 287–294, jan 2016.

[180] L. Arrachea and M. Moskalets, "Relation between scattering-matrix and Keldysh formalisms for quantum transport driven by time-periodic fields," *Phys. Rev. B*, vol. 74, p. 245322, dec 2006.

[181] Y. V. Fyodorov and H. J. Sommers, "Spectra of random contractions and scattering theory for discrete-time systems," *J. Exp. Theor. Phys. Lett.*, vol. 72, pp. 422–426, oct 2000.

[182] M. Büttiker, A. Prêtre, and H. Thomas, "Dynamic conductance and the scattering matrix of small conductors," *Phys. Rev. Lett.*, vol. 70, pp. 4114–4117, jun 1993.

[183] J. E. Avron, A. Elgart, G. M. Graf, and L. Sadun, "Optimal Quantum Pumps," *Phys. Rev. Lett.*, vol. 87, p. 236601, nov 2001.

[184] A. S. Landsberg, "Geometrical phases and symmetries in dissipative systems," *Phys. Rev. Lett.*, vol. 69, pp. 865–868, aug 1992.

[185] T. Pluecker, M. R. Wegewijs, and J. Splettstoesser, "Gauge freedom in observables and Landsberg's nonadiabatic geometric phase: Pumping

spectroscopy of interacting open quantum systems," *Phys. Rev. B*, vol. 95, p. 155431, apr 2017.

[186] N. A. Sinitsyn and I. Nemenman, "Universal Geometric Theory of Mesoscopic Stochastic Pumps and Reversible Ratchets," *Phys. Rev. Lett.*, vol. 99, p. 220408, nov 2007.

[187] N. A. Sinitsyn and I. Nemenman, "The Berry phase and the pump flux in stochastic chemical kinetics," *Europhys. Lett.*, vol. 77, p. 58001, mar 2007.

[188] Z. Wang, L. Wang, J. Chen, C. Wang, and J. Ren, "Geometric heat pump: Controlling thermal transport with time-dependent modulations," *Front. Phys.*, vol. 17, p. 13201, feb 2022.

[189] J. Tobiska and Y. V. Nazarov, "Josephson Junctions as Threshold Detectors for Full Counting Statistics," *Phys. Rev. Lett.*, vol. 93, p. 106801, sep 2004.

[190] S. Gustavsson, R. Leturcq, B. Simovič, R. Schleser, T. Ihn, P. Studerus, K. Ensslin, D. C. Driscoll, and A. C. Gossard, "Counting Statistics of Single Electron Transport in a Quantum Dot," *Phys. Rev. Lett.*, vol. 96, p. 076605, feb 2006.

[191] B. Dutta, J. T. Peltonen, D. S. Antonenko, M. Meschke, M. A. Skvortsov, B. Kubala, J. König, C. B. Winkelmann, H. Courtois, and J. P. Pekola, "Thermal conductance of a single-electron transistor," *Phys. Rev. Lett.*, vol. 119, p. 077701, Aug 2017.

[192] L. B. Wang, O.-P. Saira, and J. P. Pekola, "Fast thermometry with a proximity Josephson junction," *Appl. Phys. Lett.*, vol. 112, p. 013105, jan 2018.

[193] F. Brange, P. Samuelsson, B. Karimi, and J. P. Pekola, "Nanoscale quantum calorimetry with electronic temperature fluctuations," *Phys. Rev. B*, vol. 98, p. 205414, nov 2018.

[194] D. R. White, R. Galleano, A. Actis, H. Brixy, M. D. Groot, J. Dubbeldam, A. L. Reesink, F. Edler, H. Sakurai, R. L. Shepard, and J. C. Gallop, "The status of Johnson noise thermometry," *Metrologia*, vol. 33, pp. 325–335, aug 1996.

[195] P. Molignini, E. van Nieuwenburg, and R. Chitra, "Sensing Floquet-Majorana fermions via heat transfer," *Phys. Rev. B*, vol. 96, p. 125144, sep 2017.

[196] L. S. Ricco, F. A. Dessotti, I. A. Shelykh, M. S. Figueira, and A. C. Seridonio, "Tuning of heat and charge transport by Majorana fermions," *Sci. Rep.*, vol. 8, p. 2790, dec 2018.

[197] S. Smirnov, "Universal Majorana thermoelectric noise," *Phys. Rev. B*, vol. 97, p. 165434, apr 2018.

[198] B. A. Muzykantskii and D. E. Khmelnitskii, "Quantum shot noise in a normal-metal-superconductor point contact," *Phys. Rev. B*, vol. 50, no. 6, pp. 3982–3987, 1994.

[199] M. Moskalets and M. Büttiker, "Dissipation and noise in adiabatic quantum pumps," *Phys. Rev. B*, vol. 66, p. 035306, jul 2002.

[200] A. Romito, J. Alicea, G. Refael, and F. von Oppen, "Manipulating Majorana fermions using supercurrents," *Phys. Rev. B*, vol. 85, p. 020502, jan 2012.

[201] C. Beenakker, "Search for non-Abelian Majorana braiding statistics in superconductors," *SciPost Phys. Lect. Notes*, p. 15, aug 2020.

[202] T. Karzig, Y. Oreg, G. Refael, and M. H. Freedman, "Universal Geometric Path to a Robust Majorana Magic Gate," *Phys. Rev. X*, vol. 6, p. 031019, aug 2016.

[203] P. Bonderson, M. Freedman, and C. Nayak, "Measurement-Only Topological Quantum Computation," *Phys. Rev. Lett.*, vol. 101, p. 010501, jun 2008.

[204] J. A. Schreier, A. A. Houck, J. Koch, D. I. Schuster, B. R. Johnson, J. M. Chow, J. M. Gambetta, J. Majer, L. Frunzio, M. H. Devoret, S. M. Girvin, and R. J. Schoelkopf, "Suppressing charge noise decoherence in superconducting charge qubits," *Phys. Rev. B*, vol. 77, p. 180502, may 2008.

[205] C. Mahaux and H. A. Weidenmüller, *Shell-model approach to nuclear reactions.* 1969.

[206] M. F. Ludovico, F. Battista, F. von Oppen, and L. Arrachea, "Adiabatic response and quantum thermoelectrics for ac-driven quantum systems," *Phys. Rev. B*, vol. 93, p. 075136, feb 2016.

[207] A. Bruch, C. Lewenkopf, and F. von Oppen, "Landauer-Büttiker Approach to Strongly Coupled Quantum Thermodynamics: Inside-Outside Duality of Entropy Evolution," *Phys. Rev. Lett.*, vol. 120, p. 107701, mar 2018.

[208] N. Bode, S. V. Kusminskiy, R. Egger, and F. von Oppen, "Scattering Theory of Current-Induced Forces in Mesoscopic Systems," *Phys. Rev. Lett.*, vol. 107, p. 036804, jul 2011.

[209] J. M. Horowitz and T. R. Gingrich, "Thermodynamic uncertainty relations constrain non-equilibrium fluctuations," *Nat. Phys.*, vol. 16, pp. 15–20, jan 2020.

[210] T. Koyuk and U. Seifert, "Operationally Accessible Bounds on Fluctuations and Entropy Production in Periodically Driven Systems," *Phys. Rev. Lett.*, vol. 122, p. 230601, jun 2019.

[211] J. Lu, Z. Wang, J. Peng, C. Wang, J.-H. Jiang, and J. Ren, "Geometric thermodynamic uncertainty relation in a periodically driven thermoelectric heat engine," *Phys. Rev. B*, vol. 105, p. 115428, mar 2022.

[212] J. Eglinton and K. Brandner, "Geometric bounds on the power of adiabatic thermal machines," *Phys. Rev. E*, vol. 105, p. L052102, may 2022.